6-23-2015

Rayleigh—Taylor-Instability Evolution in Colliding-Plasma-Jet Experiments with Magnetic and Viscous Stabilization

Colin Stuart Adams

Colin S. Adams
Candidate

Electrical and Computer Engineering
Department

This dissertation is approved, and it is acceptable in quality and form for publication:

Approved by the Dissertation Committee:

Mark Gilmore , Chairperson

Scott Hsu

Edl Schamiloglu

Ylva Pihlstrom

Rayleigh–Taylor-Instability Evolution in Colliding-Plasma-Jet Experiments with Magnetic and Viscous Stabilization

by

Colin S. Adams

B.S., Aeronautical and Astronautical Engineering,
University of Washington, 2005

M.S., Aeronautics and Astronautics, University of Washington, 2009

DISSERTATION

Submitted in Partial Fulfillment of the

Requirements for the Degree of

Doctorate of Philosophy
Engineering

The University of New Mexico

Albuquerque, New Mexico

May, 2015

Dedication

To my family, for all the encouragement over the years.

Acknowledgments

I would like to express sincere appreciation to advisor and committee chair Mark Gilmore and project principal investigator Scott Hsu for their guidance and support throughout. Thanks as well to Edl Schamiloglu and Ylva Pihlström for their contributions as dissertation committee members. The experiments reported on in this dissertation were supported as well by the efforts of Auna Moser and John Dunn whose advice and companionship were invaluable. Thanks are due to Glen Wurden, who generously provided a multi-frame fast camera for use in these experiments. The efforts of many at the Plasma Liner Experiment over the years laid the groundwork for this research, with special mention of Elizabeth Merritt for help with the interferometer diagnostic. Special thanks to my wife, Bhuvana Srinivasan, for help with running simulations, editing this dissertation, and the substantial support and encouragement along the way. Thanks as well to my friends (especially those at LANL and UNM) who provided great companionship and to my parents and brother for, in addition to everything else, their generous patience. I must also acknowledge the canine companionship and therapeutic walks with Tina.

The author wishes to acknowledge the University of Washington for developing the code WARPX which was used in this work. Finally, this research was funded by the Laboratory Directed Research and Development program at the Los Alamos National Laboratory under Department of Energy contract number DE-AC52-06NA25396.

Rayleigh–Taylor-Instability Evolution in Colliding-Plasma-Jet Experiments with Magnetic and Viscous Stabilization

by

Colin S. Adams

B.S., Aeronautical and Astronautical Engineering,

University of Washington, 2005

M.S., Aeronautics and Astronautics, University of Washington, 2009

Ph.D., Engineering, University of New Mexico, 2015

Abstract

The Rayleigh–Taylor instability causes mixing in plasmas throughout the universe, from micron-scale plasmas in inertial confinement fusion implosions to parsec-scale supernova remnants. The evolution of this interchange instability in a plasma is influenced by the presence of viscosity and magnetic fields, both of which have the potential to stabilize short-wavelength modes. Very few experimental observations of Rayleigh–Taylor growth in plasmas with stabilizing mechanisms are reported in the literature, and those that are reported are in sub-millimeter scale plasmas that are difficult to diagnose. Experimental observations in well-characterized plasmas are important for validation of computational models used to make design predictions for inertial confinement fusion efforts. This dissertation presents observations of instability growth during the interaction between a high Mach-number, initially unmagnetized plasma jet and a stagnated, magnetized plasma. A multi-frame fast camera captures Rayleigh–Taylor-instability growth while interferometry, spectroscopy,

photodiode, and magnetic probe diagnostics are employed to estimate plasma parameters in the vicinity of the collision. As the instability grows, an evolution to longer mode wavelength is observed. Comparisons of experimental data with idealized magnetohydrodynamic simulations including a physical viscosity model suggest that the observed instability evolution is consistent with both magnetic and viscous stabilization. These data provide the opportunity to benchmark computational models used in astrophysics and fusion research.

Contents

List of Figures

List of Figures

List of Figures

List of Tables

Chapter 1

Introduction

1.1 The Rayleigh–Taylor Instability

The Rayleigh–Taylor instability is an interchange instability to which fluids are subject when the density gradient vector opposes the fluid-reference-frame acceleration vector. When a denser fluid is placed above a less dense fluid, 'spikes' of the denser fluid will fall as 'bubbles' of the less dense fluid rise. The nature of this instability was first characterized by Lord Rayleigh in 1883 who derived the linear growth rate (γ),

$$\gamma^2 = gk\frac{\rho_2 - \rho_1}{\rho_2 + \rho_1} \tag{1.1}$$

(where k is the wavenumber of the mode), for displacement of a boundary between two fluids of different densities $\rho_1 < \rho_2$ in a gravitational field g [1]. In 1950 Taylor generalized understanding of the instability to apply to arbitrary accelerating fluid interfaces [2]. Recent research interest in the Rayleigh-Taylor instability stems from its prevalence both in astrophysical phenomena and its role in fluid mixing in imploding fusion systems.

In situations of interest in modern research, the unstable interfaces are often interfaces between plasmas, which can be stabilized against the growth of certain Rayleigh–Taylor-instability modes by the presence of magnetic fields or plasma viscosity. Theoretical work by Chandrasekhar in 1961 characterized the effect of viscosity and a magnetic field oriented parallel to the mode wavevector on linear growth rate. Both were shown to be capable of preventing the growth of short-wavelength modes [3]. Chandrasekhar linearizes the magnetohydrodynamic equations with a transverse (x-direction) uniform magnetic field B, transverse to the direction of $\vec{g}$ (y-direction), with zero viscosity and zero resistivity. Once the continuity, momentum, and magnetic induction equations are linearized and combined, the dispersion relation

$$D\left(\rho D v_y\right) + \frac{B^2 k_x^2}{4\pi\gamma^2}\left(D^2 - k^2\right) v_y - k^2 \rho v_y = -\frac{g k^2}{\gamma^2}\left(D\rho\right) v_y \tag{1.2}$$

is produced, where $D = d/dy$ and v_y is y-direction velocity. The two uniform fluids are separated by a horizontal boundary at $y = 0$ and this derivation requires that v_y and B are continuous at $y = 0$. Integrating Equation 1.2 across the interface and simplifying gives the linear magnetic-Rayleigh–Taylor growth rate

$$\gamma^2 = gkA - \frac{\left(\vec{k}\cdot\vec{B}\right)^2}{2\pi\left(\rho_2 + \rho_1\right)}, \tag{1.3}$$

in cgs units, A is the Atwood number given by $(\rho_2 - \rho_1)/(\rho_2 + \rho_1)$, and $\vec{B}$ the magnetic field vector. Comparing Equations 1.1 and 1.3, it is clear that the case of a conducting fluid in the presence of a magnetic field introduces a stabilizing term which reduces the linear growth rate for all wavelengths, and drastically so for short wavelengths. While not unique to plasmas or conducting fluids, the presence of viscosity stabilizes wavelengths shorter than a wavelength of maximum growth rate given by

$$\lambda_{\max} = 4\pi\left(\frac{\nu^2}{gA}\right)^{1/3}, \tag{1.4}$$

where ν is the kinematic viscosity. Equation 1.4 is derived by Plesset and Whipple by treating the fluid interface as a damped harmonic oscillation, and solving for the fastest growing mode in the limit of short wavelength. Viscosity is particularly important when studying Rayleigh–Taylor instabilities in fusion-relevant plasmas because plasma viscosity is a strongly positive function of temperature. Further work by Huba et al. extended the theoretical basis of Rayleigh–Taylor instabilities in magnetized plasmas (field direction not linearly stabilizing) to show that for large ion gyroradius, the instability grows much faster than growth in plasmas with smaller ion gyroradius. Another significant result in the Huba work indicated that late-time (nonlinear) behavior of Rayleigh–Taylor in plasmas with large ion gyroradii is dominated by longer wavelength modes and the result is greater density profile disruption than for the small gyroradius case [4].

1.1.1 Importance of Rayleigh–Taylor Instability in Physical Processes

Observations of the presence of filaments in the Crab nebula by the Hubble Space Telescope [5] (Figure 1.1) have been attributed to the growth of the Rayleigh–Tayor instability in supernova remnants [6]. Other Hubble observations including the famous images of the "Pillars of Creation" in the Eagle nebula [7] have been postulated to have originated as Rayleigh–Taylor-instability modes [8]. On much smaller spatial scales, Rayleigh–Taylor instabilities are known to cause fluid mixing during the deceleration phase of inertial confinement fusion implosions [9]. In this scenario cool, dense material from the capsule shell interior slows on the hot, low density material of the so-called 'hot-spot'. This interface is susceptible to Rayleigh–Taylor mixing of cold material into the hot-spot which is thought to prevent temperatures from rising high enough to sustain a fusion burn wave [9]. Similar challenges are relevant to cylindrical liners proposed for use in some magneto-inertial fusion concepts

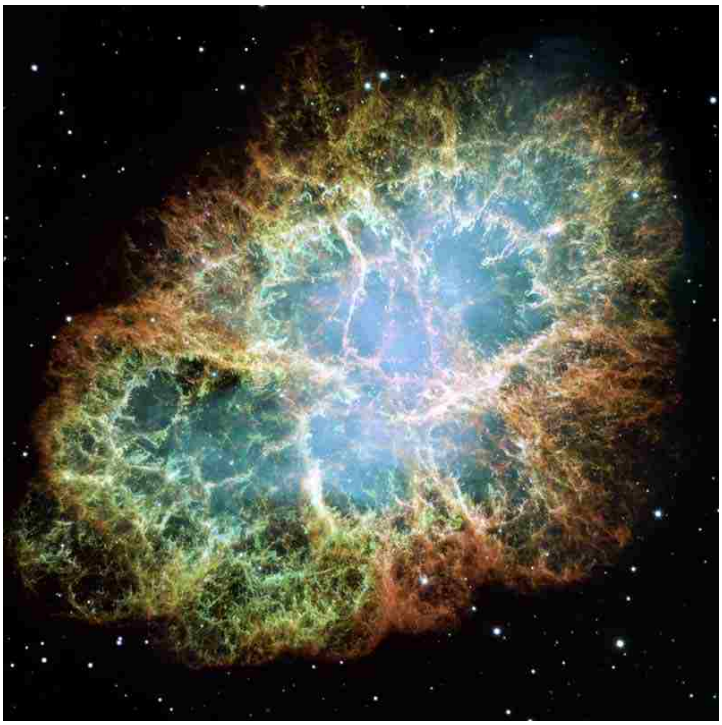

Figure 1.1: Hubble Space Telescope image of filaments in the Crab nebula, attributed to spikes and bubbles. In the center of the image, the blue glow is synchrotron radiation from relativistic electrons in the vicinity of a neutron star. At the edges, blue indicates [O I] spectra, green indicates [S II] spectra, and red indicates [O III] spectra. Image from NASA, ESA, Hester and Loll (ASU)[5].

where the inner surface of a solid-density liner slows on a much less dense magnetized plasma [10]. Likewise, in the earlier acceleration phase, the outer surface of both cylindrical and spherical inertial fusion capsules are subject to Rayleigh–Taylor growth as low-density, ablating material accelerates inward toward higher-density material. Growth at this interface could break up the pusher material and prevent compression of the fuel in the capsule.

1.1.2 Recent Investigation of Rayleigh–Taylor Instability

There are few recent experimental investigations of the Rayleigh–Taylor instability in plasmas with stabilizing mechanisms. A significant example includes experiments in a regime with viscous stabilization conducted by Robey et al. at the OMEGA laser facility, which gathered data from a linearly-translating plasma density interface. Analysis of these data, some of which are shown in Figure 1.2, confirmed that short wavelength Rayleigh–Taylor modes are affected by plasma viscosity, which is often unaccounted for in radiation-hydrodynamic codes [11]. The perturbation wavelengths ranged from 22.5 μm to 180 μm and reduced mode growth was found for shorter wavelength perturbations. The authors point out that inviscid computational models will over-predict short wavelength mode activity, causing inaccurate predictions of instability evolution. Recent computational study by Haines et al. investigated the related phenomena of multi-species mass diffusion during Rayleigh–Taylor growth. These simulations predicted that viscosity damps instability growth in certain regimes relevant to inertial confinement fusion implosions [12].

In a regime where magnetic stabilization is relevant, a series of investigations at the Z Pulsed Power Facility were conducted starting with work reported by Sinars et al. in which the magneto-Rayleigh–Taylor instability was imaged on the surface of an imploding cylindrical liner, without an applied axial magnetic field. These results, shown in Figure 1.3, demonstrated mode growth which agreed well with the predictions of hydrodynamic simulations and demonstrated azimuthal correlation of mode growth [13, 14]. Very few examples of well-resolved observations of magnetic Rayleigh–Taylor-instability growth are found in published literature, of which these results are an exceptional case. Even so, the length scales (~ 100 μm) of the Sinars results make it challenging to diagnose local plasma parameters. Further work at the same experimental facility investigated the addition of a strong axial magnetic field to the previously-reported implosions. The newly-applied field was oriented

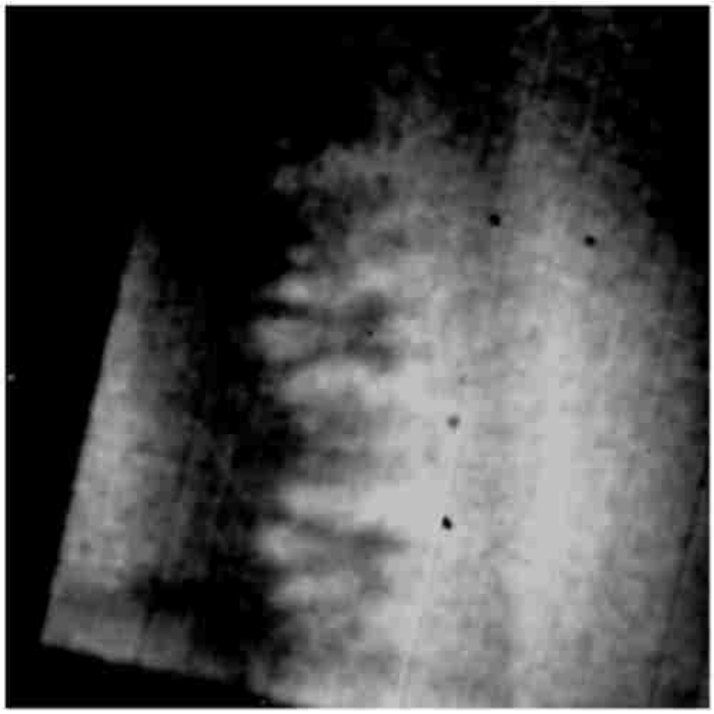

Figure 1.2: Multimode Rayleigh–Taylor growth in regime where viscosity stabilizes short-wavelength modes. Initial perturbation contains 8 wavelengths varying by a factor of 8, with random amplitude. Height of region imaged is ≈ 500 μm. Image from Ref. [11].

in a direction parallel to the previously observed mode growth, which according to linear theory should provide a stabilizing influence. The results, reported by Awe et al. showed suppressed traditional mode growth, while simultaneously showing the growth of helical-type structures during the implosion [15].

Simulation results published in 2014 by Weis et al. examined the damping of Rayleigh–Taylor modes as they propagated through a slab of magnetized plasma [16]. In these simulations, magnetic fields of significant magnitude were included such that a component of the pressure forces driving the instability were provided by the magnetic pressure. The attenuation of instability modes by the slab was

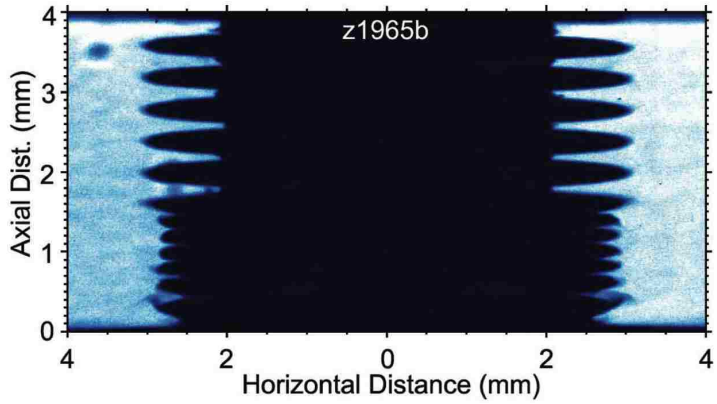

Figure 1.3: Magneto-Rayleigh–Taylor growth in imploding cylindrical liner perturbed with $\lambda = 400$ μm perturbations (top), $\lambda = 200$ μm perturbations (bottom-middle), and no perturbation (bottom-most 0.4 mm). Image from Ref. [14].

predicted to depend on the mode wavelength relative to the slab thickness. This configuration was chosen for its relevance to the experimental results published by Awe et al.

Finally, in 2012, an experimental campaign by Manuel et al. investigated magnetic fields self-generated by the growth of Rayleigh–Taylor-instability modes on ~ 100 μm spatial scales. For the first time, the existence of such fields were confirmed and measurements of their magnitude were made and compared to computational models. While correlating, the computational predictions were outside of the the error bars of the experimental data [17]. A theoretical and computational study by Srinivasan et al. published the same year found that such self-generated fields, while too small to impact mode growth, could exist of sufficient magnitude to inhibit cross-field thermal conduction in inertial confinement fusion implosions [18].

Other modern research on Rayleigh–Taylor stabilization mechanisms and instability behavior in the presence of variously oriented magnetic fields relies heavily on numerical studies and focuses heavily on the context of inertial confinement fusion.

A detailed computational study conducted by Jun et al. showed that for multimode Rayleigh–Taylor, magnetic fields oriented normal to the interface can enhance mixing due to flow collimation along field lines [19]. This work also explored the role of magnetic fields self-generated by turbulence, and found that such fields are preferentially amplified on short length scales through stretch-and-fold mechanisms. More computational studies by Stone and Gardiner showed that even small applied magnetic fields reduce mixing at small length scales and can enhance long-wavelength mode growth by preventing secondary instabilities from slowing the progress of bubbles and spikes [20, 21]. Additionally these computations predicted that very strong magnetic fields can cause the formation of large scale "rope"- and "filament"-like structures as the instability evolves. More recent research by Srinivasan and Tang computationally predicted that the critical wavelength, below which all modes are stabilized, changes locally during instability evolution as magnetic fields are amplified and reoriented [22].

Other examples of data from experiments useful for code verification and validation are few. An experimental campaign at the OMEGA laser facility, where inertial confinement fusion capsules were imploded in the presence and absence of applied uniform magnetic fields showed an increase in temperature (15%) and neutron yield (30%) [23, 24]. During the implosion, flux compression amplified the initially-applied magnetic field by a factor of ≈ 500, and the authors attributed the increased yield to reduction in thermal conductivity across field lines. The possibility of Rayleigh–Taylor-instability stabilization and associated reduction of hydrodynamic mix was not discussed in this research.

Described in this dissertation are observations of instability growth consistent with the Rayleigh–Taylor instability when a supersonic jet encounters a stagnated, magnetized plasma. Experimental results presented in this dissertation include macroscopic (multiple-cm scale) observations of Rayleigh–Taylor-instability growth

in a readily diagnosable plasma regime. Sufficient data were collected to establish that instability growth occurs in a plasma sufficiently magnetized and with sufficient viscosity that both stabilization mechanisms are relevant to the observed dynamics. This result is relevant to validation of computational models, and to the knowledge of the author is unique — especially with regard to the level of plasma parameter characterization.

1.2 Physics of Colliding Plasmas

An experimental campaign using the Plasma Liner Experiment [25] at Los Alamos National Laboratory led to the observations of Rayleigh–Taylor instability growth described in this dissertation. This series of experiments was initially motivated by the study of magnetized interactions relevant to astrophysics [26]. In the course of the investigation, the interaction of plasma jets with a background magnetic field and with a magnetized background plasma became important to understanding the physical processes present during plasma jet interaction. These topics are overviewed in this section to provide context for the experiments described.

1.2.1 Plasma Collision with a Vacuum Magnetic Field

Previous observations of relevant phenomena include work by Baker and Hammel examining the interaction of plasma jets with background magnetic fields. These experiments detected evidence of charge separation as streaming particles deflect in the presence of a magnetic field [27, 28]. This research showed that $\vec{v} \times \vec{B}$ drift caused the development of an electric potential in a direction transverse to the direction of jet propagation. This in turn generated an $\vec{E} \times \vec{B}$ drift equal and opposite in magnitude, which prevented stopping of the jet by the magnetic field in the ab-

sence of wall interactions. The Baker experiments were conducted in two parameter regimes, one with jet densities $n_{\text{jet}} \sim 10^{15}$ cm^{-3} and velocities $v_{\text{jet}} \approx 5 \times 10^6$ cm/s, while the other had lower densities of $n_{\text{jet}} \approx 3 \times 10^{13}$ cm^{-3} and higher velocities $v_{\text{jet}} \approx 4 \times 10^7$ cm/s. In both cases, penetration of the magnetic field by the jets occurred due to self-polarization of the plasma jet causing an $\vec{E} \times \vec{B}$ drift. This mechanism of jet propagation by generation of an $\vec{E} \times \vec{B}$ drift was corroborated in results reported by Beckner [29]. Later research by Marković and Scott observed a transition in plasma jet behavior in encountering magnetic fields of increasing strength. A critical magnetic field magnitude of $B_{\text{critical}} = \sqrt{12\pi\rho v_{\text{jet}}^2}$ (cgs units) was found, below which the incoming jet would exclude the ambient magnetic field from its volume as it propagated, while above the critical magnitude, the magnetic field extrudes the plasma jet into filaments as it enters the magnetic field [30]. The authors speculate that this filamentation creates conditions susceptible to Rayleigh–Taylor-instability growth.

A series of experiments conducted by Jellison and Parsons imaged a barium plasma expanding into a magnetic field. During expansion the plasma was observed to compress the magnetic field, causing the plasma to have well-defined edges as opposed to the diffuse images seen when no field was present [31]. Furthermore, striations were observed in the portions of the barium plasma that expanded more slowly. A development of this work involved the collisionless flow of a barium plasma through a background xenon plasma magnetized with a field transverse to the barium propagation. In these experiments, the streaming barium was observed to slow in a manner consistent with streaming instabilities enhanced by the presence of the magnetic field [32].

1.2.2 Collisionless, Unmagnetized Jet Interactions

The Weibel instability arises when counterstreaming plasma flows interact at very high relative velocities ($\gtrsim$ 1000 km/s) [33]. This interaction is thought to generate magnetic fields and be responsible for high-energy particle phenomena in astrophysical systems. Recent laboratory studies of this type of instability were conducted with laser-produced plasmas and observations were consistent with the presence of Weibel-generated fields [34].

At much lower relative velocities, recent experiments at the Plasma Liner Experiment involve merging jets in semi-collisionless to collisionless regimes and in the absence of a magnetic field. Initial results where the jets merged at an oblique angle demonstrated a collisional interaction [35]. During further experiments where the jets merged head-on, an ionization-mediated transition from collisionless interpenetration to the formation of a collisional shock was observed [36, 37]. While initially collisionless, the strong dependence of mean-free-path on mean ionization state ($\sim Z^{-4}$) caused the nature of the interaction to change on experimental timescales.

Other recent research by Swadling et al. investigated the dynamics of imploding jets formed by ablation of a cylindrical wire array. For most of the distance of jet propagation, magnetic field was negligible. In these experiments, collisionless interpenetration was observed between tungsten jets, while collisional oblique shocks were observed in interactions between aluminum jets [38].

1.2.3 Collisionless, Magnetized Jet Interactions

An experimental campaign with the goal of studying astrophysically-relevant collisionless shocks was undertaken at the Plasma Liner Experiment. These collisionless shocks, commonly referred to as 'cosmic' shocks are of interest because they are

thought to play an important role in astrophysical processes including the acceleration of charged particles to very high energies. The flow transition in cosmic shocks is mediated through charged particle interactions with an ambient magnetic field which lead to magnetohydrodyamic turbulence at the shock front [39]. While these shocks have been studied with computational tools [40] and evidence of their existence have been observed in the universe [41], they have never been replicated in a laboratory setting. In order to meaningfully study such shocks, an experiment must operate in an unique parameter space, characterized by highly magnetized, high β, collisionless flows interacting at super-Alfvénic speeds, among other requirements [39].

In recent years a number of other experiments have probed magnetized, collisionless interactions such as research by Courtois et al. where counter-propagating laser-generated plasmas interpenetrate both in the presence and absence of a magnetic field. Although features in density were observed to uniquely occur in the presence of the magnetic field, shocks were not detected [42].

1.3 Organization of this Dissertation

The remainder of this dissertation is organized as follows. Chapter 2 describes the experimental apparatus and the diagnostics employed to capture and characterize the reported observations of Rayleigh–Taylor-instability growth, and discussion of data analysis methods. Chapter 3 discusses the details of a schlieren diagnostic that was designed and constructed for use in plasmas with higher densities than those reported on in this dissertation. This chapter is included as a guide for diagnostic use with future experiments in those regimes. Chapter 4 reports the observations of instability growth and analyzes the results in the context of theory and computational modeling. Finally, Chapter 5 contains suggestions for future work and concludes the dissertation. Appendices are also included with supplementary material.

Chapter 2

Experimental Apparatus

2.1 Experimental Facility Overview

The experiments described in this dissertation were conducted at the Plasma Liner Experiment [43, 25] located at the Los Alamos National Laboratory. The experimental apparatus is constructed around a 9 ft diameter vacuum vessel about which plasma-armature railguns can be placed at any of 60 small 11-in. ports. The railguns fire jets of plasma supplied by compressed gas bottles into the chamber where an array of diagnostics with access through large 30-in. ports gather data on jet propagation and interactions. An annotated photograph of this apparatus is seen in Figure 2.1. Previous experiments conducted with this apparatus include characterization of a single jet [43], oblique merging of two jets [35], and head-on merging of two jets in a semi-collisional regime in the absence of a magnetic field [36, 37].

For the experiments presented here, two plasma-armature railguns fired plasma jets composed of argon and impurity materials which are ablated from the zirconia-toughened-alumina insulator placed between the conducting rails. The railguns were positioned such that jets were fired in a head-on configuration. A schematic and

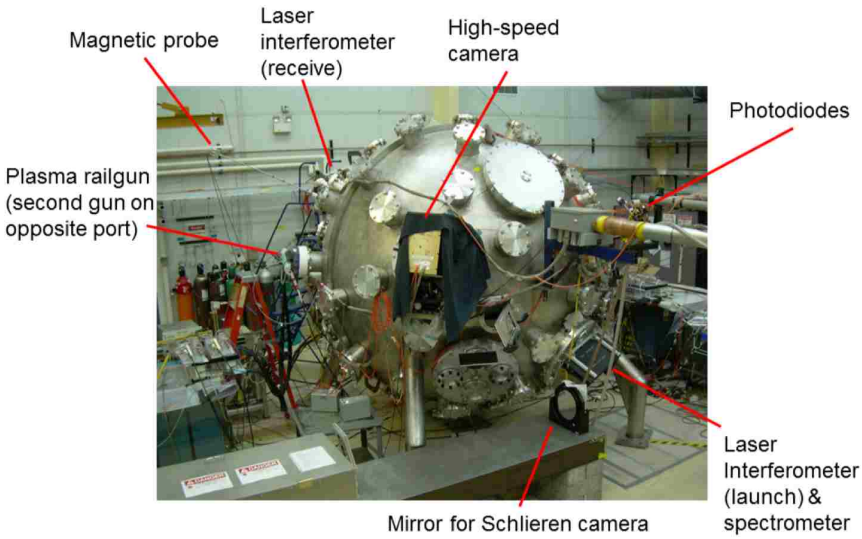

Figure 2.1: The 9 ft diameter vacuum vessel is equipped with 11 and 30 in diameter ports. Most diagnostic access is provided by the large ports, and railguns are placed at the desired 11 in ports. The high-speed camera called out here is a Dicam Pro ICCD. For the experiments presented here, a multi-frame Invisible Vision UHSi 12/24 high-speed camera was placed at an 11-in port on the opposite side of the vacuum chamber. Image from [44].

photograph of the railguns are seen in Figure 2.2. The two railguns were positioned such that the jets merge head on after propagating approximately 1.1 meters to the center of the 9 ft. diameter spherical vacuum chamber.

A recent addition to the experimental apparatus are the in-vacuum Helmholtz-configuration magnetic field coils. These coils, designed and wound by Woodruff Scientific Inc., were installed in the center of the chamber such that the magnetic field generated would be oriented transverse to the propagation direction of the plasma jets, as seen in Figure 2.3 [25]. The 30-cm radius coils are electrically connected in series and have a combined inductance of 246 μH. The capacitor bank which energizes the coils has a capacitance of 4 mF, and the resulting RLC circuit has a rise time of $\approx$ 1.3 ms which is very slow compared to the dynamics of the jet interactions (which

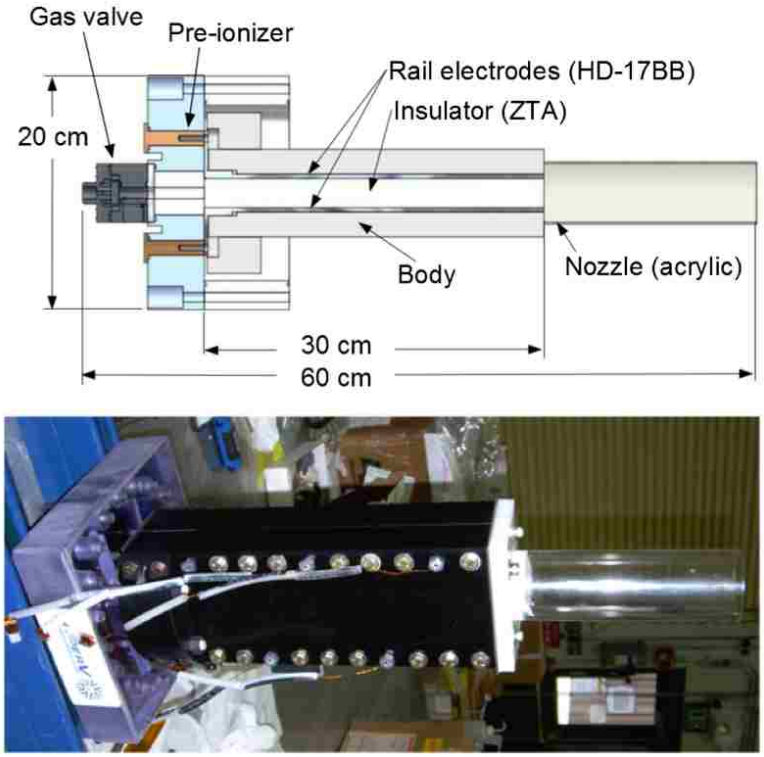

Figure 2.2: The plasma-armature railguns, produced by HyperV Technologies Corp., are built from two tungsten alloy (HD-17BB) rails insulated by zirconia-toughened-alumina standoffs. Gas is puffed between the two rails before a pre-ionizer breaks down the gas and a high-voltage, high-current discharge accelerates the plasma down the rails. Image from [43, 44].

occur on ~ 10 μs timescales), and the Helmholtz field is considered to be steady state. After installation of the coils, three concentric flux loops were placed on the symmetry axis of the coils and the field and coil current was measured for applied voltages up to 4 kV. This enabled the characterization of magnetic field as a function of coil current. For a broad range of Helmholtz coil currents, the installation generates approximately 270 G/kA at the center of the coils. Prior to the completion of Helmholtz coil characterization and subsequent use in experimental campaigns, it was necessary to design, fabricate, and install buswork based on $1'' \times 1/8''$ copper stock to supply

current to the coils. The original plan to power the coils using 11 AWG copper wire ran into trouble when the magnetic fields were found to have sufficient magnitude to bend the wires and cause them to short on the conducting support structure. After installing the buswork, coil operation was much more reliable except for occasional arcing between the buswork and the support structure at high operating voltages (in excess of ≈ 1 kV). An attempt was made to insulate the buswork with fiberglass braid, but this seemed to have little effect, and operating voltages on the Helmholtz bank were kept below 1 kV.

Figure 2.3: View of the in-vacuum Helmholtz coils, with end-on view of far railgun bore visible. Copper buswork, prior to insulation attempts, is visible in the bottom of the image. Image from [25].

In the experimental sequence, time $t = 0$ references the time at which the railguns are fired. The Helmholtz coil is energized at $t \approx -1.3$ ms, the valves which supply gas to the railguns are opened at $t \approx -300$ μs, and a pre-ionizing circuit in the railgun breech is energized at $t \approx -30$ μs. After the railguns are fired, the time of flight of the jets from the nozzle affixed to the gun muzzle to their respective edges of the Helmholtz coil is ≈ 20 μs, while it is not until $t \approx 30$ μs that the jets begin to interact with each other. Due to underdamped ringing of the circuit which provides current to the railguns, plasma jets are released from each gun in a series. This ringing is seen in the two current traces in Figure 2.4. After the first two jets collide, a second jet arrives in the interaction region as depicted in Figure 2.5, and approximately 30 μs later collides with the magnetized, stagnated plasma remaining in the interaction region from the previous collision. It is during this secondary collision that Rayleigh–Taylor instabilities are observed.

2.2 Diagnostic Overview

A suite of diagnostics, including a survey spectrometer, 8-chord visible wavelength (561.3 nm) interferometer [45, 46], magnetic flux probes, and two fast cameras are employed to study the interaction region. A cartoon of the arrangement of the diagnostics within the vacuum chamber is shown in Figure 2.6. One of the fast cameras, an Invisible Vision UHSi 12/24 captures 12 frames separated by 2 μs per experimental pulse in the experiments reported here (installation location not visible in Figure 2.1). Each frame captures visible light with a 750 ns exposure time and, after cropping the distorted edges of each frame, a maximum useful resolution of 1000×860. A visible wavelength spectrometer captures spectra from region ≈ 7 cm in diameter, centered at the location of an interferometer chord, for a short gate time during the experimental pulse. During an experimental pulse, a gate valve

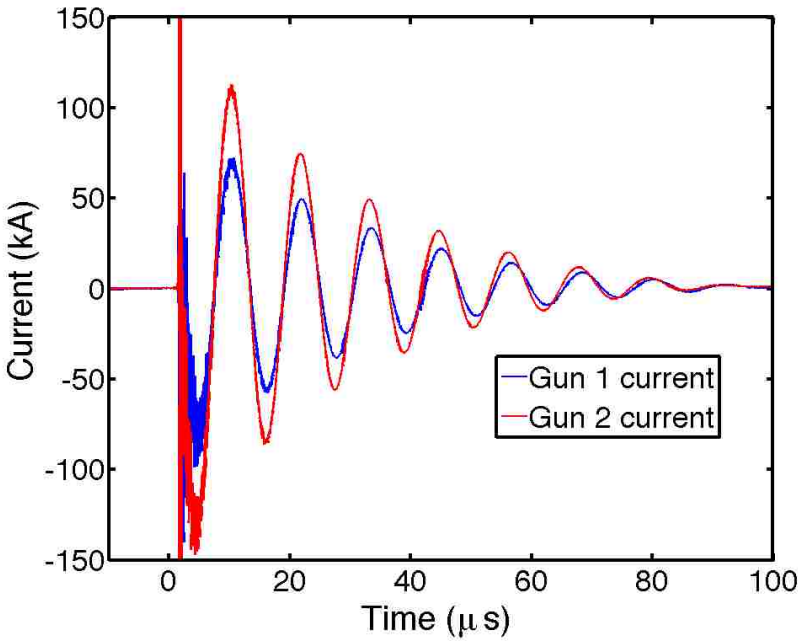

Figure 2.4: Current in the circuit powering the rails of each railgun is shown. Ringing is seen with a period of approximately 11 μs.

isolates the vacuum chamber from the compound molecular pump. By measuring the chamber pressure rise during shots during which only the gas puff valves are fired, an the amount of injected gas in the jets is estimated. By comparing this case with the pressure rise during "full" shots with the railguns energized, an estimate of the amount of impurities which are ablated from the railgun insulation is made.

Plasma ion density n_i, electron temperature T_e, and mean-ionization state $\bar{Z}$ are determined by an iterative process [43]. An initial value of $n_i \cdot dl$ (where dl is chord length through the plasma) is estimated from interferometer phase shift data using an assumed value of $\bar{Z}$. An approximate chord length dl is estimated from fast camera images to estimate the ion number density. This density estimate is used in concert with an estimate of the species mixture in non-local-thermodynamic-

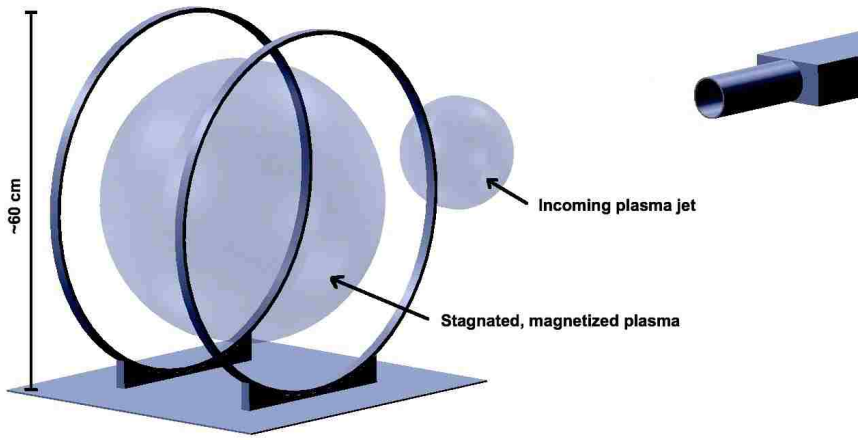

Figure 2.5: Notional view of experimental setup. Two plasma jets launched by oppositely positioned railguns collide in the presence of a magnetic field generated by the Helmholtz configuration magnetic coils before a second jet arrives at the remnants of the initial interaction. Note that only one of the two opposing plasma guns is shown.

equilibrium spectral calculations performed by PrismSPECT software [47] to predict profiles of spectral emissions for a range of T_e and $\bar{Z}$. Comparing these predicted spectra to experimentally recorded spectra enables estimation of T_e and $\bar{Z}$ based on the presence or absence of spectral lines. This estimate of $\bar{Z}$ is used to improved the estimate of n_i, and start another analysis iteration. The process is considered complete for the purposes of the results presented here when the estimated ion density is within $\approx 10\%$ of the value estimated in the previous iteration.

Magnetic field values at a position near the spectrometer view are determined by integrating signals from an array of magnetic pickup coils, the construction of which are detailed by Hsu et al. [25]. In addition to these interaction-region diagnostics, a photodiode array [25] is employed to capture emissions from jet propagation between the railgun nozzle and interaction region. Plasma jet velocity is estimated by calculating time-of-flight of features in both photodiode array and interferometer signals.

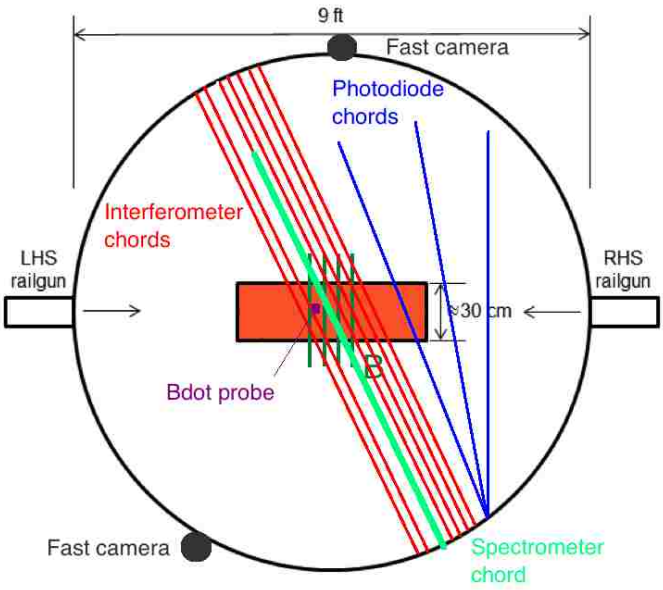

Figure 2.6: Notional top view of experiment interior with diagnostic viewing chords overlaid. The orange rectangle represents location of material from plasma jets as they near the transverse magnetic field (orientation in dark green). The multi-frame fast camera is at the top in this view.

Three photodiodes capture visible light from 1-cm field-of-view chords that intersect with the 'boresight' axis (the axis aligned with gun bores) at positions located at 61, 86, and 111 cm from the center of the spherical chamber. As plasma jets travel from the gun muzzle toward the center of the chamber, sharp increases in measured emission are interpreted to be the arrival of the leading edge of the jet, and jet velocity is estimated from the time delay in these features. An example of photodiode data is seen in Figure 2.8. Finally, an array of magnetic pickup coils affixed to the railgun nozzle captures magnetic field decay in the jet after the jet leaves the railgun bore [35].

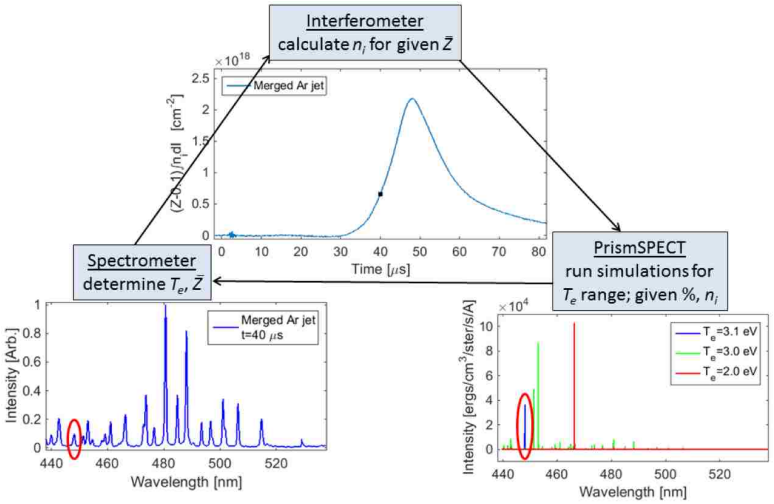

Figure 2.7: An iteration method is employed to determine T_e, n_i, and $\bar{Z}$. Interferometer data is used to estimate density, which in turn is used by PrismSPECT with an estimate of species mixture to estimate possible values of T_e. Comparison of PrismSPECT output with spectrometer data enables estimates of T_e and $\bar{Z}$, which allow more accurate estimations of n_i from interferometer data. These data are shown for example purposes and are not related to data presented elsewhere in this dissertation. Image from [44].

2.3 Interferometer Improvements

Previously, an interferometer was designed and constructed for use at the Plasma Liner Experiment [45, 48]. The 8-chord design was intended for use diagnosing plasmas relevant to plasma liner formation with electron densities in the range $10^{16} < n_e < 10^{19}$ cm^{-3}. In the existing system, a laser beam is split into probe and reference beams which are modulated to have a frequency shift relative to one another. As discussed in [48], after probing the plasma the beams are recombined and the resulting high-frequency beatwave is mixed with a signal at the original modulation frequency. This process yields signals related to the phase shift of the probe beam relative to the reference beam, and independent of the power in either

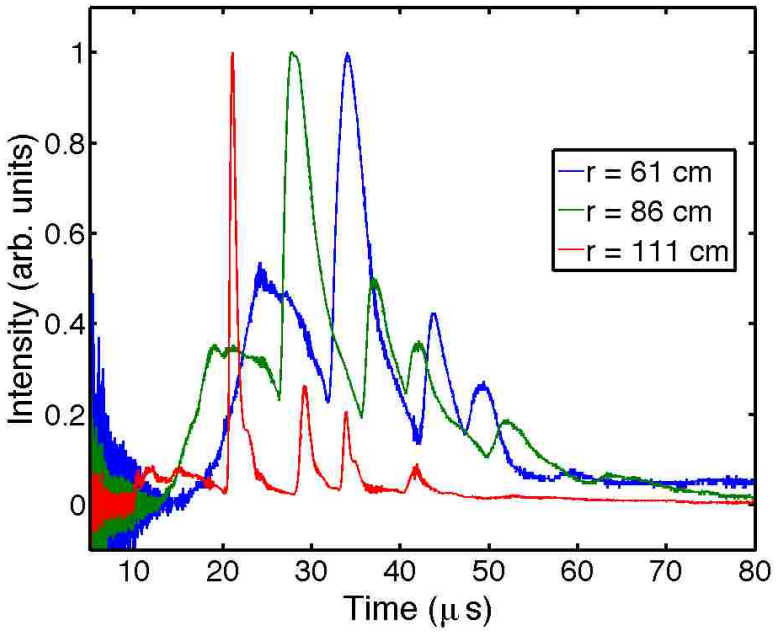

Figure 2.8: Time-of-flight features in photodiode traces enables velocity estimation. Seen here, amplitude-normalized traces of visible light from viewing chords located at $r = 61$, $r = 86$, and $r = 111$ cm show evidence the first jet arriving at $t = 21$, $t = 27$, and $t = 33$ μs, respectively.

beam. These signals, filtered prior to digitization, are the I and Q signals from the IQ mixer, where the I signal represents the cosine of the phase shift, and the Q signal represents the sine of the phase shift. Both I and Q continuously vary on slow (millisecond) timescales due to the effect of mechanical vibrations, with signals in the range ± 100 mV when the interferometer is well-tuned. The features in the signals due to the presence of the plasma are smaller amplitude (≈ 40 mV) higher frequency ($\sim 10^5$ Hz) fluctuations that are separated from the background mechanical fluctuations by an analysis algorithm.

The amplitude of the signal component attributable to the presence of plasma

depends on phase shift of the plasma, and thus its electron density. When the interferometer was employed to diagnose plasmas with densities in the range $10^{13} < n_e < 10^{15}$ cm^{-3}, the amplitude of the plasma component of the signals dropped to ≈ 10 mV. However, the bit noise amplitude of the digitizers is ± 2 mV, and the useful range of the signals for digitization is $\approx \pm 2000$ mV. In this regime, bit noise became an unacceptably large fraction of the signal of interest, and the decision was made to amplify the I and Q signals to improve the signal-to-noise ratio.

2.3.1 Design of Amplifiers

Two arrays of 8 amplifiers were constructed to amplify the raw I and Q signals with a gain of 6.1, which is capable of improving the signal-to-noise ratio by a theoretical maximum factor of 37.2 with the assumption that the only source of noise is bit noise. While in practice the improvement in signal-to-noise ratio was somewhat less, as other sources of noise became more important when amplified, the improvement was significant. In general terms, whereas prior to the addition of amplification, phase shift could be measured in practice with an error of $\approx \pm 1$ degree, the addition of the amplifiers reduced phase shift measurement error to $\approx \pm 0.25$ degree.

The amplifier model chosen for this purpose was the Analog Devices AD8130. This model was chosen due to its low noise, large bandwidth (up to 270 MHz), and stability at low gain. Evaluation boards (Analog Devices UG-133) were chosen to build the amplifier circuits on an expediency and cost basis. Parts were selected to build 16 amplifier circuits with gain 6.1 based on the Analog Devices datasheets. The amplifiers have differential inputs, which are unnecessary for use with the interferometer signals, and the spare input was shorted to ground and only a single input was used. The parts used to build the amplifiers can be seen in Table 2.1. An assembled array of 8 amplifier is seen in Figure 2.9.

Table 2.1: List of parts for interferometer amplifiers.

Qty.	Manufacturer	Part Number	Description
16	Johnson	415-0029-018	Coax cable assembly SMA
16	Analog Dev.	UG-133	Evaluation board
16	Analog Dev.	AD8130ARZ-REEL	Differential op-amp
4	CUI	VESD2-S12-D12-SIP	DC-DC converter -12/+12 V
2	Artesyn	DA12-120US-M	Wall wart power supply
16	Johnson	142-0701-801	SMA connector
32	Panasonic	ERJ-8ENF1001V	1.0 kΩ SMD resistor
16	Panasonic	ERJ-8ENF501V	5.1 kΩ SMD resistor
32	Vishay	1206ZT0R00	0.0 Ω SMD resistor
48	Vishay	1206FTD49R9	49.9 Ω SMD resistor
16	Bourns	3299W-1-102LF	1.0 kΩ trimming pot.
32	Kemet	T494D106K025AT	10 μF SMD tantalum cap.
32	TDK	C3216X7R1E105K085AA	1.0 μF SMD capacitor
48	TDK	C3216C0G1H104J160AA	0.1 μF SMD capacitor
16	Molex	0022112032	Molex header
16	Molex	0022012037	Molex connector housing
48	Molex	08-55-0131	Molex connector crimp pin

2.3.2 Interferometer Signal Processing

To process the raw interferometer data, three basic steps are taken. First the raw I and Q signals for each chord are smoothed with a 5 point moving average (boxcar) filter and the phase shift is calculated in the range $[-\pi, \pi]$ by computing the four-quadrant inverse tangent of Q/I. Second, the order of the phase is determined by checking for discontinuities, assuming the phase shift is zero at the beginning of the recorded data. The order of the phase shift is multiplied by 2π and added to the phase, to obtain the continuous phase evolution. Finally, the component of the phase caused by the presence of plasma along the chord is isolated from low-frequency mechanical vibrations or other sources of phase change by fitting either a polynomial or a spline to the portions of the phase before and after the time frame when plasma is present. This low-frequency phase fit is subtracted from the measured phase, and

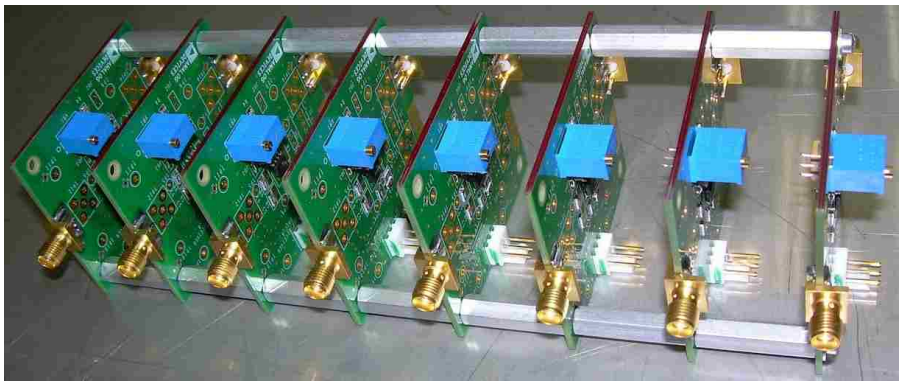

Figure 2.9: A set of 8 amplifiers to amplify the I and Q signals of four interferometer chords. Two such sets were built. The SMA terminals which are centered (near the camera) are the outputs and the offset SMA terminals are in the inputs (far from the camera).

the result is interpreted to solely represent phase shift caused by the presence of plasma. The first and last stages were altered to improve the accuracy of the phase shift calculation.

The raw data and the final stage in the analysis are shown in Figure 2.10. The mostly horizontal blue and green traces show the raw I and Q before they have been smoothed. The continuous phase evolution is shown as the cyan trace. A polynomial fit of the pre- and post-plasma low frequency phase component is shown as a magenta trace. To perform a spline fit (shown as noiseless blue trace), the continuous phase evolution is heavily smoothed with a 100 point boxcar filter (red trace) and subsample points (shown as blue circles) are selected along the smoothed trace through which to fit the spline. In place of a traditional spline, a PCHIP (piecewise cubic Hermite interpolating polynomial) was found to more smoothly and reliably fit to the low-frequency phase shift component. The low-frequency phase fit is subtracted from the continuous phase during the time period of interest and the resulting component of the phase shift resulting from the presence of plasma along

the chord can be seen in Figure 2.11.

It was necessary to improve the first stage of this process because of offset drift of the amplifiers. The original interferometer analysis code assumed that all of the I and Q signals had no offset. This meant that the presence of offset would change the amplitude of the calculated phase shift, dramatically so if the offsets were as large as ≈ 100 mV. To tackle this problem, a MATLAB routine was written that found the global minimum and maximum values of I and Q for each chord across a number of shots from a given day. This information is used by the main analysis routine to compute and subtract off the offset for each I and Q signal. These routines and an explanation of their use is found in Appendix A.

The final stage of the analysis was improved by the implementation of a spline-fit routine to replace the fitting of a polynomial to the low-frequency phase shift component. This greatly improved the fit quality and reliability of background phase shift subtraction. The analysis routine was altered such that the user of the code defines a period of time during which the plasma is expected to be present, and the code automatically smooths, subsamples, and fits a PCHIP to the subsamples in order to approximate the phase shift surrounding the user-defined time period, correcting for fit offset. For all shot ranges, subsample spacing is set to 50 μs for post-plasma times, and subsample spacing ranges from 18–40 μs for pre-plasma times, depending on the number of samples available prior to $t = 0$. The number of post-plasma subsamples increases with the length of time that the plasma is expected to be present, so that $m_{\text{subsamples}} = \text{floor}\,(1.5 \cdot \Delta t_{\text{present}}/50)$ for $\Delta t_{\text{present}}$ in μs. The smoothed phase shift is only used for the placement of the subsamples, and smoothing of the final plasma-only phase shift is an option left to the user (off by default). The code implementing this method can be seen in Appendix A.

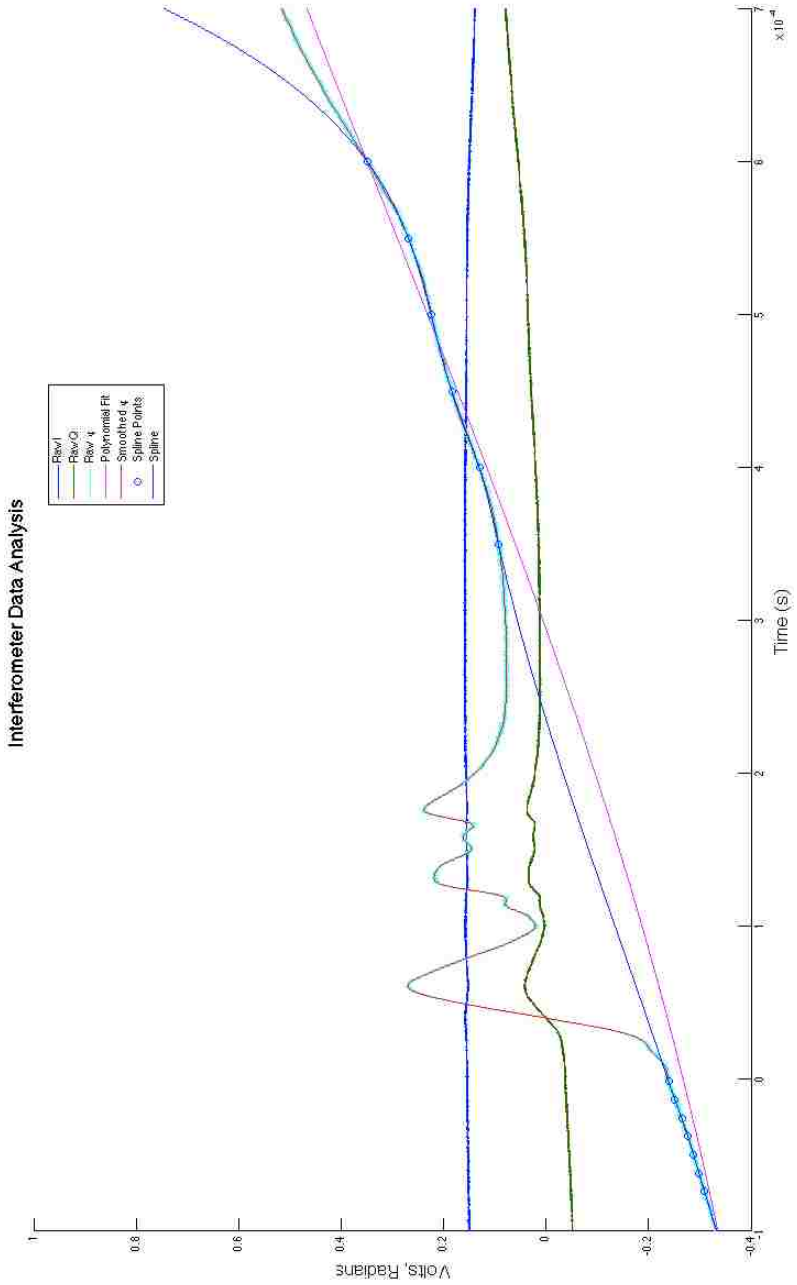

Figure 2.10: Overview of interferometer analysis, showing the raw I and Q signals, the computed phase shift, and the process of fitting curves to the low-frequency component. These data are shown for example purposes and are not related to data presented elsewhere in this dissertation.

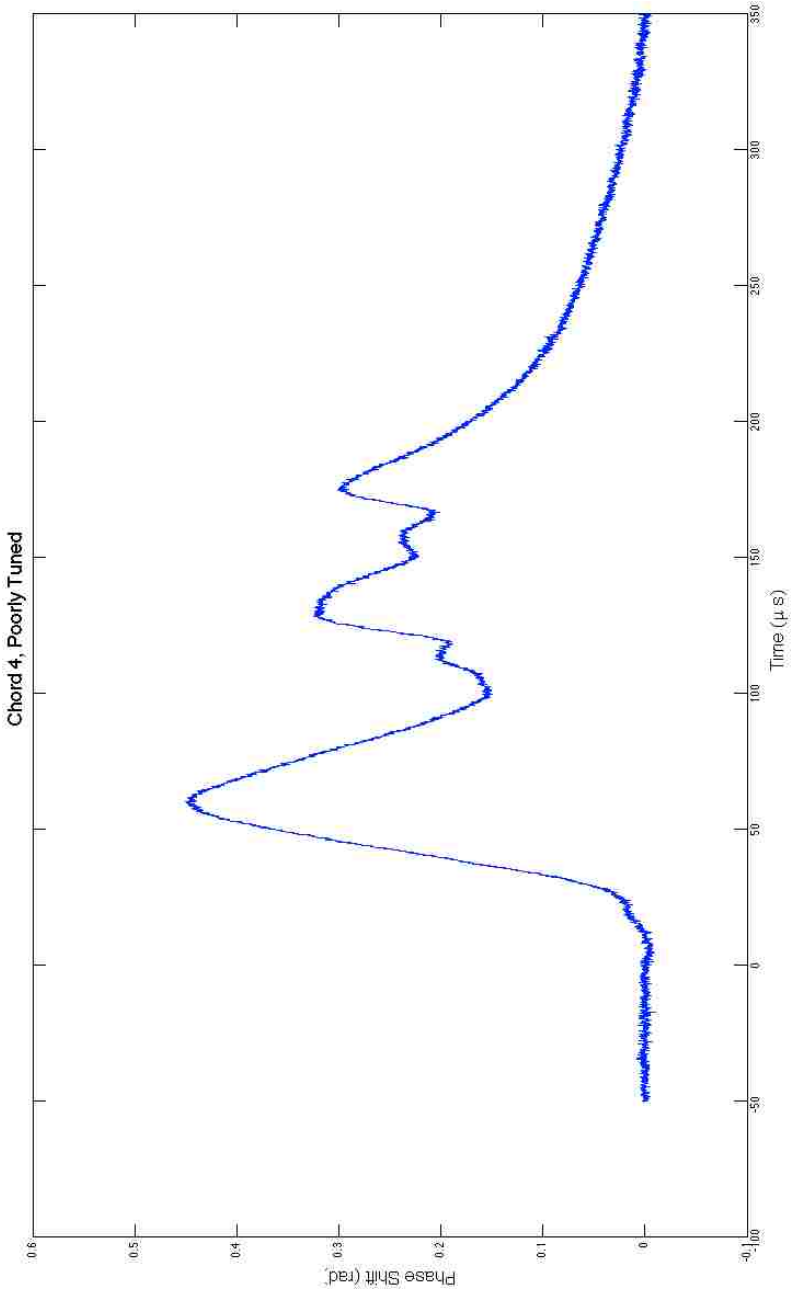

Figure 2.11: The final phase component from presence of plasma. This particular trace came from a chord with a poorly tuned fiber coupler. These data are shown for example purposes and are not related to data presented elsewhere in this dissertation.

Chapter 3

Schlieren Diagnostic

A schlieren imaging system, originally planned to diagnose plasma-liner formation experiments [25, 49] with electron densities in excess of $\sim 10^{16}$ cm^{-3}, was designed and constructed with the objective of dual use in regimes relevant to the laboratory study of shocks created during magnetized jet interactions. Such regimes were expected to have electron densities as low as $\sim 10^{14}$ cm^{-3}. As shown in this chapter, even though experiments were conducted in plasmas with densities $\approx 10^{14}$ cm^{-3}, the scale lengths of gradients in these plasmas were not short enough for the schlieren diagnostic to have sufficient sensitivity. While the diagnostic was not used for the experiments presented in this dissertation, information regarding the design and construction of the diagnostic is included here as a reference for its future use in higher-density regimes.

Schlieren imaging is a diagnostic technique that relies on refractive deflection of collimated light in a test medium to generate light and dark regions (referred to as 'contrast') at the imaging plane that have irradiance proportional to the gradient in the refractive index of the test medium. After the probe beam passes through the test medium, it is focused to a point prior to arriving at an imaging plane.

At this focal point, a portion of the beam is blocked which biases the contrast to appear for refractive gradients in the image with direction perpendicular to the edge blocking the beam. This imaging technique is distinct from shawdowgraphy, in which refractive gradients create contrast in the shadow of a scene, without the use of re-focusing and image cutoff edge for contrast enhancement. While shadowgraphy captures contrast which is sensitive to the Laplacian of refractivity ($\nabla^2 N$, where N is the index of refraction of the scene medium), schlieren techniques capture contrast which is sensitive to the gradient of refractivity (∇N). Schlieren imaging is more sensitive and thus more capable of revealing detail of flow phenomena than shadowgraphy, particularly for 'shallow' density gradients [50].

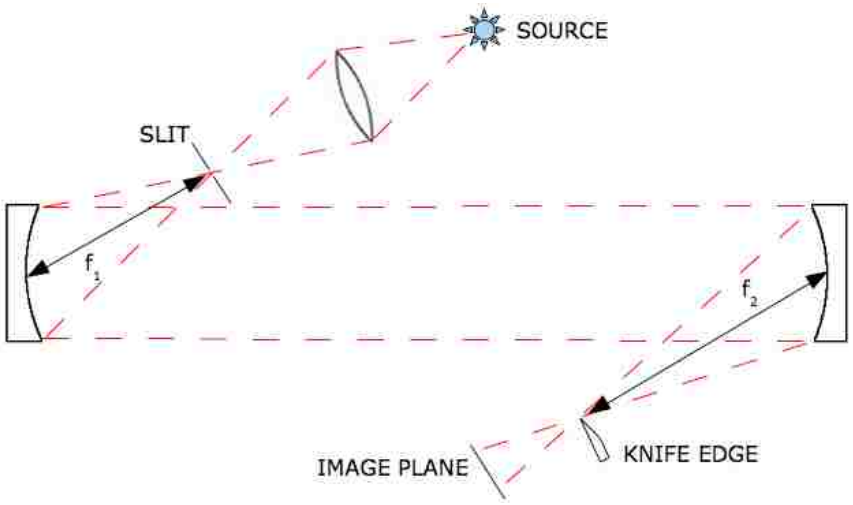

Figure 3.1: Notional layout of Z-configuration schlieren system. A slit is illuminated by a monochromatic light source and a knife edge is used to block light at focal point of post-test mirror.

When the scheme described above is executed using parabolic mirrors to collimate and refocus the probe beam, the result is a 'Z-configuration' schlieren system, notable for its compactness and low cost of construction. Figure 3.1 shows the notional layout of the Z-configuration schlieren system. Typically, light from a bright source

is focused on a slit placed near the focal point of a parabolic mirror which collimates the beam. The beam is then passed through a test medium before reaching a second parabolic mirror which re-focuses the beam to a point where a knife edge blocks all but a small portion of the probe beam. The unblocked beam passes on to the imaging plane, where the contrast of the resulting image is recorded. For a schlieren system of this type, the angular deflection ϵ in a direction y of a ray passing through the test medium is given by [50]

$$\epsilon_y = \frac{L}{N}\frac{dN}{dy}, \tag{3.1}$$

where L is the distance along the optical axis along which the probe ray passed through the test medium. When a portion of the image is blocked by a knife edge or other object at the focal point of the second mirror, the contrast C of the resulting image is given by [50]

$$C = \frac{f_2\epsilon_y}{a}, \tag{3.2}$$

where f_2 is the focal length of the second mirror and a is the height of the image which passes by the knife edge (original height of images less the amount blocked by the edge). Combining Equations 3.1 and 3.2 shows that the contrast in a schlieren image is proportional to the index of refraction gradient, seen here as

$$C = \frac{f_2 L}{aN}\frac{dN}{dy}. \tag{3.3}$$

In a plasma, the index of refraction N is usually dominated by free electrons, and for this case is given by [48]

$$N_e = \sqrt{1 - \frac{n_e}{n_c}}, \tag{3.4}$$

where n_e is the electron density and n_c is the cutoff density at the frequency of interest, which is given by $\epsilon_0 m_e \omega^2 / e^2$, where ϵ_0 is the vacuum permittivity, m_e is the mass of an electron, ω is the angular frequency of interest, and e is the charge of an electron. Taking the spatial derivative of Equation 3.4 reveals the relationship between electron density and refractive index gradients in a simple plasma,

$$\frac{dN_e}{dy} = \frac{-\frac{dn_e}{dy}}{2n_c\sqrt{1 - \frac{n_e}{n_c}}}. \tag{3.5}$$

According to Equation 3.3, image contrast is proportional to the gradient of refractive index, therefore image contrast is proportional to the gradient of electron density, inversely proportional to the cutoff density, and increases dramatically as the electron density approaches the cutoff density. For most cases, n_e/n_c is small, and the root term in the denominator of Equation 3.5 is approximately unity.

3.1 Schlieren Contrast Including Neutrals

To consider the case of a plasma that has a significant neutral gas density, the index of refraction of the plasma will no longer solely depend on the index of refraction of the free electrons. For this case the jets in the collisionless shock experiment are modeled as containing partially ionized hydrogen plasma of uniform mean ionization state $\bar{Z}$. Neutrals are assumed to be monatomic, with their electron in its ground state. Therefore two contributions to refractive index are considered; free electrons and neutral hydrogen atoms. Protons are neglected under the assumption that they are too massive to meaningfully contribute to the electric susceptibility of the jets.

For the free electrons, the refractive index was previously given in Equation 3.4. For the neutral hydrogen atoms, the Clausius-Mossotti relation states [51]

$$\frac{\epsilon - \epsilon_0}{\epsilon - 2\epsilon_0}\frac{M}{\rho} = \frac{4\pi N_A \alpha}{3}, \tag{3.6}$$

where M is the molar mass, ρ is the mass density, N_A is Avogadro's number, and α is the atomic polarizability. This can be rewritten in the following form to give an expression for the refractive index of the neutrals;

$$N_n = \sqrt{\frac{3 + 8\pi\alpha n_n}{3 - 4\pi\alpha n_n}}. \tag{3.7}$$

For a ground-state hydrogen atom, the atomic polarizability is theoretically 9/2 times a cubic Bohr's radii, which was converted to cubic meters to be compatible with the density units used in the calculation. The total refractive index of the plasma is a combination of the components from the free electrons and neutrals. The Gladstone-Dale relation indicates the relationship between the total index of refractivity and the constituents [52],

$$N_{total} - 1 = \sum_{i=1}^{m} k_i \rho_i = \sum_{i=1}^{m} \left(N_i - 1\right), \tag{3.8}$$

where k_i is the specific refractivity for a given species. Given this it can be seen that for the partially ionized hydrogen plasma,

$$N_{total} = N_e + N_n - 1, \tag{3.9}$$

and that

$$\frac{dN_{total}}{dy} = \frac{dN_e}{dy} + \frac{dN_n}{dy}. \tag{3.10}$$

Finally, by differentiating Equation 3.7 an expression is obtained for the spatial derivative of the refractive index,

$$\frac{dN_n}{dy} = \frac{18\pi\alpha\frac{dn_n}{dy}}{(3-4\pi\alpha n_n)^{\frac{3}{2}}(3+8\pi\alpha n_n)^{\frac{1}{2}}}, \tag{3.11}$$

where the neutral density $n_n = n_e(1-Z)/Z$. Further, by taking the result from Equation 3.5, Equation 3.10 becomes

$$\frac{dN_{total}}{dy} = \frac{-\frac{dn_e}{dy}}{2n_c\sqrt{1-\frac{n_e}{n_c}}} + \frac{18\pi\alpha\frac{dn_n}{dy}}{(3-4\pi\alpha n_n)^{\frac{3}{2}}(3+8\pi\alpha n_n)^{\frac{1}{2}}}. \tag{3.12}$$

In cases with sufficiently large neutral species densities, Equation 3.12 is used with Equation 3.3 to determine the relationship between schlieren contrast and electron and neutral density. For most cases, the second term on the right-hand side of Equation 3.12 is much less than the first, and a more simple (electron component only) relationship exists between density gradients and refractivity gradient.

3.2 Schlieren to Diagnose a Low Density Plasma

A schlieren system, originally conceived to diagnose high-density plasma liner experiments, was re-purposed in an attempt to detect collisionless 'cosmic' shocks in lower density plasmas, the nature of which are discussed in Section 1.2. The thickness of these shocks is thought to be on the order of the ion gyroradius. The initial experimental design suggested that ion gyroradii would range from 0.2 – 1.4 cm and that

experimental densities would be at least 2×10^{14} cm^{-3}. To proceed with development of the diagnostic, a design criteria was chosen that the system should be able to detect a 10% change in electron density over a single ion gyroradius. The design threshold for contrast detectability was chosen to be 5%, which is commonly considered the minimum practically detectable contrast [50]. Due to the unavailability of highly sensitive or otherwise contrast-enhancing detecting methods, the traditional minimum was adhered to.

Based on these considerations, and the relatively low density ($\sim 10^5\times$ lower than atmospheric) of the plasma to be diagnosed, obtaining sufficient contrast was determined to be the primary challenge. While the dominant contribution to the electric susceptibility (and thus index of refraction) is from free electrons, the lowest density neutral fluid flow features ordinarily observable by schlieren systems are at $\approx 100\times$ lower density than atmospheric. Based on the relationship in Equation 3.3, the controllable, sensitivity-influencing components of the system are the focal length of the second parabolic mirror, the amount of the image cut off by the knife edge, and via the index of refraction, the frequency of the probe beam. As seen in Equation 3.4, the index of refraction of the plasma (dominated by the contribution from free electrons) decreases as the cutoff density n_c decreases. Since the cutoff density is proportional to ω^2 of the probe beam, a low frequency (thus long wavelength) probe beam improves contrast sensitivity.

The longest wavelength illumination source available and practical for construction of the schlieren diagnostic was an infrared Nd:YAG Coherent Infinity 40-100 laser (1064 nm). A pair of two-meter focal length, 10-inch diameter telescope mirrors were employed to maximize contrast while maintaining affordability of the system. The knife edge cutoff was left as a tunable parameter. Using this equipment, and the previously described plasma parameters it was determined that a schlieren system would theoretically be capable of capturing electron density fluctuations at the

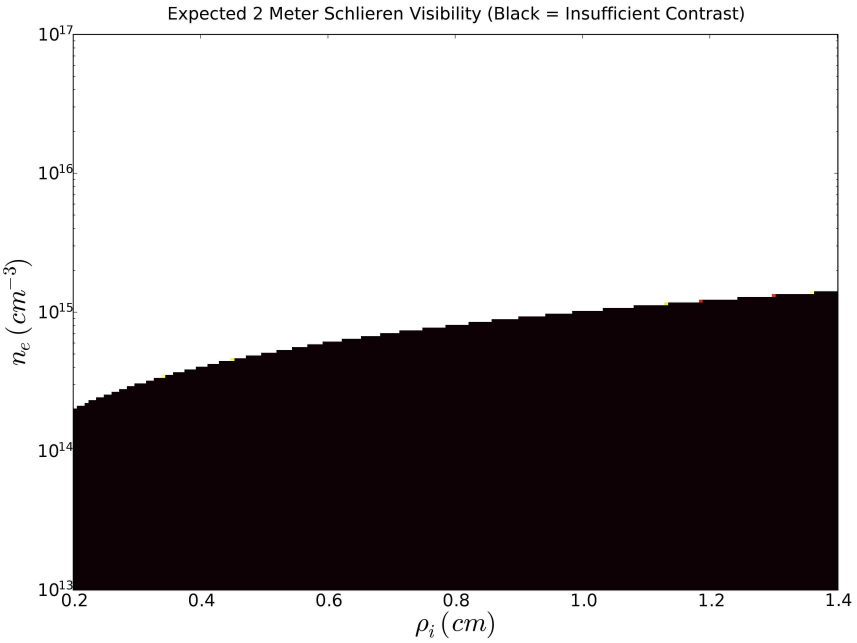

Figure 3.2: Useful parameter space of schlieren diagnostic. In black areas of the plot, contrast will be less than 5%, whereas in white areas of the plot, contrast will be greater than 5%, assuming second mirror focal length $f_2 = 2$ m, $L = 0.1$ m, and $a_{\min} = 40$ μm.

shock front. To study the theoretical performance of the diagnostic in the expected parameter space the contrast was computed for a range of densities and ion gyroradii, as seen in Figure 3.2. From this contour, it can be seen that for gyroradii of a few millimeters, contrast is sufficient for electron densities as low as 2×10^{14} cm^{-3}, whereas for gyroradii longer than a centimeter, densities in excess of 10^{15} cm^{-3} are necessary to detect density gradients.

To proceed with design and construction of the diagnostic an Apogee Alta U1109 imaging unit, intended to be a telescope camera system, was readily available at no cost. From a technical perspective, this unit was chosen because the sensor, a Hamamatsu S10140-1109, features a remarkable 8% quantum efficiency at 1060 nm,

an unprecedented efficiency for a readily-available silicon CCD. The Apogee camera contains no internal optics, solely consisting of a sensor, shutter, trigger, and readout capability. An external enclosure was constructed to place two filters in the path of the beam prior to arriving at the CCD. The first filter is a bandpass filter, that only allows light at the laser wavelength to pass into the otherwise light-proof aluminum enclosure. Immediately prior to the camera shutter is a mount for a neutral density filter used as necessary to prevent damage to the sensor by the laser.

3.3 Construction of Schlieren System

In addition to the Alta camera and the Infinity laser, numerous other items were necessary for the schlieren diagnostic, including a translatable knife edge, optical mounts for parabolic mirrors, flat beam-folding mirrors for which custom mounts were necessary to direct the beam through the spherical vacuum chamber, translation stage optics to align, attenuate, and diverge the probe beam, and a visible-wavelength alignment system. The optical components necessary are shown in Table 3.1. In the following subsection, the systems that these components comprise are described.

To cut off a portion of the image at the focal point of the second mirror, a razor blade was rigged in a lab clamp positioned atop a micrometer-adjusted linear translation stage. This enables very fine control over the cutoff, and consequently the brightness and contrast of the schlieren image, as seen in Figure 3.4. Optical mounts for the parabolic mirrors were salvaged, however mounts for the flat 8 by 10 inch folding mirrors necessary to direct the probe beam through the spherical vacuum chamber were designed and fabricated. The design for these mounts was complicated by the geometry of the experiment. Since the probe beam needed to be directed through the large, spherical vacuum chamber at a level nearly two meters above the floor of the lab, custom rotating and tilting mounts were developed. Diagnostic

Table 3.1: List of parts for schlieren system.

Qty.	Manufacturer	Part Number	Description
3	Edmund	NT40-067	Large flat mirrors
2	RF Royce	CM-10.8	Conical section parabolic mirrors
1	Edmund	A43-717	Opal diffuser
1	Edmund	A49-157	Ground glass diffuser
1	Edmund	NT55-292	IR indicator card
1	Edmund	48-766	25mm focal length lens
2	Newport	9912	Bases
1	Newport	9607	Post holder
1	Newport	9608	Post holder
1	Newport	SV-0.5	Adjustable width slit
1	Thorlabs	PT1	Single axis translation stage
1	Edmund	NT63-410	OD 1.0 NIR ND filter 25.4 mm
1	Edmund	NT62-874	1064 nm bandpass (3 nm) filter 25.4 mm
1	Thorlabs	KM100T	Kinematic Mount
1	Thorlabs	CPS532	Diode Laser
1	Thorlabs	LDS5	Laser power supply
1	Newport	9891	Flipper mount
1	Edmund	NT83-485	1” dia. mirror
2	Edmund	66-518	125 mm rotary stage
1	—	—	Lab clamp
1	—	—	Razor blade
1	—	—	Beamsplitter, 25.4 mm

access was provided via 11-inch ports located high above the optical tables that the launch and imaging stages were mounted to. To effectively direct the probe beam through these ports, the so called ‘periscope’ mounts were required to azimuthally rotate around the ports and tilt at an angle relative to the axis of symmetry of each port. The final design of the components of these mounts is shown in Appendix B. Attached to the periscope mounts are lightweight rectangular mirror mounts and associated mirrors, shown in Appendix C. A photograph of the complete assembly is shown in Figure 3.3.

The primary purpose of the schlieren launch stage, seen in Figure 3.5 is to direct

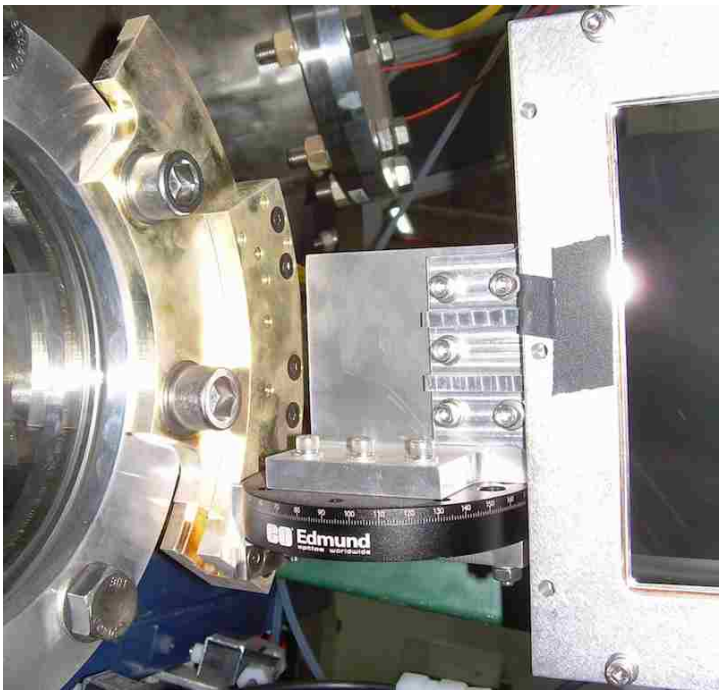

Figure 3.3: Each periscope mount consists of the custom parts shown in Appendix C as well as an Edmund 66-518 rotary mount.

a diverging beam toward the first collimating parabolic mirror. This beam must originate from a point one focal length from the mirror in the longitudinal direction and slightly offset from the axis of symmetry of the parabolic mirror. Furthermore, the amount of energy in each laser pulse must be large enough to obtain a useful signal at the detector but not large enough to pose an eye safety hazard from specular reflections of the expanded beam. To accomplish this, the beam from the laser is first attenuated with a beamsplitter that directs 90% of the beam energy into a beam dump and transmits the remaining 10% to a lens with a 25 mm focal length. This lens expands the beam such that it has an approximate diameter of 250 mm at a range of 2000 mm. At this distance, the beam encounters the parabolic mirror and is collimated at a diameter of $\approx$ 200 mm, and directed through the vacuum chamber

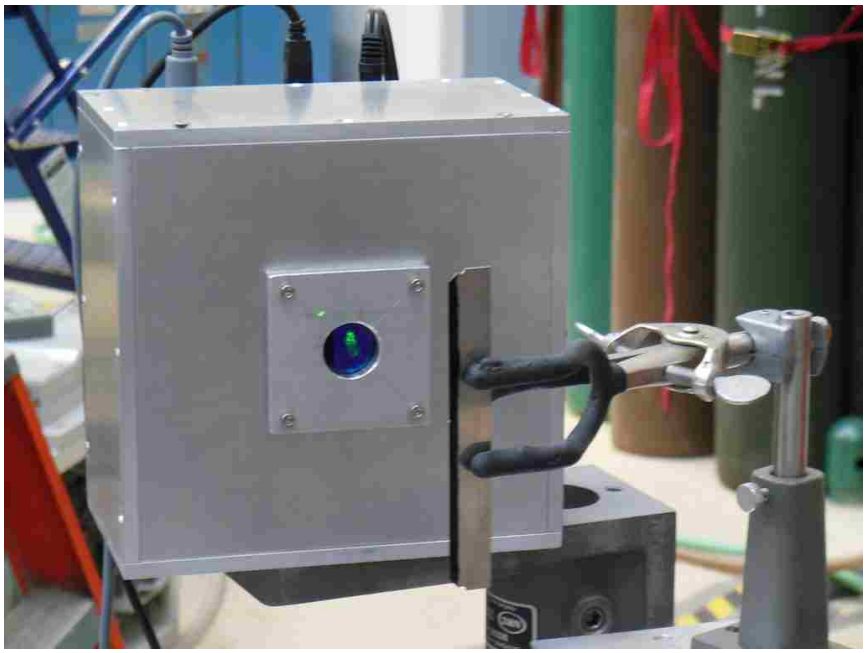

Figure 3.4: The Apogee imaging unit is located on the back of the aluminum enclosure containing two filters. The knife edge mount is translatable transverse to, and along the beam at the focal point of the second parabolic mirror. The green (532 nm) alignment beam is incident on the knife edge and filter.

by a series of flat folding mirrors. Additionally, to aid in alignment of the system, a green alignment diode laser was added to the launch stage. The alignment laser can be seen below the word "splitter" in Figure 3.5. The alignment beam is directed toward a 'flippable' mirror that is usually in the down position, allowing the infrared beam to pass. When the mirror is in the up position, it blocks the infrared beam and instead directs the green alignment laser down the same optical path as the infrared beam.

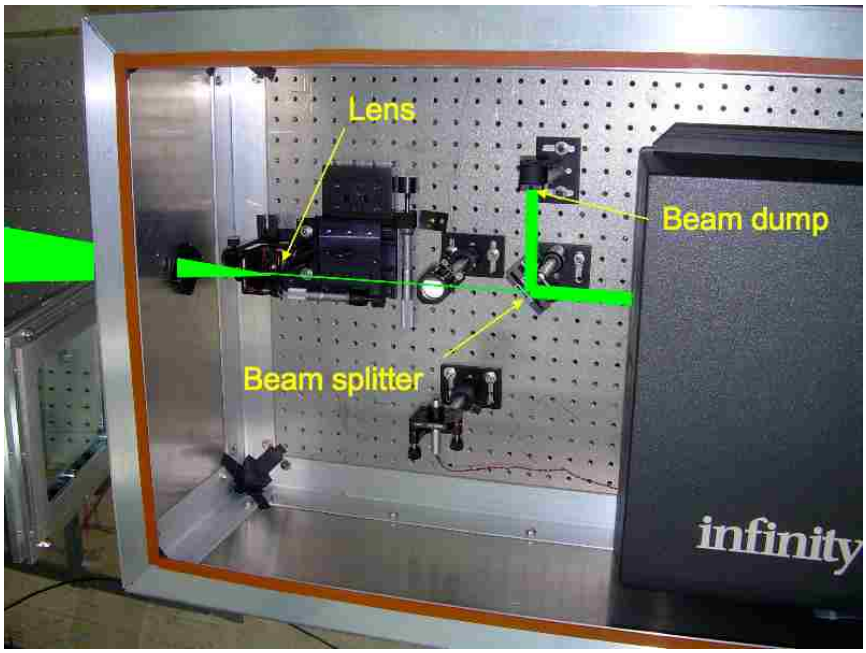

Figure 3.5: Layout of schlieren system launch stage. Laser energy is reduced with a beamsplitter before a lens diverges the beam as it propagates toward the first collimating parabolic mirror.

3.4 Optical Aberrations

As mentioned previously, the optical path of the PLX schlieren system is rather convoluted when compared to a traditional z-configuration schlieren system. After the beam encounters the first parabolic mirror, three turning mirrors redirect the beam through the spherical vacuum chamber and to a separate optical table which contains the second parabolic mirror, knife edge, and the imaging unit. The coma aberration arises when a parabolic mirror fails to focus collimated light to a point due to the collimated light being incident to the mirror at an angle relative to the axis of the parabola [50]. Traditional z-configuration schlieren systems (Figure 3.1) are usually immune to coma aberration by virtue of the symmetry of the geometry—

coma aberration induced at the first parabolic mirror is cancelled by the equal and opposite coma at the second mirror. Due to the optical path at the experimental facility, such symmetry was prohibitively difficult to achieve. Pains were taken to reduce coma aberration by moving and elevating elements of the system as necessary, but coma aberration was never completely expunged from the system, and as a result the knife edge cutoff darkened and enhanced contrast of some portions of the image more than others.

3.5 Alignment

To align the green alignment laser to the infrared beam, the diverging lens was removed from the launch stage, and a beam block was placed at a location ≈ 1.7 m from the laser enclosure. A piece of thermally reactive paper was affixed to the beam block, and a plastic beam tube was installed between the beam block and the laser enclosure, as seen in Figure 3.6. Then, the infrared laser was fired, making a mark on the laser paper, and the flippable mirror was placed in the up position and the green laser was directed toward the mark on the paper by adjusting the pan and tilt on the flippable mirror. Next, a piece of reactive paper was placed at the inside of the laser enclosure, the flippable mirror was placed in the down position, and the infrared laser was fired again, making another mark. This time, after raising the flippable mirror, the alignment beam was directed to the mark by adjusting the pan and tilt on the alignment laser mount itself. This process was repeated until the alignment beam met both marks made on the papers without any adjustment.

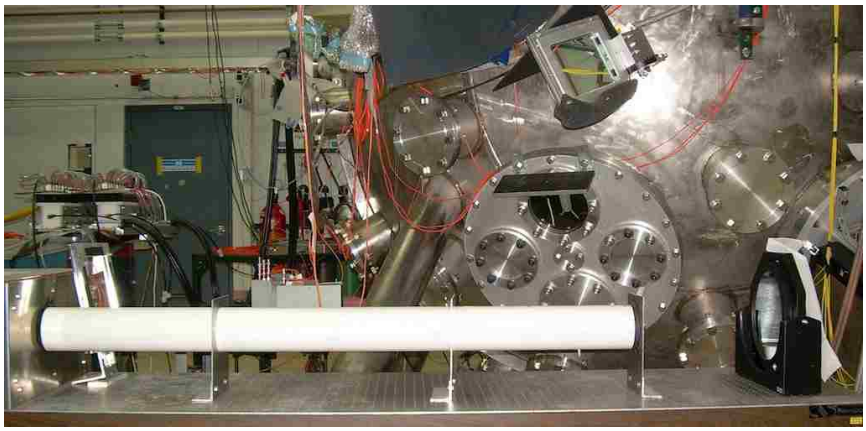

Figure 3.6: Position of beam tube for schlieren alignment. The laser enclosure appears at the left side of the photograph and the first parabolic mirror is visible on the right side.

3.6 System Trials

The system was aligned as described above and directed at candles placed in the beam path, as seen in Figure 3.7. Schlieren images were observed both with the alignment laser and using the infrared laser. The system was tuned to improve the quality of the schliere, to a moderate degree of success with the alignment laser, and less so with the infrared laser. Using the alignment laser, coma aberration was drastically reduced, and the presence of reflections propagating in the probe beam was also eliminated.

However, serious challenges remain with the infrared laser. Perhaps due to the lack of a spatial filter, beam illumination is very uneven, unlike the alignment laser. This was attempted to be compensated for with the use of image processing techniques with some success, but changes in beam intensity from shot-to-shot complicated such efforts. Furthermore, diffraction patterns that were visible but not extreme with alignment laser appeared in a pronounced fashion in images captured

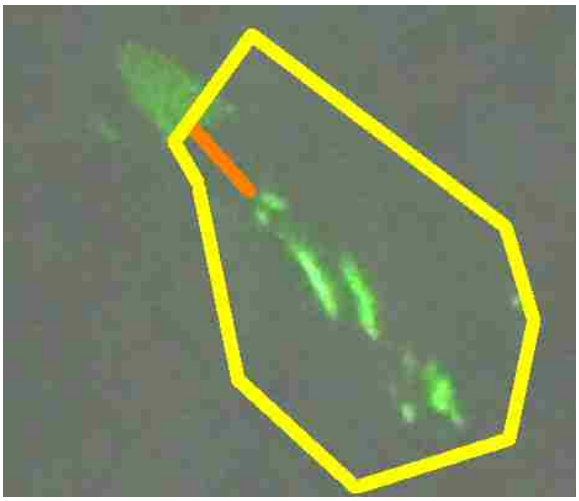

Figure 3.7: Schlieren image of candle plume with green alignment laser. This photograph is of a projection onto a piece of black cardboard, captured during tests of the system. During operation this image would be projected directly onto an imaging sensor. The position of the candle is marked in orange, and the boundaries of the image are seen in yellow. Note the difference between scene and image vertical.

of the infrared beam. Attempts to diagnose or correct these issues were hampered by the low beam energy precluding the use of available IR-sensitive cards or paper to visually check the alignment and illumination evenness of the infrared beam.

Since construction was completed, the system has not been used to diagnose a plasma, as plasmas with sufficiently high density and sufficiently small gradient scale lengths were not generated in experiments. Figure 3.8 shows the parameter space of plasmas in the experiment (red oval) overlaid on the sensitivity contour map shown earlier.

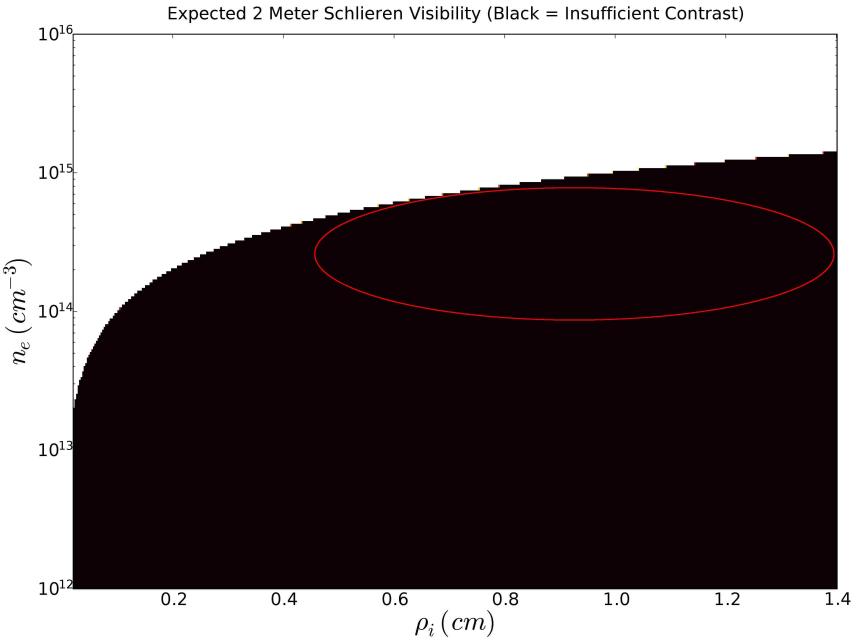

Figure 3.8: Useful parameter space of schlieren diagnostic overlaid with experimental operating space (in red). The x-axis of this plot can be read as "gradient scale length", to generalize to cases where a magnetic field was not present.

3.7 Image Processing

Simple image processing routines were developed to differentiate between contrast from refractivity gradients and unevenness of beam illumination. The approach was to subtract a background image from a scene image, and filter the resulting difference with a Fourier-space filter to remove beam speckle and diffraction pattern artifacts. This enabled schlieren and shadowgraph images of a test candle to be captured unambiguously, as seen in Figure 3.9.

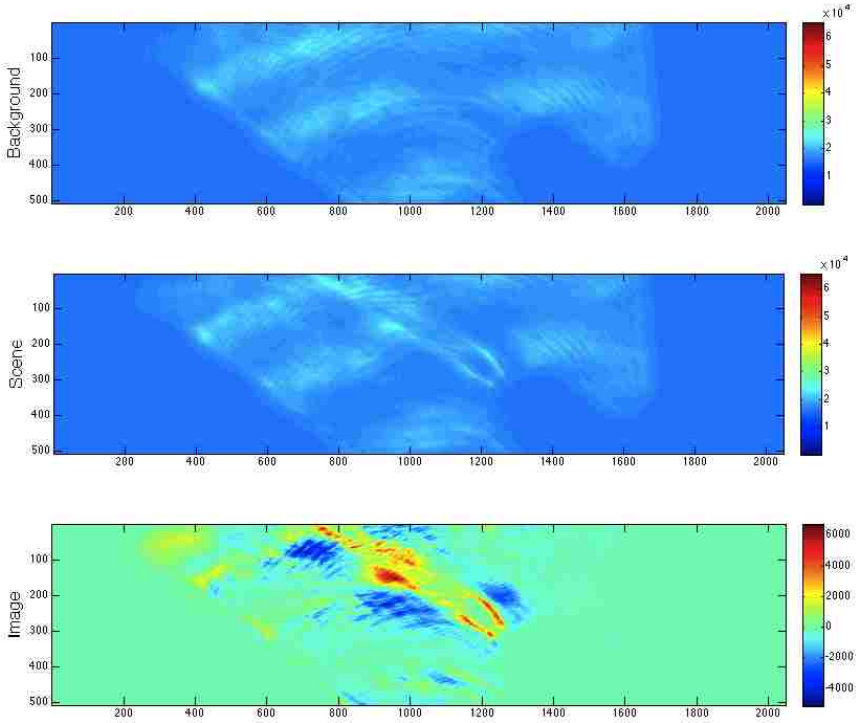

Figure 3.9: Shadowgraph (knife edge is fully withdrawn, no cutoff effect) of candle in 1064 nm laser light. The candle is visible as a shadow in the lower right part of each image. The top is a background with no flame, the center is a scene image with a candle flame, and the bottom is the difference. While the presence of the flame is discernible, artifacts from the presence of diffraction patterns mar the image.

Chapter 4

Rayleigh–Taylor Instability at a Decelerating Plasma Interface

During the course of experiments of the type shown in Figure 2.5, an unmagnetized jet collided with a stagnated magnetized plasma, and instabilities were observed which appeared to be stabilized by the presence of magnetic field. In this chapter these results are presented and the instability is shown to be consistent with the Rayleigh–Taylor instability in a regime where both magnetic and viscous stabilization are relevant.

4.1 Observations of Rayleigh–Taylor Growth

When the second jet arrives at the interaction region the growth of fingers are observed in visible emission as the material in the newly arrived jet encounters the stagnated plasma, shown in Figure 4.1. A portion of the Helmholtz coils are visible as arc-shaped structures in the right part of each frame, where the right-hand coil is closer to the camera than the left-hand coil. The stagnated plasma is dark (not

emitting), and located in the vicinity of the spectrometer view, which is in the center of the Helmholtz coils. The second jet is seen as the bright material moving from right to left. The location of interferometer chords at the mid-plane of the Helmholtz coils are shown as small white squares. The chords are not situated normal to the mid-plane, rather from the perspective of the images in Figure 4.1, the chords originate from the lower left of the visible region and into-the-page and and terminate at a location above, to the right, and out-of-the page. The location of the intersection of the spectrometer view with the midplane is shown as a circle, and the absolute location of the magnetic probe is shown as a 'plus' (+) symbol.

As the incoming jet impacts the stagnated plasma the jet slows down. Rayleigh–Taylor -like instability fingers are clearly seen in the images. To estimate the acceleration to which the interface is subject, the location of a bubble is tracked in successive images, as shown in Table 4.1. Additionally, the location of a spike is tracked in successive images, shown in Table 4.2. In both tables, difficulties in precisely choosing the location of the bubble and spike cause erratic calculations of corresponding velocities. The resolution of the images was such that each pixel corresponds a distance of only 0.075 cm, affording a theoretical velocity resolution of $\approx$ 1500 m/s. Rather, difficulties arose from changes in exposure of successive images, the presence of background reflections, and general lack of clarity. This meant that in practice feature locations were picked within only 3-4 pixels giving a velocity resolution of only 4500–6000 m/s. In an attempt to determine the largest possible acceleration at the interface the kinematic relation $v_f^2 = v_i^2 + 2a\Delta x$ was employed to determine the average acceleration between the position of the largest and smallest inferred velocities. This result is shown in the right-most column of both tables, and for both bubbles and spikes is $\approx 10^9$ m/s^2. This calculation of the average acceleration over the sequence of frames is most sensitive to the initial velocity, which has the largest magnitude (since $a \sim v_i^2$). For this reason, all physically relevant approaches to calculating acceleration based on the data in Tables 4.1 and 4.2 result

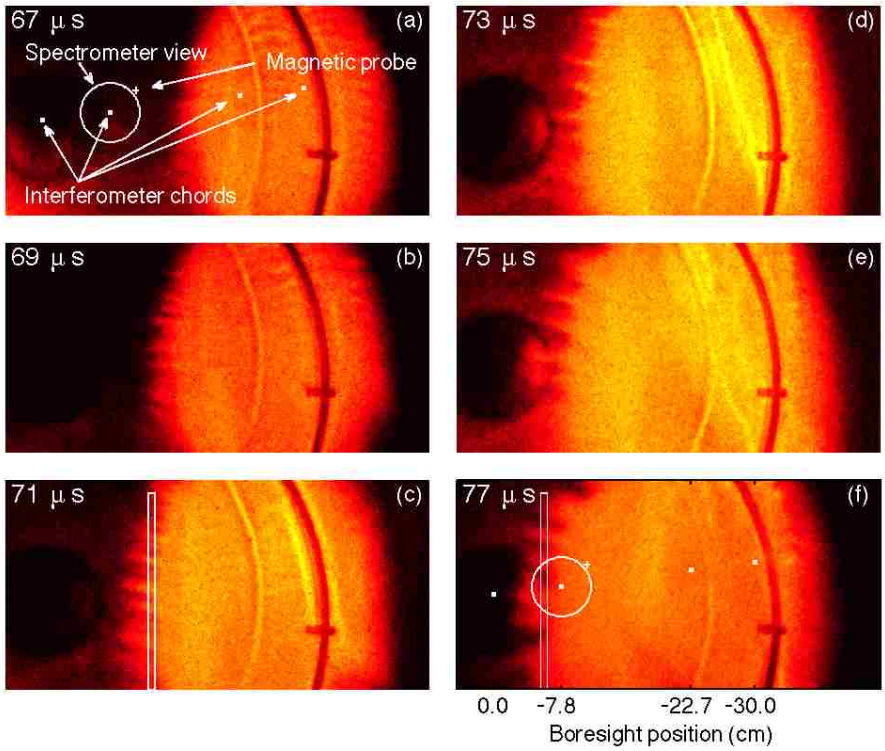

Figure 4.1: Six frames from a single shot capturing instability growth over 10 μs as the second jet enters the region containing stagnated plasma. The location of diagnostic measurements are called out in frame (a), and reiterated in frame (f). The arc-shaped structures visible in the right side of each image are the Helmholtz coils. Chord positions are measured with respect to the boresight axis, which is aligned with the railgun bore.

in an acceleration magnitude $O \sim 10^9$ m/s^2.

As mentioned previously, time-of-flight of features in photodiode and interferometer traces are used to estimate jet velocity. Examples of these features are found in Figures 2.8 and 4.5. To corroborate the acceleration estimate based on the camera images, an estimate is made of the acceleration required to stop the jet over a distance corresponding to the length scale of the interaction. For the purposes of this estimate, the velocity of the incoming jet is assumed to be lost in a distance of

Table 4.1: Estimation of velocity and acceleration from bubble position

Time (μs)	Pixel	Location (cm)	Velocity (m/s)	Acceleration (m/s^2)
67	259	-15.2	—	—
69	215	-11.9	16500	—
71	181	-9.3	12800	—
73	152	-7.1	10900	—
75	107	-3.8	16900	—
77	88	-2.3	7130	-1.17×10^9

Table 4.2: Estimation of velocity and acceleration from spike position

Time (μs)	Pixel	Location (cm)	Velocity (m/s)	Acceleration (m/s^2)
67	303	-18.5	—	—
69	265	-15.6	14300	—
71	229	-12.9	13500	—
73	194	-10.3	13100	—
75	175	-8.8	7130	-1.19×10^9
77	147	-6.8	10500	—

30 cm, which corresponds to half the diameter of the region containing the applied magnetic field. Jet velocity was characterized for the railguns in previous study [43] and was found to be in the range 40–70 km/s based on photodiode and interferometer data for the operating parameters of these experiments. This suggests an acceleration ranging from 2.7–8.2 $\times$ 10^9 m/s^2. While this estimate is somewhat higher than the image-based estimates, both are within an order of magnitude, and 10^9 m/s^2 is taken to be the nominal acceleration for the purposes of analyzing the observed phenomena.

The view of the frames in Figure 4.1 is nearly perpendicular to the plane of each coil, thus the view is oriented nearly parallel to the vacuum magnetic field generated in the center of the coils. In the context of the dynamics of jet interaction, the initially applied field is steady state, but the arrival of the first jets causes the field

to evolve on microsecond timescales in the 30 μs leading up the observed phenomena. An insertable magnetic probe is placed in the interaction region (position indicated in Figure 4.1) to measure the evolution of up to three local magnetic field components during the interaction of the second jet with the stagnated plasma. Magnetic field directions are reported with respect to the coordinate system of the Helmholtz coil, such that 'axial' refers to a direction nearly into-and-out-of-the-page in the images, 'azimuthal' refers to a direction nearly vertical, and 'radial' refers to a direction nearly horizontal. Data from this probe, seen in Figure 4.2, indicate that the stagnated plasma from the initial interaction becomes magnetized prior to the arrival of the second jet. In the 12 μs prior to the arrival of the interface at the location of the probe, the axial magnetic field in the stagnated plasma increases to the steady-state magnitude, approximately 300 G. In the few microseconds prior to the arrival of the interface, the magnitude briefly peaks at 370 G, suggesting some field compression immediately prior to the arrival of the still-supersonic jet. As the leading edge of the second jet sweeps across the position of the magnetic probe, the measured magnetic field drops dramatically, from over 300 Gauss to only a few Gauss by the time of the last camera image. This rapid drop suggests strong advection of magnetic field by propagation of the field-excluding second jet.

As reported in previously published work [35], magnetic fields of 750 G are present at the gun nozzle, and decay with an e-folding time of 5.6 μs which would suggest a magnitude of $\approx$ 10 G by the time of arrival at the interaction region. Measurement of local magnetic field upon jet arrival with the insertable $\dot{B}$ probe (location specified in Figure 4.1) without energizing the Helmholtz coils suggests that there is no advection of magnetic field with the second jet. Thus for the purposes of this investigation, the second jet is considered to be unmagnetized as it arrives in the vicinity of the Helmholtz coils.

Spectra snapshots are collected over a series of shots covering times both before

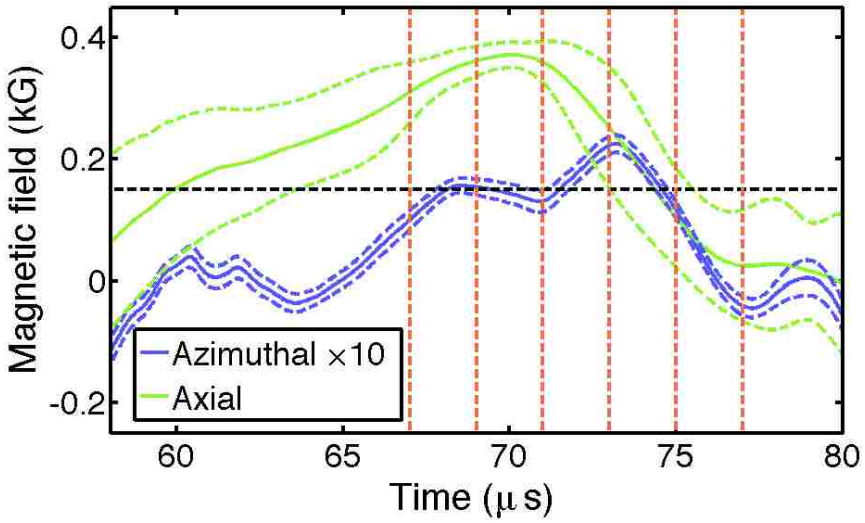

Figure 4.2: Signals from the insertable $\dot{B}$ probe are integrated and added to the steady-state field to determine magnetic evolution. The coordinate system references the Helmholtz coil, thus the axial component is approximately into-and-out-of-the-page in Figure 4.1, while the azimuthal component is nearly vertical. The radial component (not shown here) show insignificant activity during the time frame of interest. The vertical dashed lines indicate the beginning of each exposure in Figure 4.1. The horizontal dashed line corresponds to a 15 G field measured by the azimuthal probe.

and after the interface is in the location of the spectrometer view. Comparing PrismSPECT spectral calculations with these experimental spectra enables bounding of T_e in both the stagnated plasma and second jet. Prior to the arrival of the second jet, the appearance of line emission near 497.2 nm and the lack of line emission at 520.8 nm indicate a peak $T_e \approx 2.3$–2.4 eV in the stagnated plasma, an example of which is seen in Figure 4.3. After the interface passes the spectrometer view, the appearance of line emission near 490.6 nm and the lack of line emission at 453.1 nm indicate a peak $T_e \approx 2.7$–2.8 eV in the second jet, an example of which is seen in Figure 4.4. For the range $2.3 < T_e < 2.8$ eV the corresponding values of mean ionization state are calculated using PrismSPECT to be $1.2 < \bar{Z} < 1.6$.

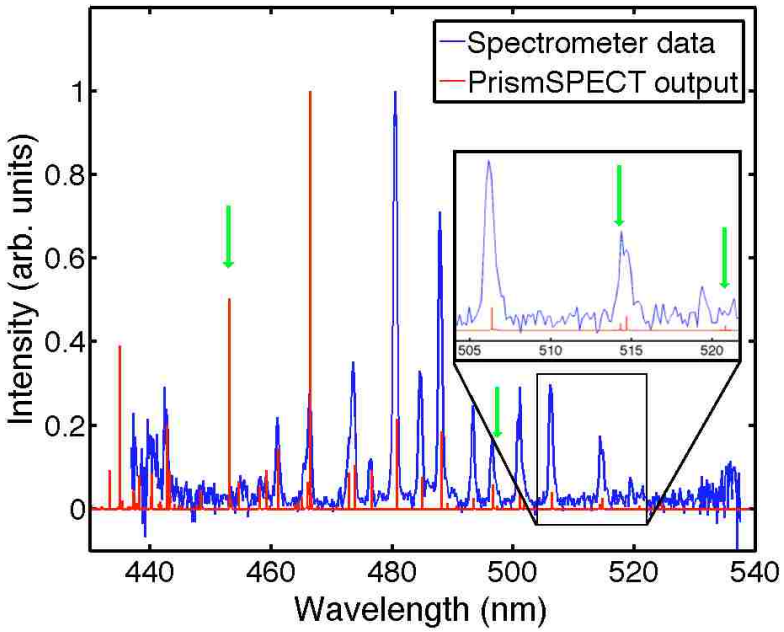

Figure 4.3: Spectra captured from a shot (#3330) with the same parameters as that shown in Figure 4.1. Prior to the arrival of the second jet ($t = 65$ μs) spectra shows emission consistent with $T_e \approx 2.3$–2.4 eV. Example PrismSPECT output is prediction of line emission wavelengths consistent with $T_e = 2.8$ eV.

Seven chords from the 8-chord interferometer are used to measure the spatial and temporal evolution of phase shift $\Delta\Phi$ from free and bound electrons in the plasma [45, 46]. The chord-integrated density is related to the measured phase shift by the expression $\int n_{\mathrm{tot}} dl = \Delta\Phi / \left[C_e \left(\bar{Z} - Err\right)\right]$, where n_{tot} is the total ion-plus-neutral density, $C_e = (\lambda_{\mathrm{probe}} e^2)/(4\pi\epsilon_0 m_e c^2) = 1.58 \times 10^{-21}$ rad $\cdot$ m^2 is the phase sensitivity to electrons, $\lambda_{\mathrm{probe}} = 561.3$ nm, and $Err \lesssim 0.08$ is an upper limit on the contribution from bound electrons [35], which for cases of interest is small compared to $\bar{Z}$. The temporal evolution of phase shift of each chord is computed and averaged over a number of shots, as seen in Figure 4.5. Spatial profiles are determined by comparing the phase shift of different chords at a given time. Figure 4.6 shows the spatial profile

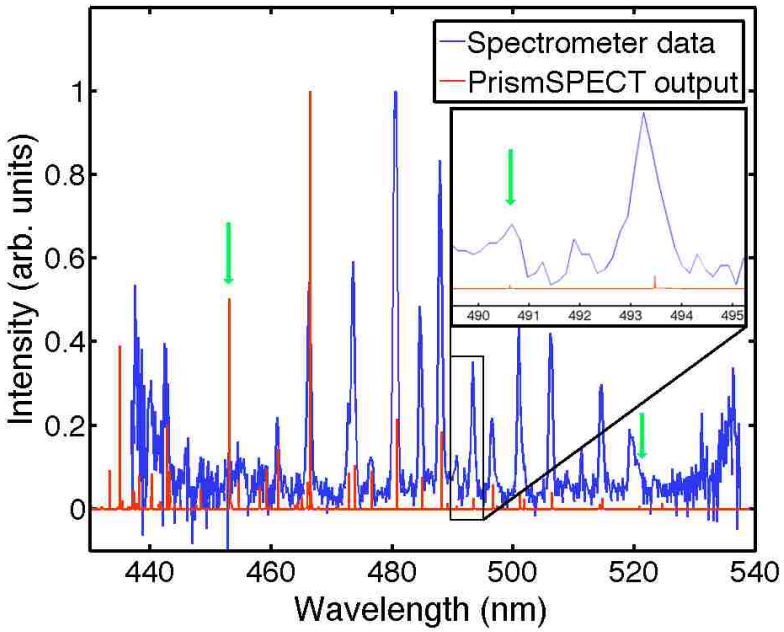

Figure 4.4: Spectra captured from a shot (#3332) with the same parameters as that shown in Figure 4.1. At the time of the arrival of the second jet to the spectrometer viewing chord ($t = 67$ μs) spectra shows emission consistent with $T_e \approx 2.7$–2.8 eV. Example PrismSPECT output is prediction of line emission wavelengths consistent with $T_e = 2.8$ eV.

of $n_{\text{tot}} \left(\bar{Z} - Err\right)$ (with an assumed chord length of 30 cm) at time $t = 77$ μs, from which an experimental number density $n_{\text{tot}} \approx 10^{14}$ cm^{-3} is inferred.

The progression of images in Figure 4.1 appears to show an increase in wavelength as the interface penetrates further into the stagnated plasma. To quantify this change in wavelength, ten adjacent lineouts are added together from the region of frames (c) and (f) containing the left edge of the second jet (indicated in the figure). These summed lineouts are shown in Figure 4.7, and clearly show that 10 fingers appear at $t = 71$ μs, while in the same vertical height, only 6 fingers appear at $t = 77$ μs. While the displayed length scales are uncorrected for parallax, this effect is computed to

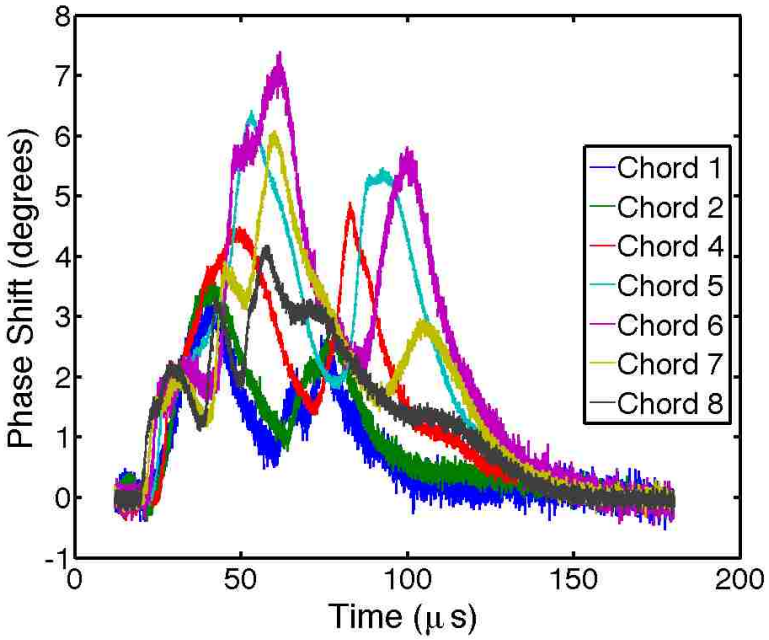

Figure 4.5: Temporal evolution of chord-integrated phase shift averaged over 28 shots. A chord length of 30 cm is estimated from camera images for all seven interferometer chords. Early-time rise in phase shift between adjacent outer chords is interpreted as a feature indicating jet leading edge arrival.

be negligible, as the camera is situated approximately two meters from the jet, and the camera line-of-sight is nearly perpendicular to jet propagation. This increase in wavelength over 6 μs suggests that a stabilizing mechanism may be damping the growth of short-wavelength modes.

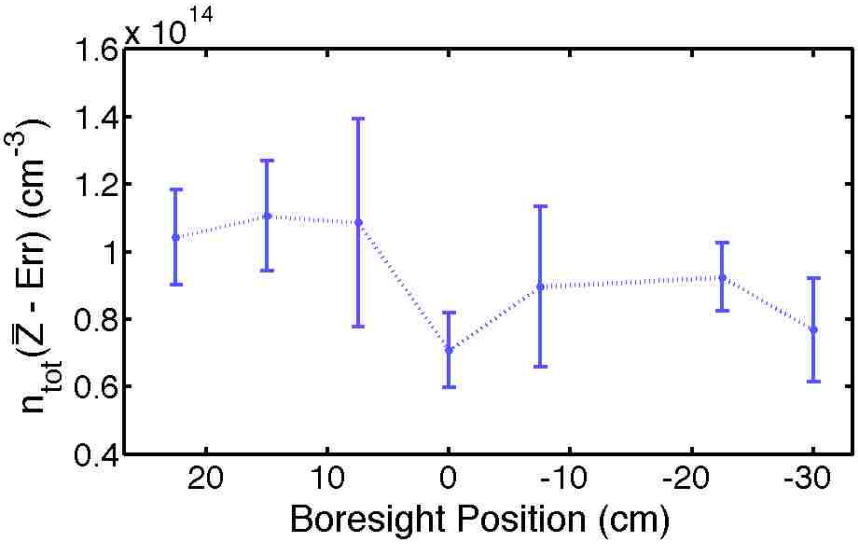

Figure 4.6: Spatial profile of chord-integrated density $n_{tot} \approx n_e/\bar{Z}$ at $t = 77$ μs, using a chord length of 30 cm estimated from camera images, along seven interferometer chords. Because the contribution from ions and neutrals is small, this plot represents the plasma electron density distribution multiplied by local mean charge state. Error-bars indicate the standard deviation over multiple shots.

4.2 Comparison with Theoretical and Computational Models of Rayleigh–Taylor Growth

When the Helmholtz coils are not energized, no instability is observable on the fast cameras, indicating that growth either does not occur, or occurs at wavelengths too small to be resolved. However, for the case presented here, the Helmholtz coils are initially energized with a 1.1 kA current, generating an $\approx$ 290-Gauss vacuum magnetic field. However, the magnetic field generated by the Helmholtz coil is initially oriented into-the-page, in a direction which would be inconsistent with the stabilization mechanism of the magnetic-Rayleigh–Taylor instability seen in Equation 1.3. The $\vec{k} \cdot \vec{B}$ term provides stabilization of short wavelength modes, but depends on

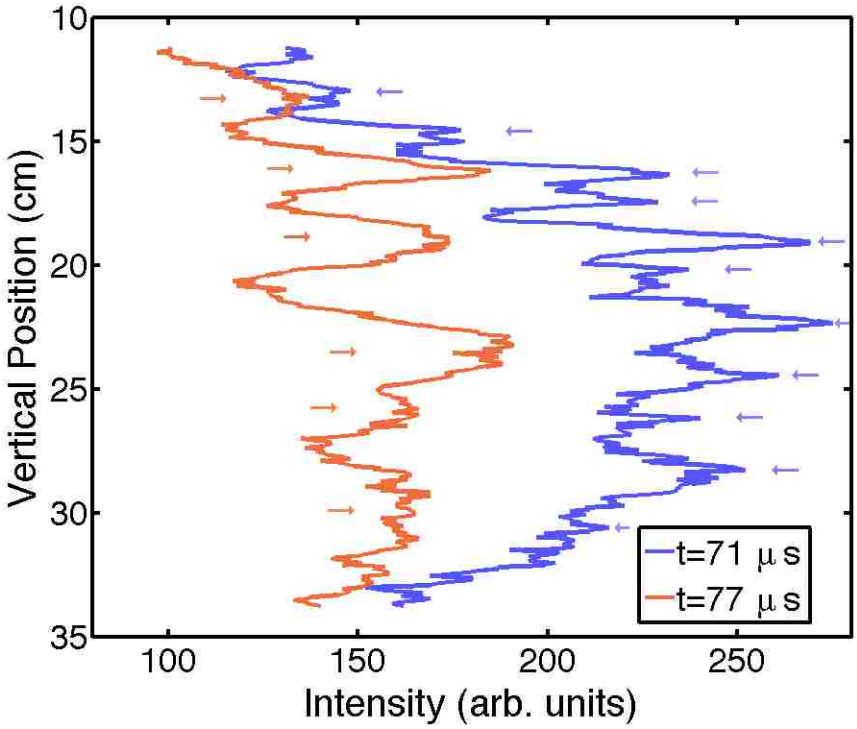

Figure 4.7: Summed emission lineouts from frames (c) and (f) of Figure 4.1. Pixel intensity of 10 adjacent (300-pixel high) columns are summed together across the regions of each frame containing the observed fingers. The locations of the bright fingers are highlighted with arrows. The wavelength of the observed modes decreases by a factor of 5/3 over the course of 6 μs.

a component of the magnetic field which would be vertical in the images of Figure 4.1, and be perpendicular to the applied vacuum magnetic field. Calculating linear growth rate versus mode wavelength (using Equation 1.3) for a variety of magnetic field values relevant to the experimental parameter space results in the curves shown in Figure 4.8. The observed modes have wavelengths of ≈ 2 cm, a wavelength which corresponds to the peak growth rate for a magnetic field component of about 15 Gauss aligned with the instability wave vector and growth on ~ 10 μs timescales. As seen in Figure 4.2, the azimuthal probe, which captures vertical field activity

(that is, aligned with $\vec{k}$) at a single location in the interaction region, shows activity of sufficient magnitude to account for magnetic stabilization for a period between 68 and 75 μs during the interaction. This 7 μs period corresponds to about 3/4 of a growth time. Due to the dynamic pressure ($q = \rho v^2/2$, where ρ and v are jet mass density and velocity, respectively) of our plasma jets being ≈ 30 times greater than the magnetic pressure, it is plausible that the applied vacuum field can be partially reoriented into the needed vertical (azimuthal) component through advection at other locations in the vicinity of the interface.

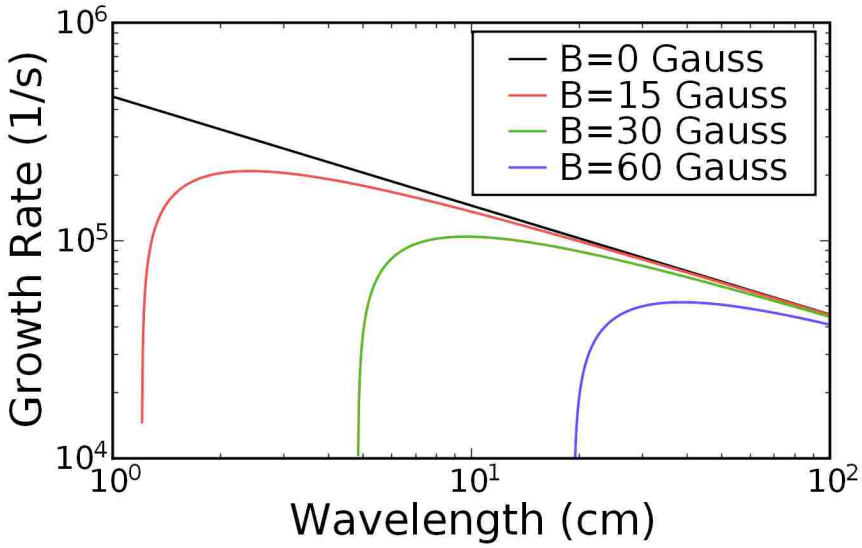

Figure 4.8: Linear growth rate of magnetic-Rayleigh–Taylor instability for the observed parameter space.

Viscous stabilizing mechanisms could also contribute to the suppression of short-wavelength mode growth, as seen in Equation 1.4. For the experimental regime here there is weak electron magnetization in the arriving jet since electron gyroradius $r_{Le} \approx 0.27$ cm and Hall parameter $\omega_{ce}\tau_e \approx 0.3$ (where ω_{ce} is electron cyclotron frequency in rad/s and τ_e is electron-electron collision time). This means that gyroviscosity is not significant because $\omega_{ce}\tau_e$ is less than one and the large ion mass

m_i ($m_i/m_p \approx 33.5$, where m_p is the mass of a proton) indicates that ion viscosity dominates plasma viscosity. For this case dynamic viscosity ($\mu = \rho\nu$) is given in cgs units by [53, 54]

$$\mu_0^i = 0.96 n k T_i \tau_i, \tag{4.1}$$

where

$$\tau_i = \frac{3\sqrt{m_i}\,(kT_i)^{3/2}}{4\sqrt{\pi} n \ln\Lambda e^4 \bar{Z}^4}, \tag{4.2}$$

where $\ln\Lambda$ is the Coulomb logarithm, k is Boltzmann's constant, T_i is ion temperature, n is plasma number density, and τ_i is ion-ion collision time. Thus $\lambda_{\max} \sim T_i^{5/3}\bar{Z}^{-8/3}$. The energy equilibration time of the second jet upon arrival at the interaction region is ≈ 30 μs, after expanding during flight from the railgun nozzle to the interaction region. On exit from the gun nozzle ≈ 30 μs earlier, the highly collisional jet was $\approx 100\times$ as dense and at nearly the same temperature [43], thus having a sub-microsecond energy equilibration time. Since $T_e = T_i$ at the nozzle, and the equilibration time is still on the order of the plasma lifetime after expansion, the assumption that $T_e = T_i$ is quite reasonable at the time of interaction.

As mentioned previously, temperatures in the vicinity of the accelerating interface are in the range $2.3 < T_e < 2.8$ eV, and corresponding ionization states are in the range $1.2 < \bar{Z} < 1.6$. This means that dynamic viscosities in the range $5.2 \times 10^{-5} < \mu < 1.1 \times 10^{-4}$ g/(cm $\cdot$ s) are possible, which for acceleration $g = 10^9$ m/s^2 and density $\rho_2 = 2\rho_1 = 1.12\times10^{-8}$ g/cm^3 can stabilize modes with maximum wavelengths in the range $\lambda_{\max} \approx 1.7$–$2.9$ cm. These wavelengths are consistent with the size of the observed growing wavelengths.

To explore the effects of viscous and magnetic stabilization in the experimental

regime, two-dimensional simulations of magnetic-Rayleigh–Taylor-instability growth were computed using the code WARPX [55, 56, 57]. In these simulations, a magnetohydrodyanmic model with viscosity was solved with a 2^{nd} order discontinuous Galerkin method. The equation system neglects electron physics (velocity $\vec{v} = \vec{v}_i$) and resistivity in Ohm's law ($\vec{E} = -\vec{v} \times \vec{B}$), such that continuity, momentum, energy, and Faraday's law appear as [58]

$$\frac{\partial \rho}{\partial t} + \nabla \cdot (\rho \vec{v}) = 0 \tag{4.3}$$

$$\frac{\partial \rho \vec{v}}{\partial t} + \nabla \cdot \left(\rho \vec{v}\vec{v} + p\overline{I} - \frac{\vec{B}\vec{B}}{\mu_0} + \frac{B^2}{2\mu_0}\overline{I} + \overleftrightarrow{\Pi_i} \right) = -\rho \vec{g} \tag{4.4}$$

$$\frac{\partial \epsilon}{\partial t} + \nabla \cdot \left((\epsilon + p + \frac{B^2}{2\mu_0})\vec{v} - \frac{\vec{B} \cdot \vec{v}}{\mu_0}\vec{B} + \overleftrightarrow{\Pi_i} \cdot \vec{v} \right) = -\rho \vec{g} \cdot \vec{v} \tag{4.5}$$

$$\frac{\partial \vec{B}}{\partial t} - \nabla \times \left(\vec{v} \times \vec{B} \right) = 0, \tag{4.6}$$

where total energy $\epsilon = \epsilon_i + \epsilon_e$, pressure $p = p_i + p_e$, μ_0 is the permeability of free space, $\overline{I}$ is the identity matrix, and $\overleftrightarrow{\Pi_i}$ is the viscosity tensor. Due to the presence of ion viscosity, the momentum equation includes the divergence of viscosity tensor $\nabla \cdot \overleftrightarrow{\Pi_i}$ and the energy equation includes a viscous heating term $\nabla \cdot \overleftrightarrow{\Pi_i} \cdot \vec{v}$, on the left-hand-side of the equations. The body forces due to gravity appear on the right-hand-side of the momentum and energy equations. The form of viscosity tensor is given by [54]

$$\overleftrightarrow{\Pi_i} = -\mu_0^i \overleftrightarrow{W_i}, \tag{4.7}$$

where

$$\overleftrightarrow{W_i} = \nabla \vec{v} + (\nabla \vec{v})^T - \frac{2}{3}\delta_{ij} \nabla \cdot \vec{v}. \tag{4.8}$$

These simulations were initialized with a uniform acceleration oriented adversely to a smooth density gradient between a light and heavy fluid given by

$$n = \frac{n_0}{2}\frac{2A}{1-A}\tanh\left(\frac{\alpha y}{L_y}\right) + \frac{n_0}{2}\frac{2A}{1-A} + n_0, \tag{4.9}$$

where n_0 is number density of the lighter fluid, A is the Atwood number, α is the length scale over which the gradient occurs, and L_y is the height of the computational domain. In order to ensure that the un-perturbed profile is in equilibrium, the pressure profile was initialized to

$$P = P_{\min} - \frac{gm_i}{2}\left[\left(\frac{n_0}{2}\frac{2A}{1-A}\right)\frac{L_y}{\alpha}\ln\cosh\left(\frac{\alpha y}{L_y}\right) + \left(\frac{n_0}{2}\frac{2A}{1-A} + n_0\right)y\right] + \left(\frac{n_0}{2}\frac{2A}{1-A} + n_0\right)k_B T_0, \tag{4.10}$$

where $P_{\min}$ is a constant chosen to prevent the initial condition from having zero or negative pressure, k_B is the Boltzmann constant, and T_0 is the temperature, which for the purposes of these simulations is arbitrary. The horizontal density profiles are uniform except for cosine-form density perturbations at the fluid interface described by

$$\delta n = \alpha n_0\left[\cos\left(1\cdot 2\pi\frac{x}{L_x}\right) + \cos\left(5\cdot 2\pi\frac{x}{L_x}\right) + \cos\left(20\cdot 2\pi\frac{x}{L_x}\right)\right]\exp\left(\frac{-y^2}{2y_r^2}\right), \tag{4.11}$$

where y_r is the vertical region of the fluid interface where the perturbation is applied smoothly and L_x is the horizontal domain size. The coefficients 1, 5, and 20 in the cosine terms seed the perturbation with wavelengths corresponding to 20 cm, 4 cm, and 1 cm across the domain. The simulations are performed on a Cartesian grid with

200×300 cells with 1 mm resolution to capture the smallest scales we can observe experimentally. The horizontal domain size L_x is 20 cm and the vertical domain size L_y is 30 cm. Periodic boundary conditions are employed in the horizontal direction and the top and bottom boundaries are conducting walls. Additionally the Atwood number is 1/3 (which corresponds to a factor of 2 in density), the acceleration g is 10^9 m/s^2, ion mass $m_i = 33.5 m_p$ (estimated via chamber pressure rise, as described in Section 2.2), and mass density $\rho_2 = 2\rho_1 \approx 1.12 \times 10^{-8}$ g/cm^3 (where $\rho_1 = m_i n_0$). The initial condition is shown in Figure 4.9.

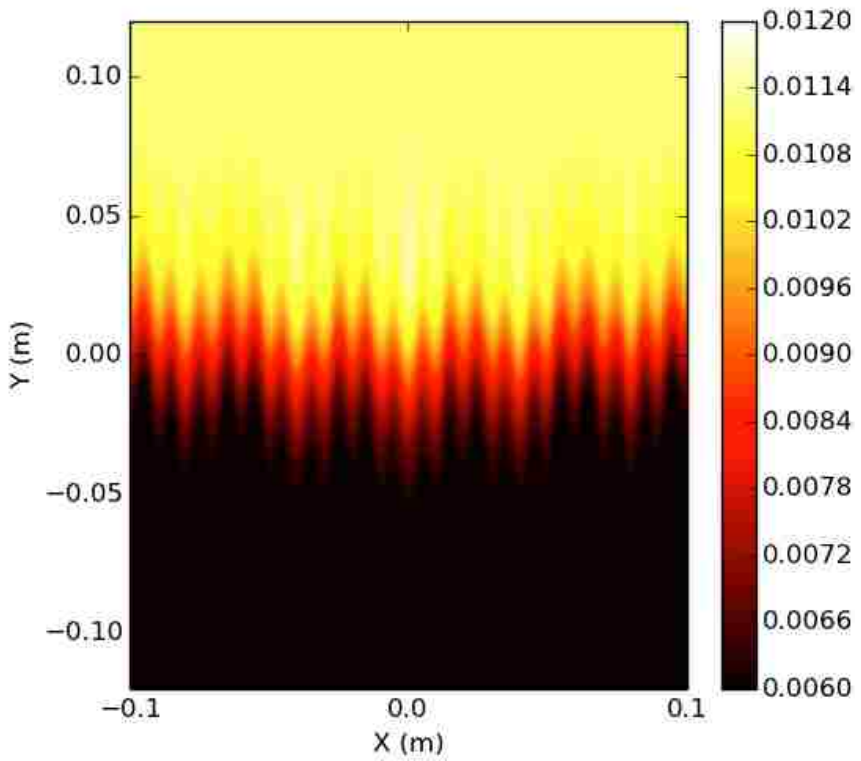

Figure 4.9: Detailed view of simulation initial condition, showing perturbed interface between heavy and light fluids. Force from acceleration is directed downward.

The domain was initialized with an array of different uniform horizontal magnetic fields and viscosities to isolate the effects of each on Rayleigh–Taylor-instability

growth. Field values of 0, 2, and 15 Gauss were run as well as the dynamic viscosities computed above. Simulations were run on a MacBook Pro computer equipped with a quad-core, hyperthreading (8 virtual cores), 2.66 GHz Intel i7 processor. Inviscid cases ran for ≈ 13 minutes per output (10 μs of simulation) and cases with viscosity ran for ≈ 40 minutes per output. Figure 4.10 compares the results after 10, 20, and 30 μs of growth for six cases, including one with both magnetic field and viscosity.

The top most-panel in each column in Figure 4.10 shows simulation results with no physical viscosity or magnetic field. For this case, short-wavelength modes grow rapidly and saturate. The second and third cases from the top also have zero physical viscosity, and show that a horizontal magnetic field of 2 G is incapable of stabilizing even 1-cm modes, while a field of 15 G is capable of stabilizing 1-cm but not 4-cm modes. The fourth and fifth simulations from the top have no magnetic field but have viscosities corresponding to $T_e = 2.8$ eV, $\bar{Z} = 1.6$ and $T_e = 2.3$ eV, $\bar{Z} = 1.2$, respectively, from top to bottom. Interestingly, while both cases are capable of stabilizing 1-cm modes, the 2.8-eV case does so poorly, while the 2.3-eV case is qualitatively similar to the 15-G magnetic-field-only case. Finally the bottom-most case shows a simulation with both high viscosity and a 15-G magnetic field, and the results are quite similar to the 15-G field-only case. These simulations suggest that our experiments are in a regime in which both magnetic and viscous stabilization are capable of stabilizing short-wavelength Rayleigh–Taylor-instability growth.

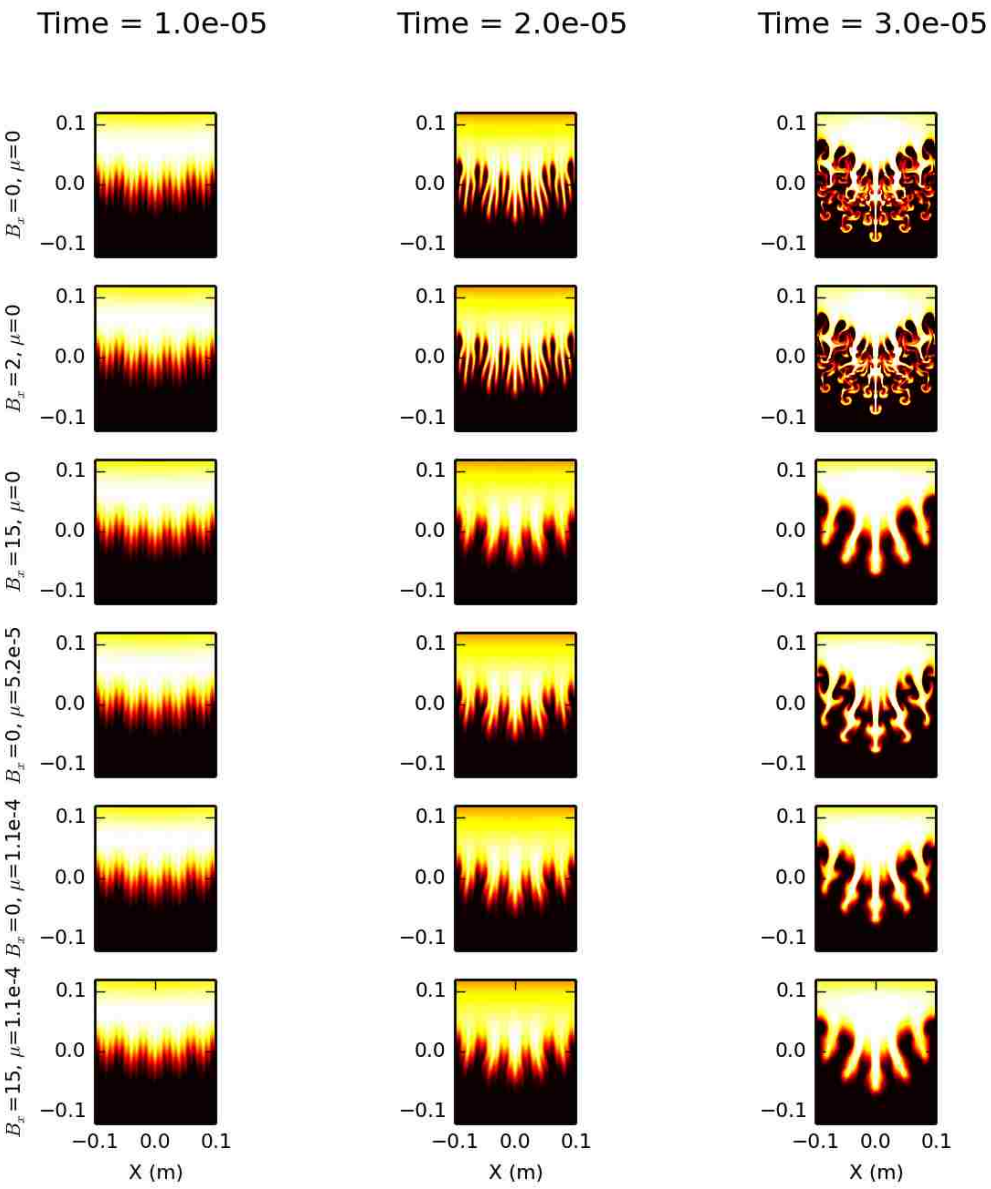

Figure 4.10: Ideal 2D MHD simulation of RTI evolution at a plasma interface. Case with no magnetic field does not show stabilization of any modes (top) after 30 μs of growth, while cases with magnetic field of sufficient magnitude (middle-top) or ion viscosity (middle-bottom) show stabilization of short-wavelength RT modes. A case with viscosity and magnetic field (bottom) shows similar growth characteristics as solely magnetic stabilization. Units are Gaussian except for domain size in meters.

Chapter 5

Conclusions and Future Work

To summarize, observations of Rayleigh-Taylor-instability growth at the interface between magnetized, stagnated plasma and a decelerating, unmagnetized plasma jet have been observed and characterized. The observed instability wavelength (≈ 2 cm) and growth time (~ 10 μs) are consistent with the fastest-growing wavelength predicted by linear magnetic-RTI theory in the presence of a 15-G field aligned with the instability wave vector. A field with this magnitude and direction was measured in our experiment for an ≈ 7 μs time period during instability growth. Furthermore, spectroscopic analysis suggests that plasma temperatures and ionization states are capable of supporting a plasma viscosity which could contribute to stabilization. The captured images of instability growth show a progression toward longer wavelengths by a factor of 5/3 over 6 μs, consistent with the presence of stabilizing mechanisms. Finally, a computational study of instability growth in the presence of these stabilizing mechanisms was conducted with a magnetohydrodynamic model in the WARPX code. These investigations of the damping effect of magnetic field and viscosity on the instability led to the conclusion that both could be contributing to the observation of mode evolution toward longer wavelength.

5.1 Improvement of Cosmic Shock Experiments

Study of cosmic shocks was the original motivation for the experimental campaign described in this dissertation, and the effort continued throughout investigation of the Rayleigh–Taylor instability. However the results, based on analysis so far, have been inconclusive. A particularly significant difficulty is the lack of magnetization of the incoming jets. Rather than dynamics between two magnetized collisionless flows, experiments appear to be dominated by dynamics between unmagnetized jets and a vacuum magnetic field. This issue could possibly be addressed by larger magnetic field coils to magnetize the jets while still in flight to the interaction region, or possibly by exploring the use of more resistive jets. Another problem was the presence of impurities in the jets which enabled the mean ionization state to increase and cause a transition from a collisionless to collisional regime. To tackle the impurity problem, improved plasma gun designs should be investigated, either with contoured rail cross sections to prevent high current near the insulator, or perhaps a coaxial gun.

5.2 Suggestions for Interferometer Diagnostic

Several further improvements could make the interferometer an even more effective diagnostic at the Plasma Liner Experiment. First, the installation of the Helmholtz coils in the vacuum chamber interfered with the beam path for chord 3 of the interferometer. It is recommended that positioning of the chords be adjusted so that chord three has a clear path between the launch and receive stage. Second, the author recommends finding a replacement for the Thorlabs PAF-X-18-PC-A fiber couplers at the vacuum-chamber mounted receive stage. While these couplers have several advantages as discussed in [48], including compact size and good stability (even when removing and attaching fibers), the author found them to lack mechan-

ical robustness. The extremely small set screws used to adjust the alignment of the couplers were easily and frequently stripped, and the adjustment mechanism itself began to show signs of malfunction in multiple couplers (with varying degrees of severity) by the completion of the research presented in this dissertation. Also, not insignificant was the amount of time necessary to adjust the couplers when compared to the couplers employed in the beam path of the reference beam.

Finally, the AD8130 amplifiers were found to suffer from offset drift over time. Even after calibration, within a few weeks the zero offsets were found to be as much as several hundred millivolts. From an operational standpoint, keeping the amplifiers calibrated was infeasible, and the previously-described changes to the analysis routines were employed to correct for this issue. The cost, however is that data analysis takes approximately twice as much time with the amplifiers than for data collected without amplifiers. Also, the data analysis routines rely on analyzing a significant number of shots with the same settings to compute accurate phase shifts. If budget and time allow, the author recommends researching methods of preventing offset in the amplifier circuit, or replacing the amplifiers with another model less prone to drift.

5.3 Suggestions for Schlieren Diagnostic

For future work on the schlieren diagnostic, the author recommends adding a spatial filter to the beam path of the infrared laser to improve the uniformity of the beam illumination. This was considered but due to budget constraints and limited usefulness of the diagnostic for the experiments conducted, was not implemented. Another highly recommended improvement would be to develop a method of visualizing the location of the infrared beam, even at its expanded, low intensity. This would aid in tracking down reflections, checking alignment with the visible beam, and speeding

up determination of the exact location of the focal point of the second parabolic mirror.

Finally, an issue that was avoided in the initial trials of the diagnostic is the benefit of using an extended light source and consequently having a finite depth of field in the system. This issue is discussed in detail in Settles [50]. In terms of applicability to the existing system, the presence of the diverging lens in the schlieren launch stage makes the laser light a point source for the parabolic mirrors, and in the absence of optical aberrations, the probe beam is perfectly collimated and will focus to a point at the focal point of the second mirror. While this has advantages in terms of aligning the system and for initial trials, it has the disadvantages that all phenomena along the probe beam are equally in focus (making it difficult to distinguish experimental from ambient phenomena) and that at the knife edge the entire image is at a single point, making attempts to block only a part of the beam either impossible or doing so makes the scene unevenly cut off. A variety of diffusers and an adjustable slit were purchased in order to create an extended light source at the exit of the laser enclosure, but attempts to do this were not completed due to challenges in obtaining sufficient brightness to complete alignment. The author believes that tackling this challenge would me most fruitful in improving the diagnostic, as meeting this challenge successfully would likely solve other problems such as unevenness of illumination and the presence of diffraction patterns.

5.4 Future Research Directions

In addition to the growth of Rayleigh–Taylor instabilities, other phenomena were observed during the experiments discussed including the presence of striations, jet stopping, and the appearance of large-scale structure uniquely present when jets interact with the magnetic field. For example, the image shown in Figure 5.1 shows

striations that appear when argon jets encounter a magnetic field with magnitude ≈ 440 G. This observation is reminiscent of observations in barium plasmas reported in [31]. Examples of jet stopping can be seen in the image sequences in Figures 5.2 and 5.3. These sequences are captured during shots in which hydrogen gas was injected into the railguns instead of argon. The Helmholtz coils were energized with the same initial field (≈ 300 G) as in the shot shown in Figure 4.1. The frames are taken at the same late times as those previously shown as well, capturing the arrival of a secondary jet. Instead of the instability growth observed previously, what appear to be jet stopping and the counter-propagation of a bow-shock like structure are observed (presumably from the opposing jet). The physics of these phenomena are open research questions at the time of this writing. Additionally, the experimental apparatus employed to conduct the research in this dissertation is capable of accessing physics regimes relevant to the results reported in [30]. As discussed in Subsection 1.2.1, the behavior of plasma jets changed dramatically when encountering a magnetic field above a critical value B_{critical}. The author estimates for the argon jets reported on in this dissertation, the critical magnetic field magnitude is $B_{\text{critical}} \approx 780$ G.

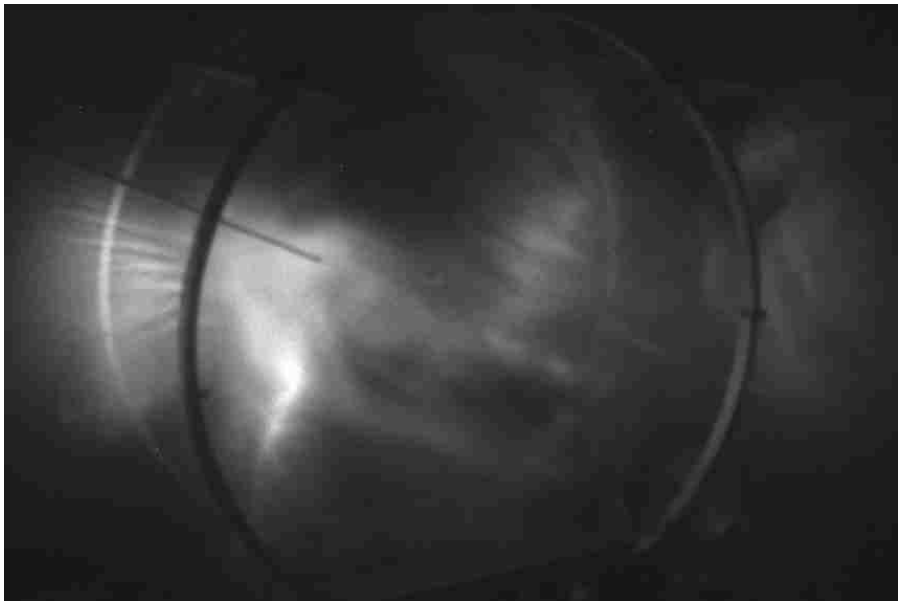

Figure 5.1: Striations appear (left side of image) when argon jet encounters ≈ 440 G magnetic field. Photograph captured by Dicam Pro camera on shot 2959.

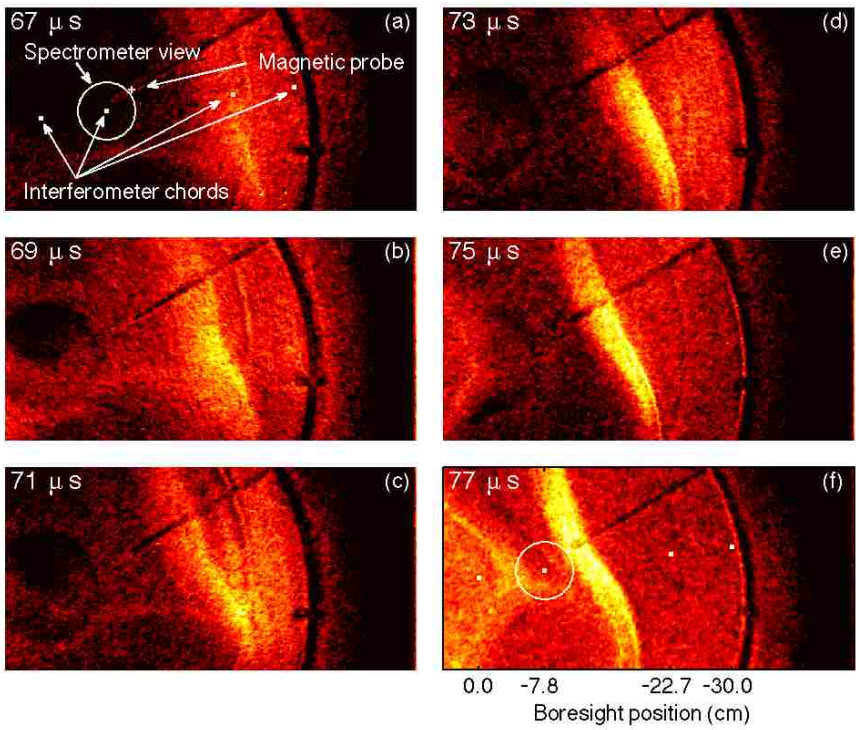

Figure 5.2: Late-time arrival of second hydrogen jet at interaction region in shot 3457. The right-hand jet appears to stop near magnetic probe tip as a shock-like structure forms. In the final two frames, a bow-shock like structure arrives from the left.

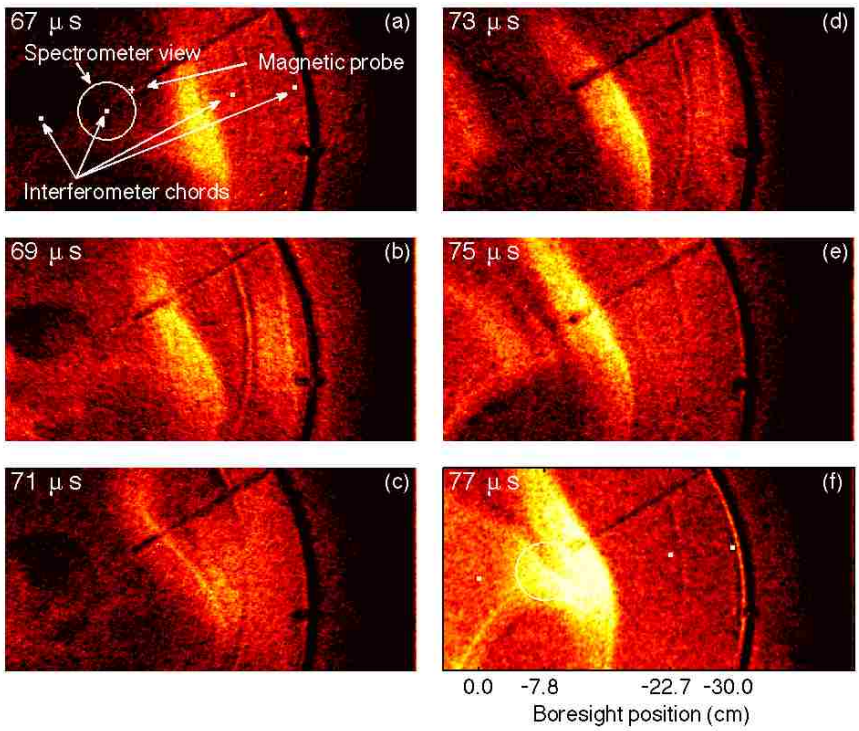

Figure 5.3: Late-time arrival of second hydrogen jet at interaction region in shot 3458. The right-hand jet appears to stop near magnetic probe tip as a shock-like structure forms. In the final three frames, a bow-shock like structure arrives from the left.

Appendix A

Interferometer analysis codes

The MATLAB function 'chord_data' contained in 'chord_data.m' returns the raw I signal, Q signal, and time domain given a shot number and a chord number. This function is designed to have pre-defined digitizer configurations built in for most shot numbers. If there is not a pre-defined digitizer configuration, the code reverts to a default configuration. This function is shown below.

```
function [I,Q,t] = chord_data(shot_number, chord_number)

mdsconnect('localhost');
mdsopen('plx',shot_number);

p0 = 'devices:screen_box:camac_1:jrg_tr_';
t0 = 'dim_of(devices:screen_box:camac_1:jrg_tr_';
p2 = ':input_';

if shot_number < 79
    di = [1 0; ...    % CHORD 1 I
          1 1; ...    % CHORD 1 Q
          1 2; ...    % CHORD 2 I
          1 3; ...    % CHORD 2 Q
          1 4; ...    % CHORD 3 I
          1 5; ...    % CHORD 3 Q
          1 6; ...    % CHORD 4 I
          1 7; ...    % CHORD 4 Q
          1 8; ...    % CHORD 5 I
          1 9; ...    % CHORD 5 Q
          1 10; ...   % CHORD 6 I
          1 11; ...   % CHORD 6 Q
          1 12; ...   % CHORD 7 I
          1 13; ...   % CHORD 7 Q
          1 14; ...   % CHORD 8 I
          1 15];      % CHORD 8 Q
```

```
elseif (shot_number >= 79) && (shot_number < 670)
    di = [1 0; ...    % CHORD 1 I
          1 1; ...    % CHORD 1 Q
          1 2; ...    % CHORD 2 I
          1 3; ...    % CHORD 2 Q
          1 4; ...    % CHORD 3 I
          1 5; ...    % CHORD 3 Q
          2 6; ...    % CHORD 4 I
          2 7; ...    % CHORD 4 Q
          2 8; ...    % CHORD 5 I
          2 9; ...    % CHORD 5 Q
          1 10; ...   % CHORD 6 I
          1 11; ...   % CHORD 6 Q
          1 12; ...   % CHORD 7 I
          1 13; ...   % CHORD 7 Q
          1 14; ...   % CHORD 8 I
          1 15];      % CHORD 8 Q
elseif (shot_number >= 670) && (shot_number < 2505)
    di = [1 0; ...    % CHORD 1 I
          1 1; ...    % CHORD 1 Q
          1 2; ...    % CHORD 2 I
          1 3; ...    % CHORD 2 Q
          1 4; ...    % CHORD 3 I
          1 5; ...    % CHORD 3 Q
          2 0; ...    % CHORD 4 I
          2 1; ...    % CHORD 4 Q
          2 8; ...    % CHORD 5 I
          2 9; ...    % CHORD 5 Q
          1 10; ...   % CHORD 6 I
          1 11; ...   % CHORD 6 Q
          1 12; ...   % CHORD 7 I
          1 13; ...   % CHORD 7 Q
          1 14; ...   % CHORD 8 I
          1 15];      % CHORD 8 Q
elseif (shot_number >= 2505) && (shot_number < 2552)
    di = [1 0; ...    % CHORD 1 I
          1 1; ...    % CHORD 1 Q
          1 2; ...    % CHORD 2 I
          1 3; ...    % CHORD 2 Q
          1 4; ...    % CHORD 3 I
          1 5; ...    % CHORD 3 Q
          1 6; ...    % CHORD 4 I
          1 7; ...    % CHORD 4 Q
          1 8; ...    % CHORD 5 I
          1 9; ...    % CHORD 5 Q
          1 10; ...   % CHORD 6 I
          1 11; ...   % CHORD 6 Q
          1 12; ...   % CHORD 7 I
          1 13; ...   % CHORD 7 Q
          1 14; ...   % CHORD 8 I
          1 15];      % CHORD 8 Q
elseif (shot_number >= 2578) && (shot_number < 2587)
    di = [nan nan; ...    % CHORD 1 I
          nan nan; ...    % CHORD 1 Q
          1 2; ...        % CHORD 2 I
          1 3; ...        % CHORD 2 Q
          1 4; ...        % CHORD 3 I
          1 5; ...        % CHORD 3 Q
          2 0; ...        % CHORD 4 I
          2 1; ...        % CHORD 4 Q
          2 8; ...        % CHORD 5 I
          2 9; ...        % CHORD 5 Q
```

```
           1 10; ...       % CHORD 6 I
           1 11; ...       % CHORD 6 Q
           1 12; ...       % CHORD 7 I
           1 13; ...       % CHORD 7 Q
           1 0; ...        % CHORD 8 I
           1 1];           % CHORD 8 Q
elseif (shot_number >= 2591) && (shot_number < 2653)
    di = [nan nan; ...     % CHORD 1 I
          nan nan; ...     % CHORD 1 Q
          nan nan; ...     % CHORD 2 I
          nan nan; ...     % CHORD 2 Q
          1 4; ...         % CHORD 3 I
          1 5; ...         % CHORD 3 Q
          2 0; ...         % CHORD 4 I
          2 1; ...         % CHORD 4 Q
          2 8; ...         % CHORD 5 I
          2 9; ...         % CHORD 5 Q
          1 10; ...        % CHORD 6 I
          1 11; ...        % CHORD 6 Q
          1 12; ...        % CHORD 7 I
          1 13; ...        % CHORD 7 Q
          1 0; ...         % CHORD 8 I
          1 1];            % CHORD 8 Q
else
    % DEFAULT CONFIGURATION
    di = [1 0; ...     % CHORD 1 I
          1 1; ...     % CHORD 1 Q
          1 2; ...     % CHORD 2 I
          1 3; ...     % CHORD 2 Q
          1 4; ...     % CHORD 3 I
          1 5; ...     % CHORD 3 Q
          2 0; ...     % CHORD 4 I
          2 1; ...     % CHORD 4 Q
          2 8; ...     % CHORD 5 I
          2 9; ...     % CHORD 5 Q
          1 10; ...    % CHORD 6 I
          1 11; ...    % CHORD 6 Q
          1 12; ...    % CHORD 7 I
          1 13; ...    % CHORD 7 Q
          1 14; ...    % CHORD 8 I
          1 15];       % CHORD 8 Q
end

if chord_number == 1
    I = mdsvalue([p0 num2str(di(1,1)) p2 num2str(di(1,2),'%02.0f')]);
    Q = mdsvalue([p0 num2str(di(2,1)) p2 num2str(di(2,2),'%02.0f')]);
    t = mdsvalue([t0 num2str(di(1,1)) p2 num2str(di(1,2),'%02.0f') ')']);
elseif chord_number == 2
    I = mdsvalue([p0 num2str(di(3,1)) p2 num2str(di(3,2),'%02.0f')]);
    Q = mdsvalue([p0 num2str(di(4,1)) p2 num2str(di(4,2),'%02.0f')]);
    t = mdsvalue([t0 num2str(di(3,1)) p2 num2str(di(3,2),'%02.0f') ')']);
elseif chord_number == 3
    I = mdsvalue([p0 num2str(di(5,1)) p2 num2str(di(5,2),'%02.0f')]);
    Q = mdsvalue([p0 num2str(di(6,1)) p2 num2str(di(6,2),'%02.0f')]);
    t = mdsvalue([t0 num2str(di(5,1)) p2 num2str(di(5,2),'%02.0f') ')']);
elseif chord_number == 4
    I = mdsvalue([p0 num2str(di(7,1)) p2 num2str(di(7,2),'%02.0f')]);
    Q = mdsvalue([p0 num2str(di(8,1)) p2 num2str(di(8,2),'%02.0f')]);
    t = mdsvalue([t0 num2str(di(7,1)) p2 num2str(di(7,2),'%02.0f') ')']);
elseif chord_number == 5
    I = mdsvalue([p0 num2str(di(9,1)) p2 num2str(di(9,2),'%02.0f')]);
    Q = mdsvalue([p0 num2str(di(10,1)) p2 num2str(di(10,2),'%02.0f')]);
```

```
151     t = mdsvalue([t0 num2str(di(9,1)) p2 num2str(di(9,2),'%02.0f') ')']);
152 elseif chord_number == 6
153     I = mdsvalue([p0 num2str(di(11,1)) p2 num2str(di(11,2),'%02.0f')]);
154     Q = mdsvalue([p0 num2str(di(12,1)) p2 num2str(di(12,2),'%02.0f')]);
155     t = mdsvalue([t0 num2str(di(11,1)) p2 num2str(di(11,2),'%02.0f') ')']);
156 elseif chord_number == 7
157     I = mdsvalue([p0 num2str(di(13,1)) p2 num2str(di(13,2),'%02.0f')]);
158     Q = mdsvalue([p0 num2str(di(14,1)) p2 num2str(di(14,2),'%02.0f')]);
159     t = mdsvalue([t0 num2str(di(13,1)) p2 num2str(di(13,2),'%02.0f') ')']);
160 elseif chord_number == 8
161     I = mdsvalue([p0 num2str(di(15,1)) p2 num2str(di(15,2),'%02.0f')]);
162     Q = mdsvalue([p0 num2str(di(16,1)) p2 num2str(di(16,2),'%02.0f')]);
163     t = mdsvalue([t0 num2str(di(15,1)) p2 num2str(di(15,2),'%02.0f') ')']);
164 else
165     I = [0];
166     Q = [0];
167     t = [0];
168 end
169
170 mdsclose;
171 mdsdisconnect;
```

The MATLAB function 'find_IQ_envelopes' contained in 'find_IQ_envelopes.m' returns minimum and maximum values of the I and Q signals for given a range of shots and chord numbers. When analyzing interferometer data from a given shot, a group of other shots from the same day should be passed to 'find_IQ_envelopes' so that the function 'calculate_phase_shift_amplified' can correct for offsets. This function is shown below.

```
1  function IQ_min_max = find_IQ_envelopes(shot_group, chords)
2
3  % Determines the envelope of I and Q values for each chord of interest
4  % in the shot group of interest (usually from the same shot day)
5  %
6  % IQ_min_max = calculate_phase_shift(shot_group, chords)
7  %
8  % Arguments: shot_group is an array of shot numbers for which the envelope
9  %            of possible I and Q values is computed
10 %
11 %            chords is an array of chord numbers for which the envelope
12 %            of possible I and Q values is computed
13
14 IQ_min_max = zeros(length(chords), 4);
15
16 disp(['Pre-analyzing ' num2str(shot_group(1))])
17
18 for j = 1:1:length(chords)
19
20     [I,Q,t] = chord_data(shot_group(1), chords(j));
21     I_smoothed = fastsmooth(I,5,1,1);
22     Q_smoothed = fastsmooth(Q,5,1,1);
23
24     IQ_min_max(j,1) = min(I_smoothed);
```

```
25      IQ_min_max(j,2) = max(I_smoothed);
26      IQ_min_max(j,3) = min(Q_smoothed);
27      IQ_min_max(j,4) = max(Q_smoothed);
28  end
29
30  clear I Q t I_smoothed Q_smoothed
31
32  for i = 2:1:length(shot_group)
33
34      disp(['Pre-analyzing ' num2str(shot_group(i))])
35
36      for j = 1:1:length(chords)
37
38          [I,Q,t] = chord_data(shot_group(i), chords(j));
39          I_smoothed = fastsmooth(I,5,1,1);
40          Q_smoothed = fastsmooth(Q,5,1,1);
41
42          IQ_min_max(j,1) = min([I_smoothed IQ_min_max(j,1)]);
43          IQ_min_max(j,2) = max([I_smoothed IQ_min_max(j,2)]);
44          IQ_min_max(j,3) = min([Q_smoothed IQ_min_max(j,3)]);
45          IQ_min_max(j,4) = max([Q_smoothed IQ_min_max(j,4)]);
46      end
47
48      clear I Q t I_smoothed Q_smoothed
49  end
50
51  if sum(sum((abs(IQ_min_max) > 1.9))) > 1.0
52      disp('WARNING: Problem detected with shot(s) in group, IQ_min_max values invalid
            .')
53  end
```

The MATLAB function 'calculate_phase_shift_amplified' contained in 'calculate_phase_shift_amplified.m' returns the plasma component of phase shift and time domain given a minimum of a shot number. For more accurate results, the user is encouraged to also provide the desired chord numbers, the start time and end time of the presence of plasma, and the output matrix from 'find_IQ_envelopes'. The use of smoothing at various stages in the analysis are also built-in options. This function is shown below.

```
1   function [time_save phase_save] = ...
2           calculate_phase_shift_amplified(shot, chords, t_start, t_end, ...
3       offset_compensation, IQ_min_max, IQ_smoothing, phase_smoothing)
4
5   % Calculates the phase shift measured by the interferometer
6   % [time phase] = calculate_phase_shift(shot)
7   % [time phase] = calculate_phase_shift(shot, chords)
8   % [time phase] = calculate_phase_shift(shot, chords, t_start, t_end)
9   % [time phase] = calculate_phase_shift(shot, chords, t_start, t_end,
10  %                   offset_compensation, IQ_min_max)
11  % [time phase] = calculate_phase_shift(shot, chords, t_start, t_end,
12  %                   offset_compensation, IQ_min_max, IQ_smoothing,
13  %                   phase_smoothing)
```

```
14 %
15 % Optional arguments: chords is an array of chord numbers for which phase
16 %                       information will be returned
17 %                       default value of chords is [4]
18 %
19 %                       t_start and t_end are times (in microseconds)
20 %                       bounding the phenomena of interest
21 %                       default values t_start = -20
22 %                                      t_end = 350
23 %
24 %                       offset_compensation is a boolean which indicates
25 %                       whether to compensate for offset variation in the
26 %                       raw I and Q signals, default value of true
27 %
28 %                       IQ_min_max is an array containing the maximum and
29 %                       minimum values of I and Q for the shot range of
30 %                       interest, as generated by 'find_IQ_envelopes'
31 %
32 %                       IQ_smoothing is a boolean which indicates whether to
33 %                       peform smoothing of the raw I and Q signals, default
34 %                       value of false
35 %
36 %                       phase_smoothing is a boolean which indicates whether
37 %                       to peform smoothing of the final calculated phase,
38 %                       default value of false
39
40 if isempty(shot)
41     shot = 2407;
42 end
43
44 if isempty(chords)
45     chords = [4];
46 end
47
48 if isempty(t_start)
49     t_start = -20;    % START OF TIME FRAME OF INTEREST (MICROSECONDS)
50 end
51
52 if isempty(t_end)
53     t_end = 300;      % END OF TIME FRAME OF INTEREST (MICROSECONDS)
54 end
55
56 if isempty(offset_compensation)
57     offset_compensation = true;  % BY DEFAULT PERFORM OFFSET SUBTRACTION
58 end
59
60 if isempty(IQ_smoothing)
61     IQ_smoothing = false;  % BY DEFAULT NO RAW IQ SMOOTHING
62 end
63
64 if isempty(phase_smoothing)
65     phase_smoothing = false;  % BY DEFAULT NO FINAL PHASE SMOOTHING
66 end
67
68 % PROCEED WITH ANALYSIS
69
70 t_save = 50;
71
72 Zeff = 1.0;  % ASSUMED VALUE OF IONIZATION FRACTION
73 dL = 1;      % ASSUMED CHORD LENGTH
74
75 c = 2.9979*10^8;              % SPEED OF LIGHT [m/s].
```

```
76  e = 1.6022*10^-19;              % CHARGE OF AN ELECTRON [C].
77  me = 9.1094*10^-31;             % MASS OF AN ELECTRON [kg].
78  mu0 = 4*pi*1*10^-7;             % PERMEABILITY OF FREE SPACE [H/m].
79  epsilon0 = 1/(mu0*c^2);         % PERMITTIVITY OF FREE SPACE [F/m].
80  lambda0 = 561.3*10^-9;          % OXXIUS LASER WAVELENGTH IN FREE SPACE [m].
81
82  for i = 1:1:length(chords)
83
84      chord = chords(i);
85
86      % RETRIEVE I AND Q SIGNALS FOR EACH CHORD
87
88      [I,Q,t] = chord_data(shot, chord);
89
90      time = t*10^6;
91
92  %     figure(shot*100+60+chord)
93  %     hold on
94  %     plot(t, I, 'c:', t, Q, 'g:')
95  %     title('Raw I and Q','FontSize',18)
96
97      if IQ_smoothing == true
98
99          % SMOOTH THE RAW I AND Q SIGNALS WITH FASTSMOOTH
100         % WIDTH 5, RECTANGULAR BOXCAR, ENDS HANDLED
101         I_smoothed = fastsmooth(I,5,1,1);
102         Q_smoothed = fastsmooth(Q,5,1,1);
103
104         % % SMOOTH I AND Q WITH MATLAB SMOOTH FUNCTION
105         % n_smooth = 5;
106         % I_smoothed = smooth(I,n_smooth,'moving');
107         % Q_smoothed = smooth(Q,n_smooth,'moving');
108
109         % plot(t, I_smoothed, 'b-', t, Q_smoothed, 'k-')
110
111     else
112
113         % BYPASS I AND Q SMOOTHING
114         I_smoothed = I;
115         Q_smoothed = Q;
116
117     end
118
119     clear I Q
120
121     % DETERMINE INDICES BOUNDING TIME FRAME OF INTEREST
122     dt = (max(time)-min(time))/(length(time)-1);
123     n_start = floor((t_start - min(time))/dt) + 2;
124     n_end = n_start + floor((t_end-t_start)/dt);
125     n_zero = n_start - floor(t_start/dt);
126     n_save = n_start + floor((t_save-t_start)/dt);
127
128     % AMPLIFIER OFFSET COMPENSATION
129
130     if offset_compensation == true
131
132         if isempty(IQ_min_max)
133             I_lower_bound = min(I_smoothed);
134             I_upper_bound = max(I_smoothed);
135             Q_lower_bound = min(Q_smoothed);
136             Q_upper_bound = max(Q_smoothed);
137         else
```

```
138             I_upper_bound = IQ_min_max(i,1);
139             I_lower_bound = IQ_min_max(i,2);
140             Q_upper_bound = IQ_min_max(i,3);
141             Q_lower_bound = IQ_min_max(i,4);
142         end
143
144         I_smoothed = I_smoothed - (I_upper_bound + I_lower_bound)/2;
145         Q_smoothed = Q_smoothed - (Q_upper_bound + Q_lower_bound)/2;
146
147         % plot(t, I_smoothed, 'b-', t, Q_smoothed, 'k-')
148
149         % hline(I_upper_bound, 'c:')
150         % hline(I_lower_bound, 'c:')
151         % hline(Q_upper_bound, 'g:')
152         % hline(Q_lower_bound, 'g:')
153     end
154
155     % CALCULATE PHASE SHIFT FROM AMPLITUDE-CORRECTED I & Q
156
157     I_amplitude = I_upper_bound - I_lower_bound;
158     Q_amplitude = Q_upper_bound - Q_lower_bound;
159
160     phase(:,i) = atan2(Q_smoothed/Q_amplitude,I_smoothed/I_amplitude);
161
162     clear I_smoothed Q_smoothed
163
164     % DETERMINE THE ORDER OF PHASE SHIFT
165     order = zeros(length(phase(:,i)),1);
166
167     for j = 1:1:length(phase(:,i))-1
168         if phase(j+1,i) - phase(j,i) < -pi
169             order(j+1:length(phase(:,i))) = order(j) + 1;
170         elseif phase(j+1,i) - phase(j,i) > pi
171             order(j+1:length(phase(:,i))) = order(j) - 1;
172         end
173     end
174
175     % ASSUME THE PHASE SHIFT STARTS AS ORDER 0 AND MAKE CONTINUOUS
176     phase(:,i) = phase(:,i) + 2*pi*order;
177
178 %     figure(shot*100+50+chord)
179 %     plot(t,phase(:,i),'c')
180 %     title('Phase Calculation and Spline Subtraction','FontSize',18)
181 %     hold on
182
183     %%%%%%%%% THIS SECTION OF CODE FOR POLYNOMIAL SUBTRACTION %%%%%%%%%
184
185 %     fit_interval = 0.7; % FRACTION OF THE TIME FRAME TO USE FOR FIT
186 %     p_order = 4;        % ORDER OF THE POLYNOMIAL TO FIT BASELINE PHASE
187 %
188 %     % SELECT PORTION OF CALCULATED PHASE SHIFT TO CALCUATE BASELINE
189 %     n_fit_end = floor(n_end + fit_interval*(n_end - n_start));
190 %     t_baseline = time(1:n_fit_end);
191 %     phase_baseline = phase(1:n_fit_end,i);
192 %
193 %     % ISOLATE BASELINE PHASE SHIFT
194 %     t_baseline(n_start:n_end) = [];
195 %     phase_baseline(n_start:n_end) = [];
196 %
197 %     % FIT THE BASELINE PHASE SHIFT TO A POLYNOMIAL
198 %     phase_fit = polyval(polyfit(t_baseline',phase_baseline,p_order), time);
199 %
```

```
%     plot(t, phase_fit,'m')
%     xlim([-25*10^-6 600*10^-6])

    %%%%%%%%% THIS SECTION OF CODE FOR SPLINE SUBTRACTION %%%%%%%%%

    fit_interval = 1.5; % FRACTION OF THE TIME FRAME TO USE FOR FIT
    n_fit_end = floor(n_end + fit_interval*(n_end - n_start));

    % SMOOTH, SUBSAMPLE, AND SPLINE THE BASELINE PHASE SHIFT
    % phase_smooth = smooth(phase(:,i),300,'sgolay');
    phase_smooth = fastsmooth(phase(:,i),100,1,1);

    if shot < 2408
        phase_sub = phase_smooth([n_zero-floor(20/dt):floor(18/dt):n_zero ...
                    n_end:floor(50/dt):n_fit_end]);

        time_sub = time([n_zero-floor(20/dt):floor(18/dt):n_zero ...
                   n_end:floor(50/dt):n_fit_end]);
    else
        phase_sub = phase_smooth([n_start-floor(90/dt):floor(40/dt):n_start ...
                    n_end:floor(50/dt):n_fit_end]);

        time_sub = time([n_start-floor(90/dt):floor(40/dt):n_start ...
                   n_end:floor(50/dt):n_fit_end]);
    end

    phase_spline = interp1(time_sub, phase_sub, time, 'pchip')';

%     plot(t, phase_smooth,'r', time_sub/10^6, phase_sub, 'bo')
%     plot(time/10^6, phase_spline, 'b')
%     xlim([-100/10^6 700/10^6])

%     axis([-100/10^6 300/10^6 1.2 1.7])
%     xlabel('Time (s)','FontSize',16)
%     ylabel('Phase (rad) ','FontSize',16)
%     title('Plasma Phase Shift Isolation','FontSize',18)
%     legend('Raw Phase','Filtered Phase','Fit Points','Background Spline',0)
%     hold on

    clear t

    % SUBTRACT BASELINE

    phase(:,i) = phase(:,i) - phase_spline(:);

    % CALCULATE AND SUBTRACT OUT AVERAGE OFFSET, FROM T=-10 TO 0.

    phase(:,i) = phase(:,i) - ...
                     sum(phase(n_zero-floor(10/dt):n_zero,i))/...
                     (1+floor(10/dt));

    % EXTRACT DATA FROM TIME FRAME OF INTEREST, PAD BY 10 MICROSECONDS
    time_save = time((n_start-10/dt):(n_end+10/dt))';
    phase_save(:,i) = phase((n_start-10/dt):(n_end+10/dt),i);

    clear phase

%     % PLOT PRE-SMOOTHED PHASE TRACE
%     figure(shot*100+70+chord)
%     plot(time_save, phase_save(:,i),'b')
%     hold on

```

```
262     if phase_smoothing == true
263
264         % SMOOTH THE TRACE 10 TIMES WITH WIDTH 10 BOXCAR
265
266         for k = 1:1:10
267             phase_save(:,i) = fastsmooth(phase_save(:,i),10,1,1);
268         end
269     end
270
271 %     plot(time_save, phase_save(:,i),'r')
272 %     axis([-50 200 -0.025 0.1])
273 %     xlabel('Time (\mus)','FontSize',16)
274 %     ylabel('Phase (rad) ','FontSize',16)
275 %     %title('Boxcar Smoothing of Phase Shift','FontSize',18)
276 %     title('Signal-To-Noise Ratio as Little as 6','FontSize',18)
277 %     %legend('Unsmoothed','Smoothed',0)
278 %     hold on
279 %
280 %     shalsm
281
282 end
283
284 % figure(4)
285 % plot(time_save,phase_save)
286
287 disp('Phase is');
288 disp(num2str(phase_save(n_save - n_start + floor(10/dt))))
289 disp('at time');
290 disp(num2str(time_save(n_save - n_start + floor(10/dt))))
291
292 Ce = (lambda0*e^2)/(4*pi*epsilon0*me*c^2)
293
294 C0_aluminum = (2*pi/lambda0)*(0.063163)/(2.503*10^25);  % PROBLEM HERE?
295
296 Ce/C0_aluminum
297
298 ne_lower = (phase_save(n_save - n_start + floor(10/dt))/(Ce*Zeff*dL))/10^4
```

Appendix B

Schlieren periscope mount

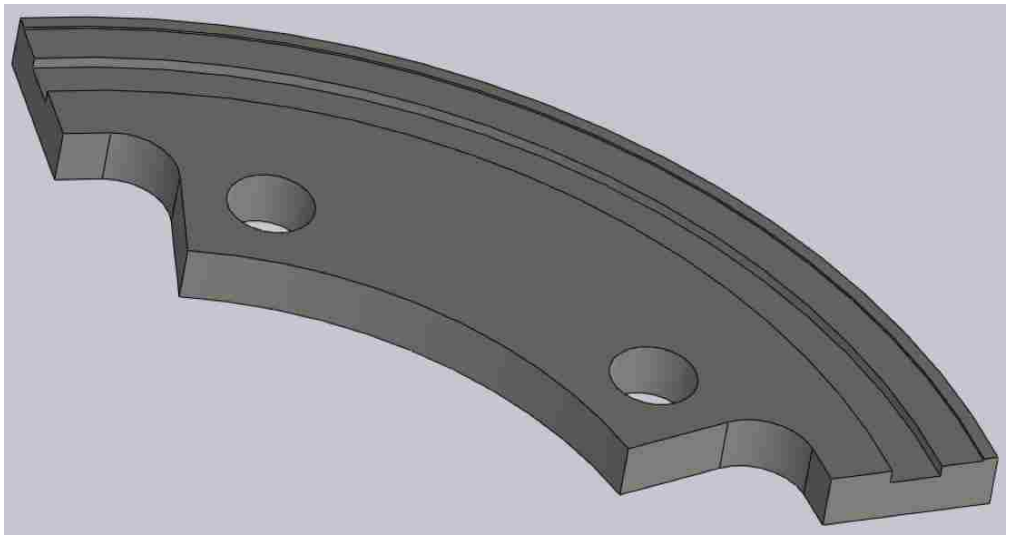

Figure B.1: The base for the 'periscope' mount bolts directly to the 11-in flange and acts as a 'rotor' on which the 'slider' is mounted. This part was silver plated to reduce surface friction.

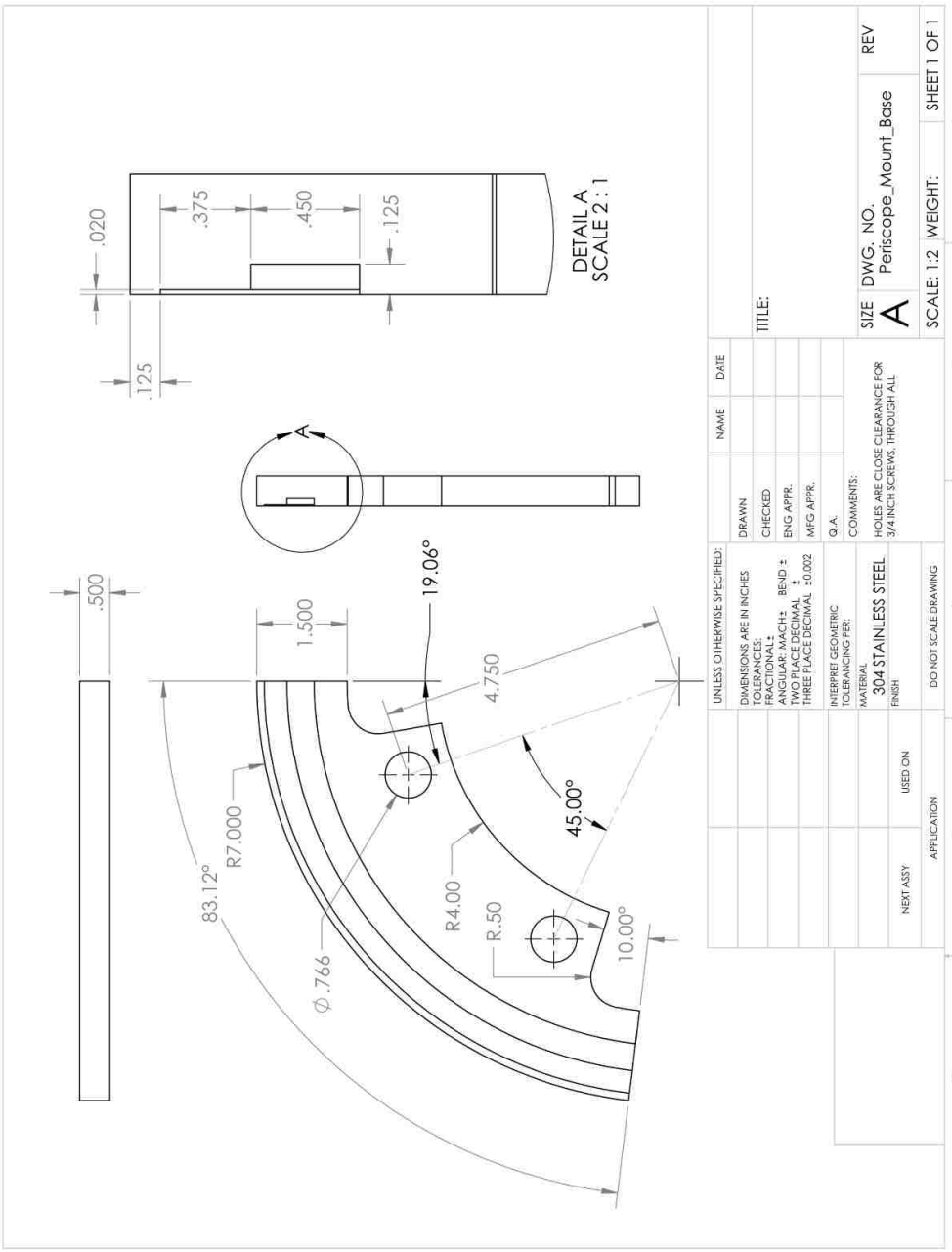

Figure B.2: Drawing of the base for the periscope mount. This part was silver plated to reduce surface friction.

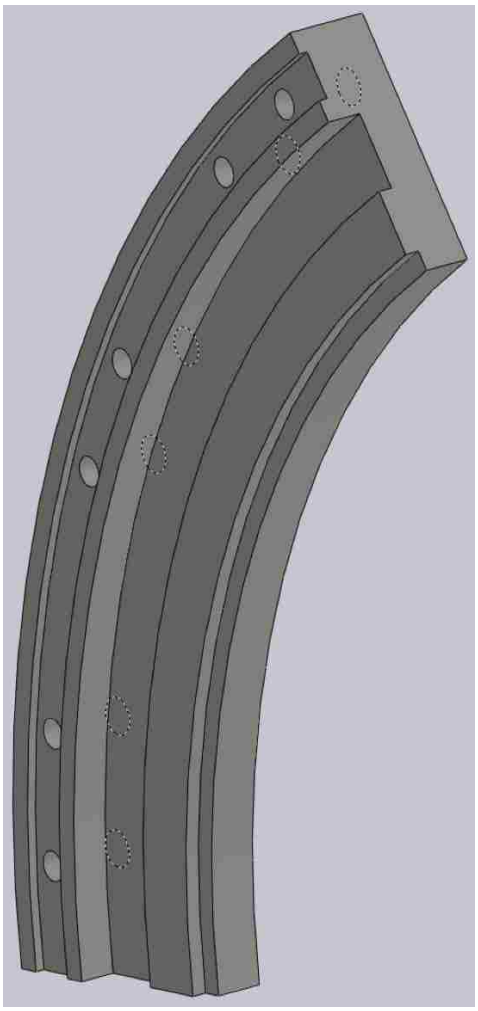

Figure B.3: The lower portion of the slider for the periscope mount. Together with the upper portion, slides in the azimuthal direction around the port. This part was silver plated to reduce surface friction.

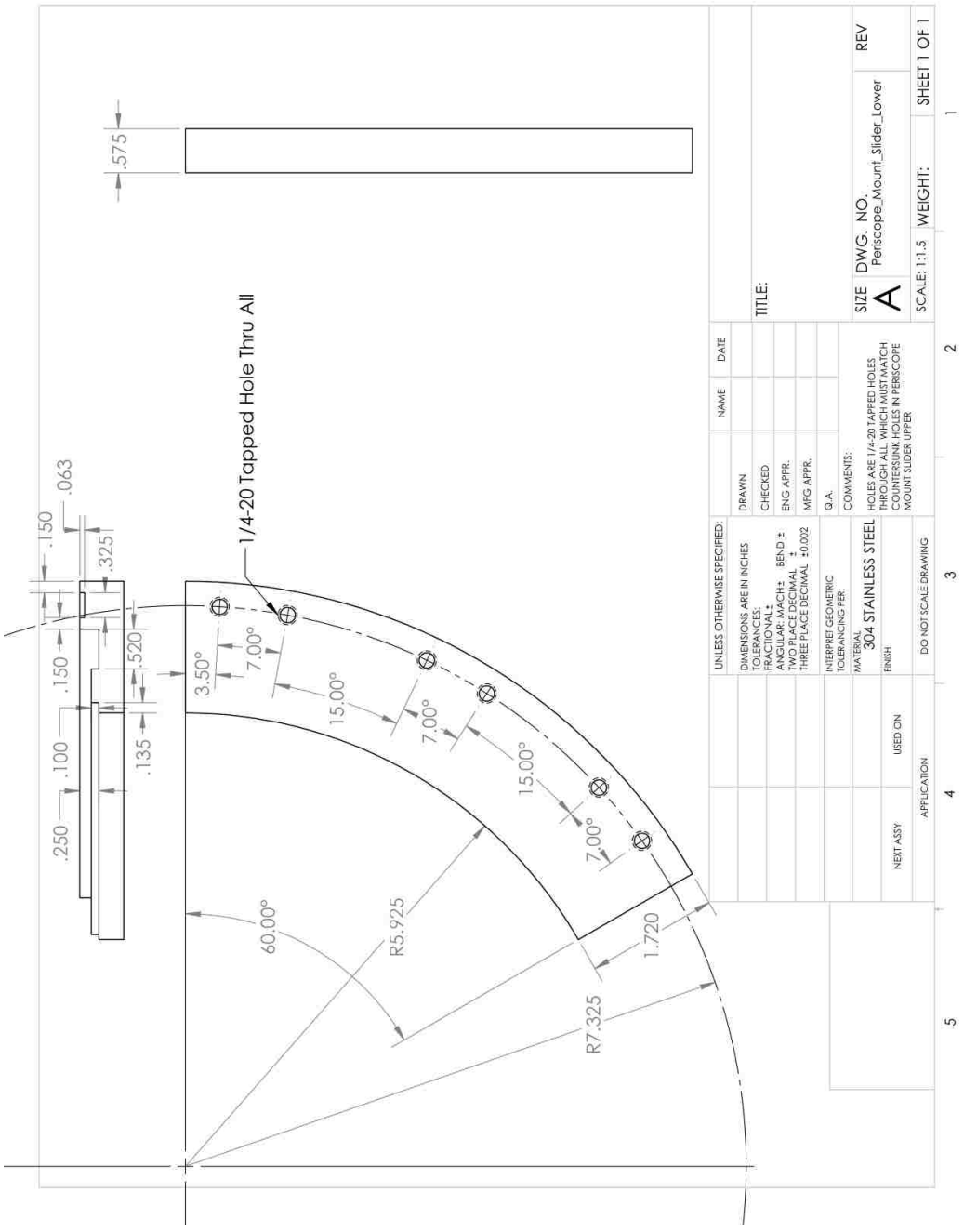

Figure B.4: Drawing of the lower portion of the slider for the periscope mount. This part was silver plated to reduce surface friction.

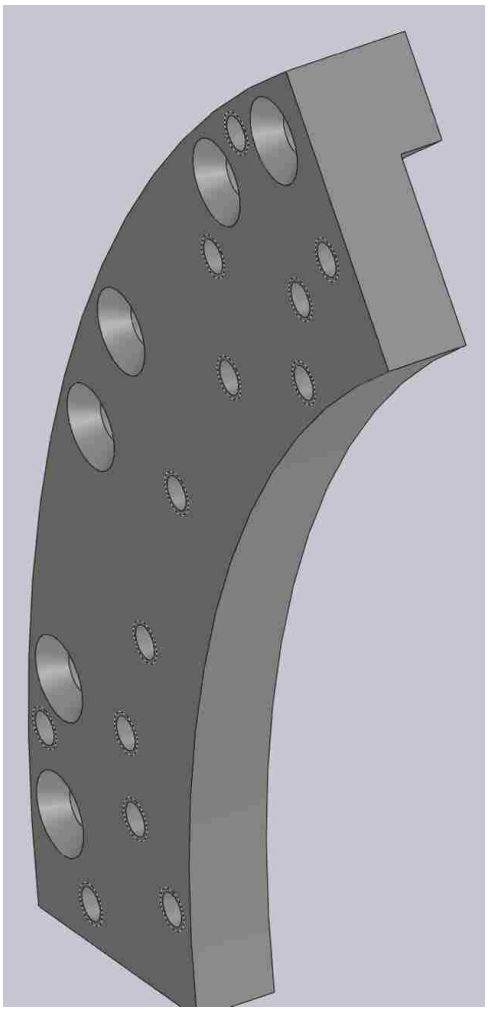

Figure B.5: The upper portion of the slider for the periscope mount. Together with the lower portion, slides in the azimuthal direction around the port. This part was silver plated to reduce surface friction. Conformable soft-tip (silver-tip) set screws were used in the azimuthal array of tapped holes to securely clamp the slider to the base without damaging the surface of the base.

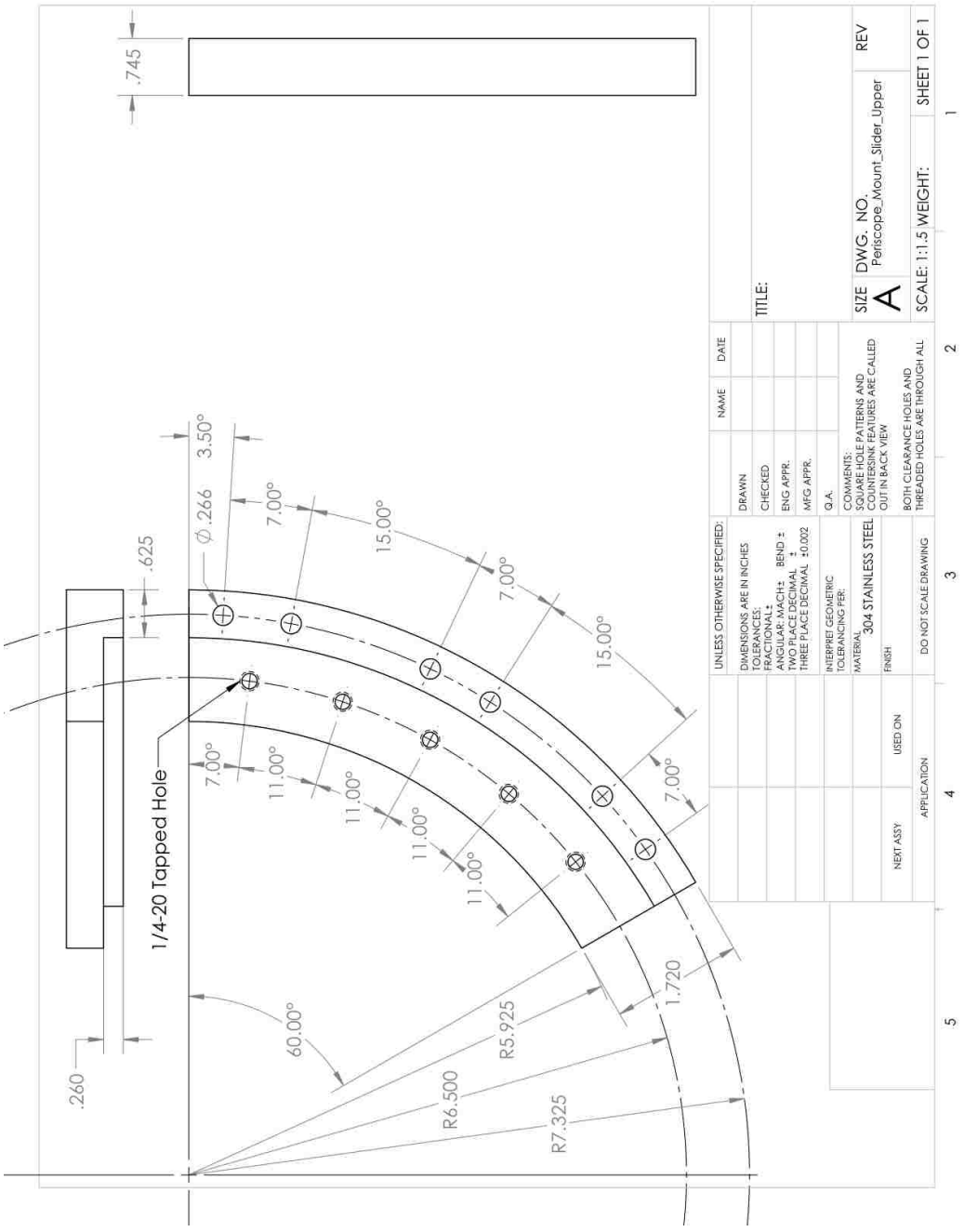

Figure B.6: Drawing of the upper portion of the slider for the periscope mount. This part was silver plated to reduce surface friction. Conformable soft-tip (silver-tip) set screws were used in the azimuthal array of tapped holes to securely clamp the slider to the base without damaging the surface of the base.

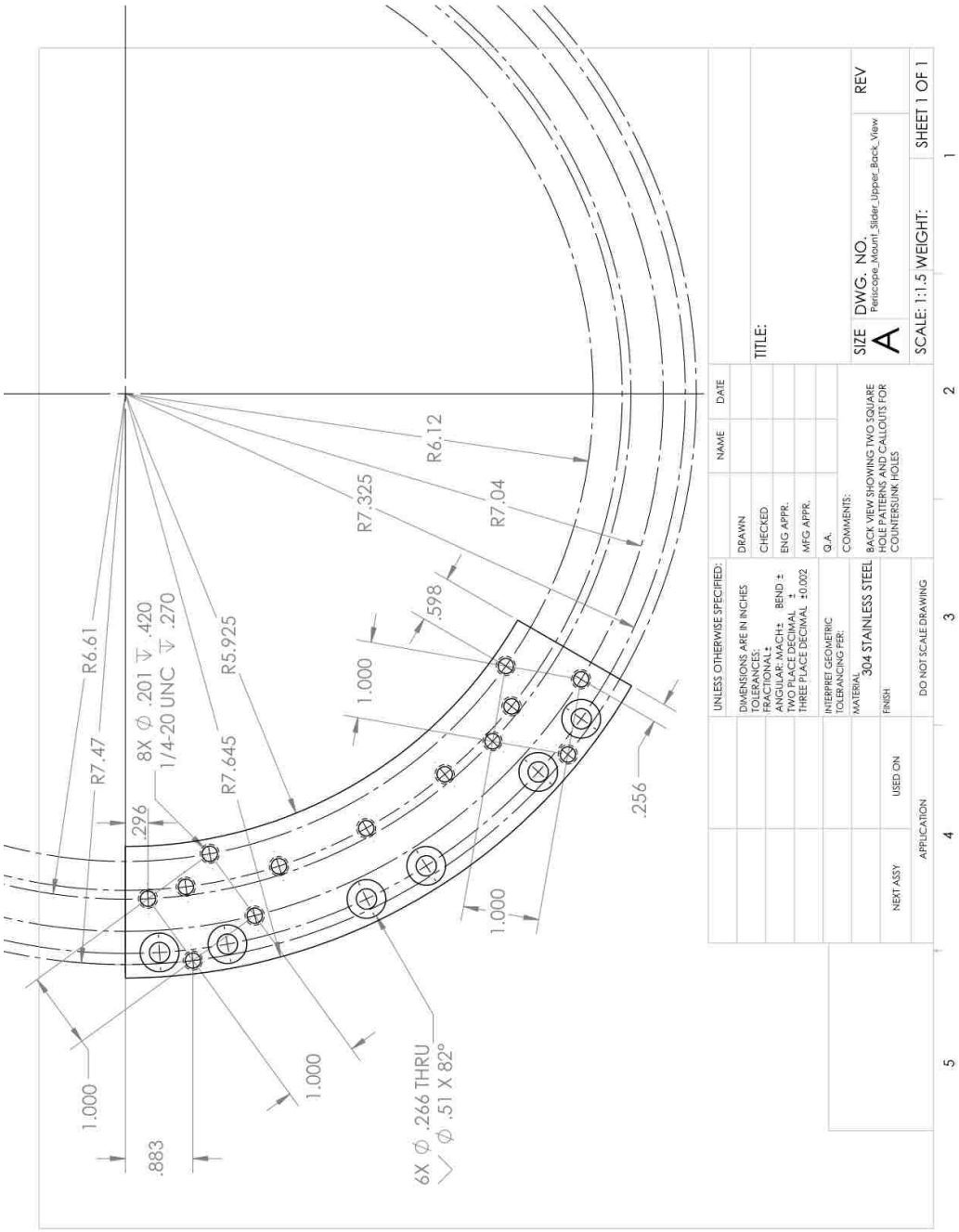

Figure B.7: Drawing of the back of the upper portion of the slider for the periscope mount. This part was silver plated to reduce surface friction. Conformable soft-tip (silver-tip) set screws were used in the azimuthal array of tapped holes to securely clamp the slider to the base without damaging the surface of the base.

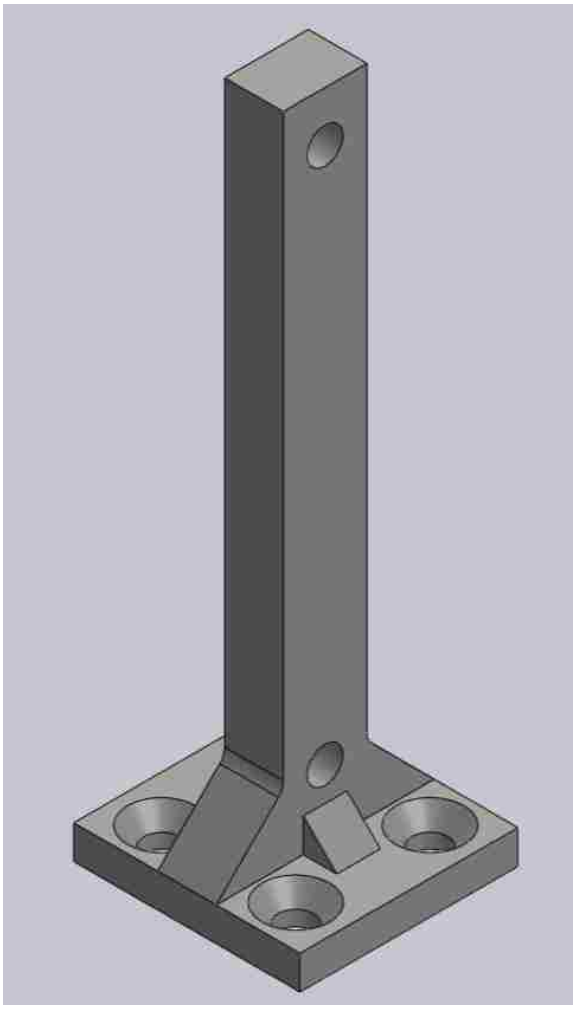

Figure B.8: The rotary mount of the periscope mount. This is a bracket to which a rotation stage is mounted.

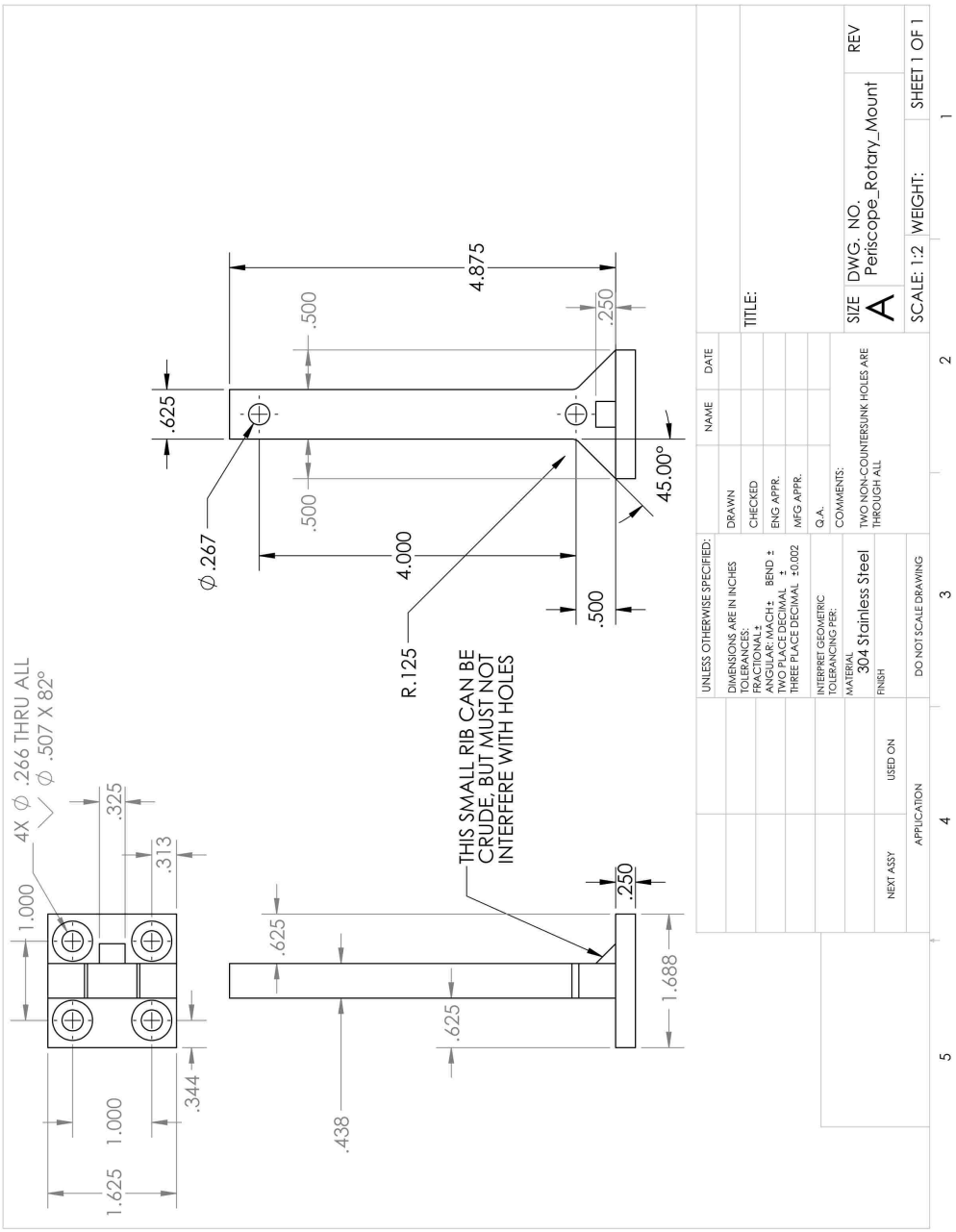

Figure B.9: Drawing of the rotary mount of the periscope mount.

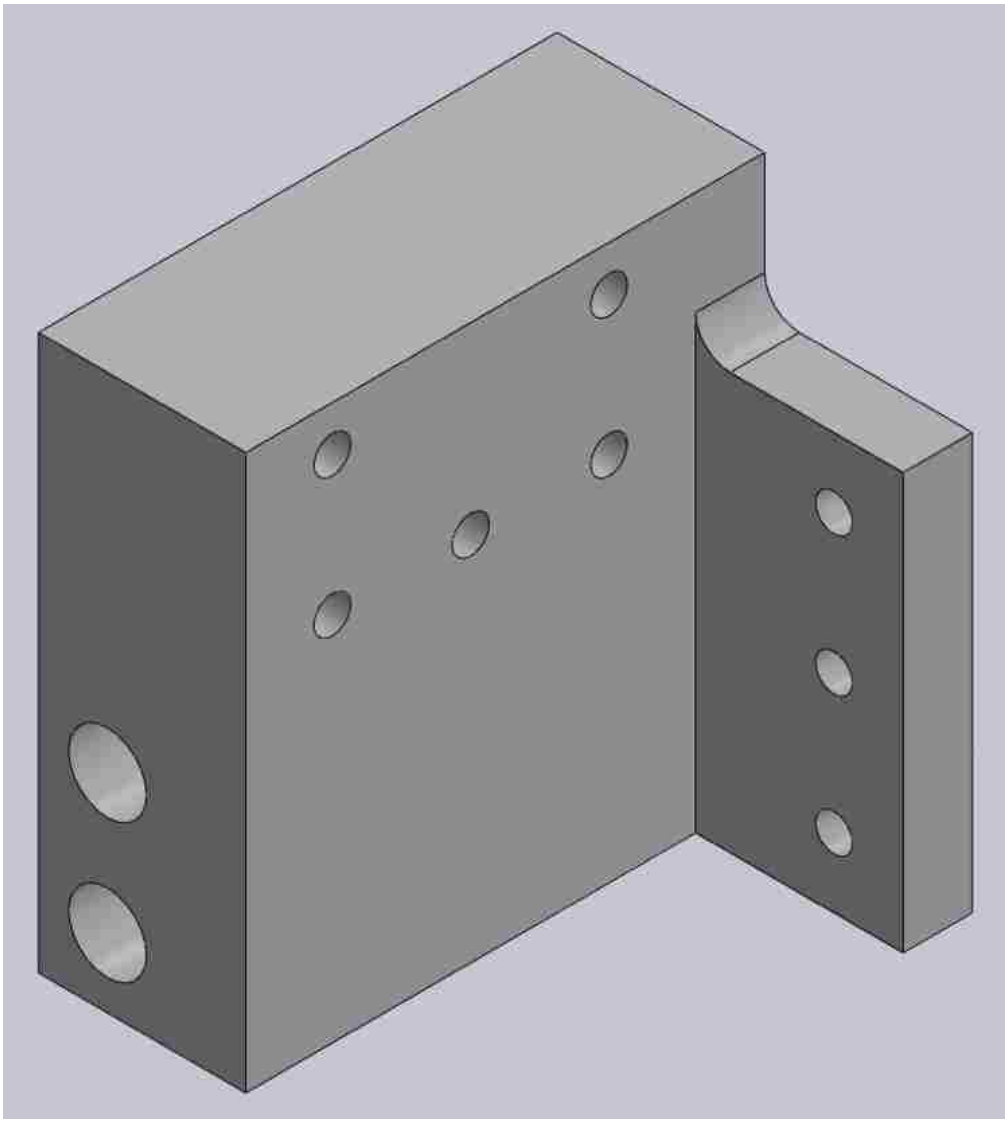

Figure B.10: The mirror adapter for the periscope mount bolts to the rotation stage and provides a mounting point for the lightweight rectangular mirror mount.

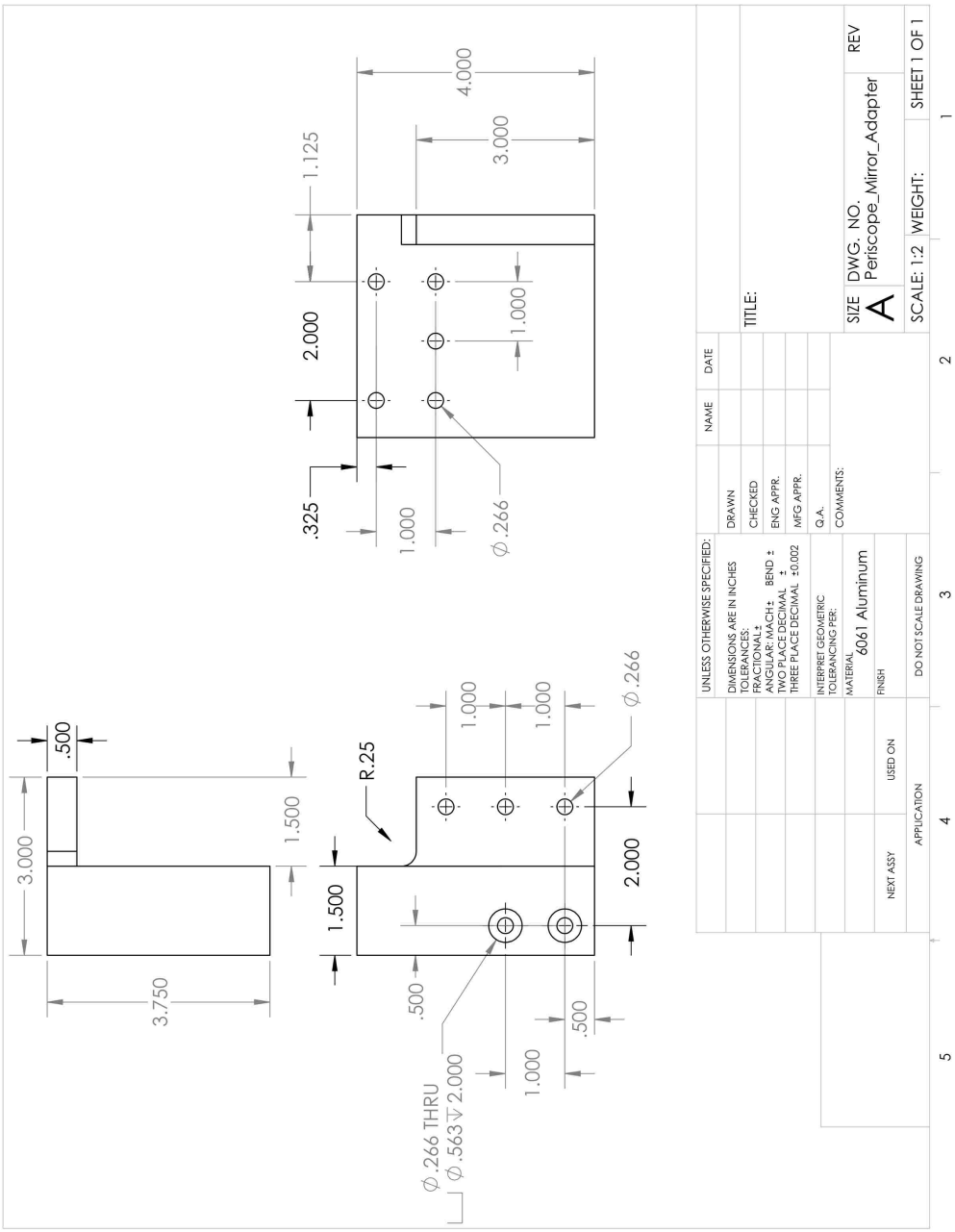

Figure B.11: Drawing of the mirror adapter for the periscope mount.

Appendix C

Schlieren lightweight mount

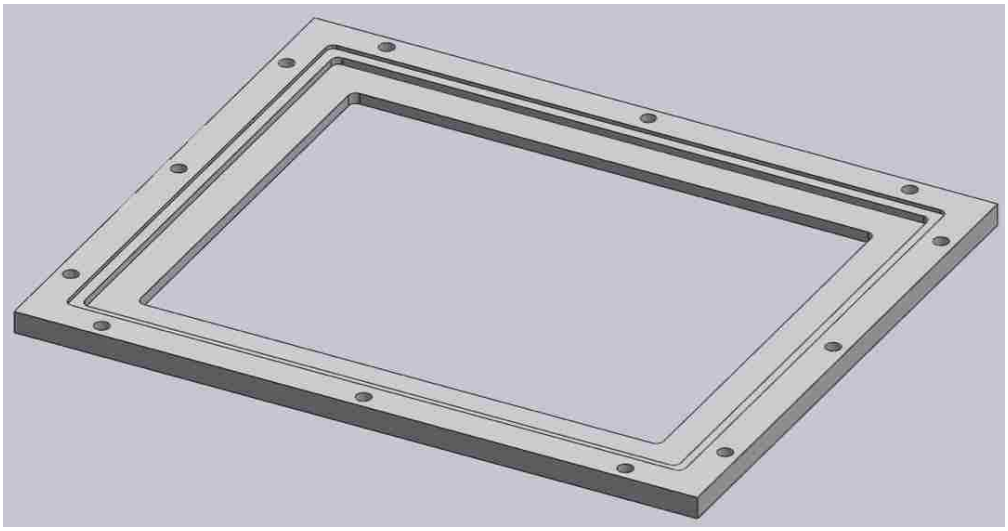

Figure C.1: The front of the lightweight mount. This bolts to the back of the lightweight mount to hold mirror in place.

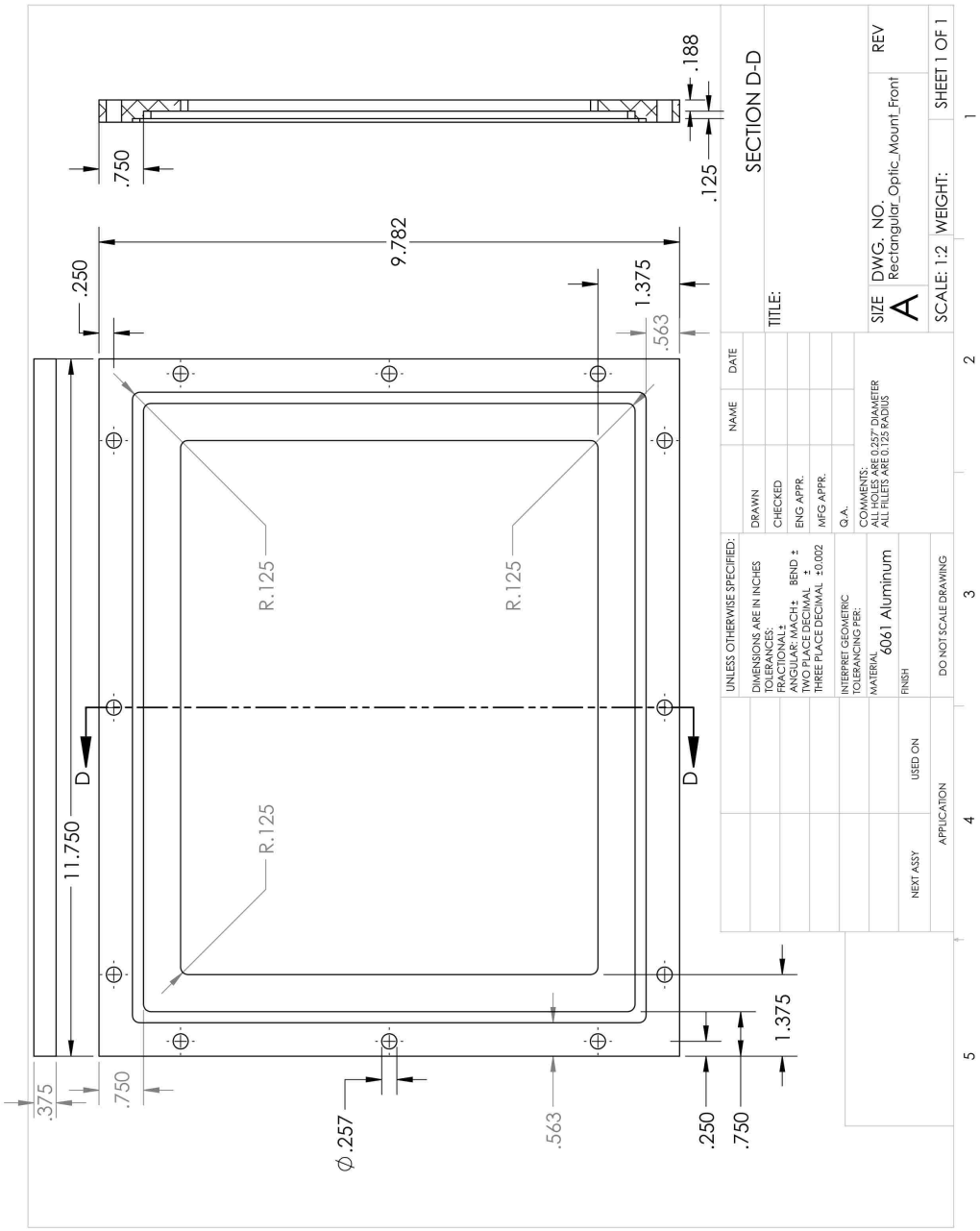

Figure C.2: Drawing of the front of the lightweight mount.

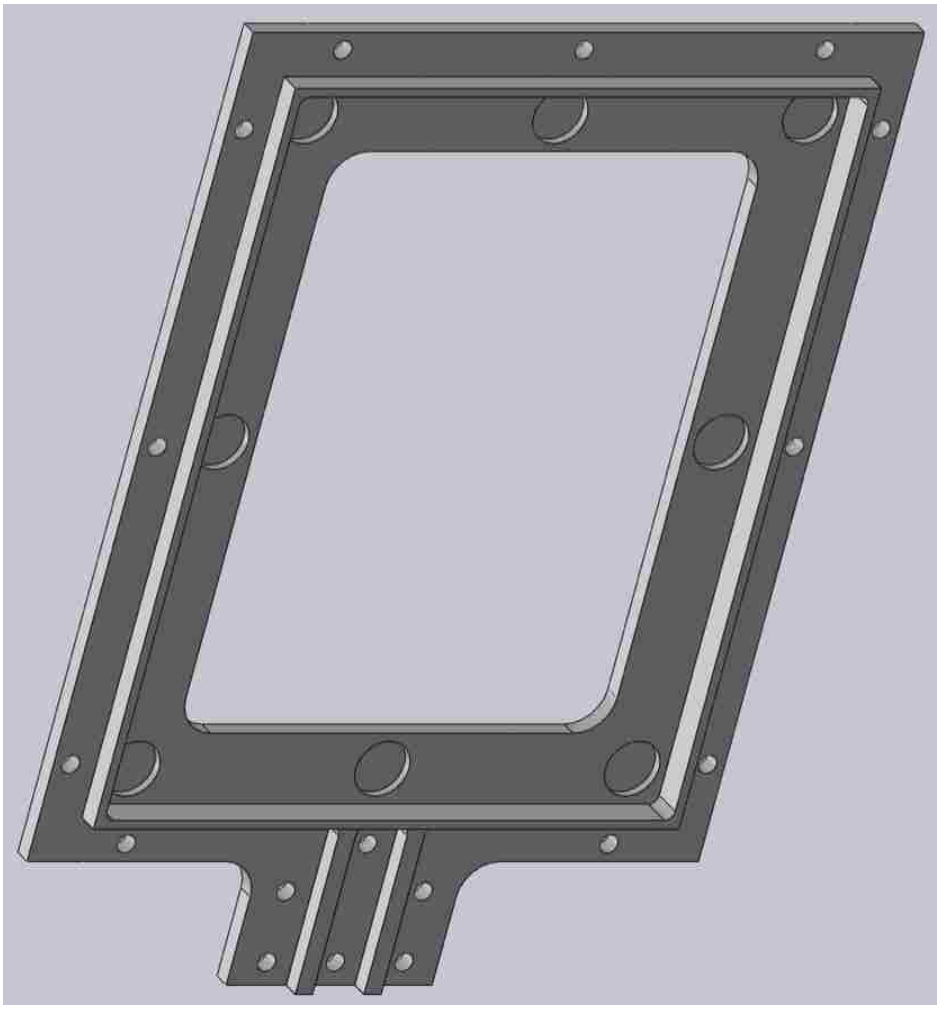

Figure C.3: The back of the lightweight mount. This bolts to the front of the lightweight mount to hold mirror in place.

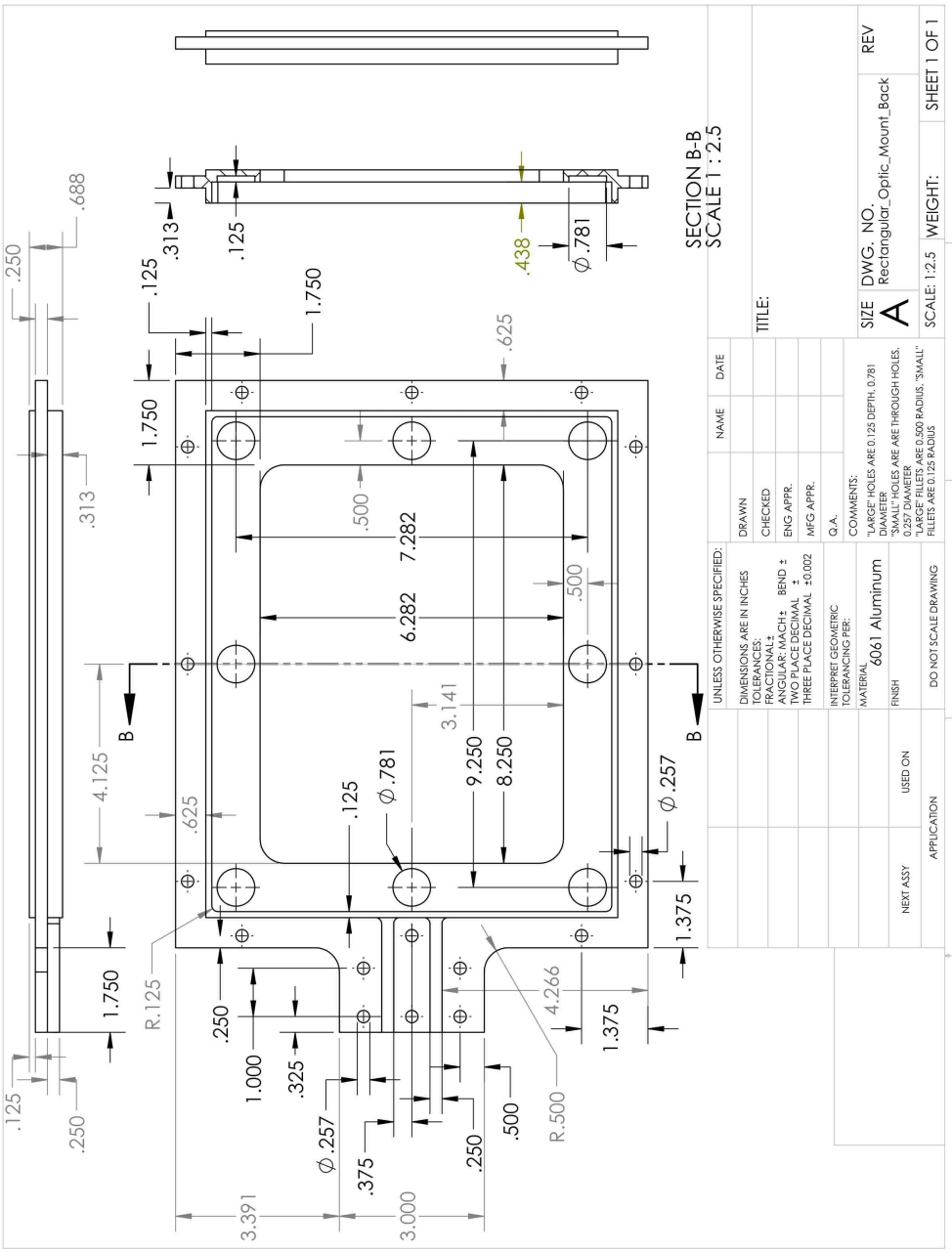

Figure C.4: Drawing of the back of the lightweight mount.

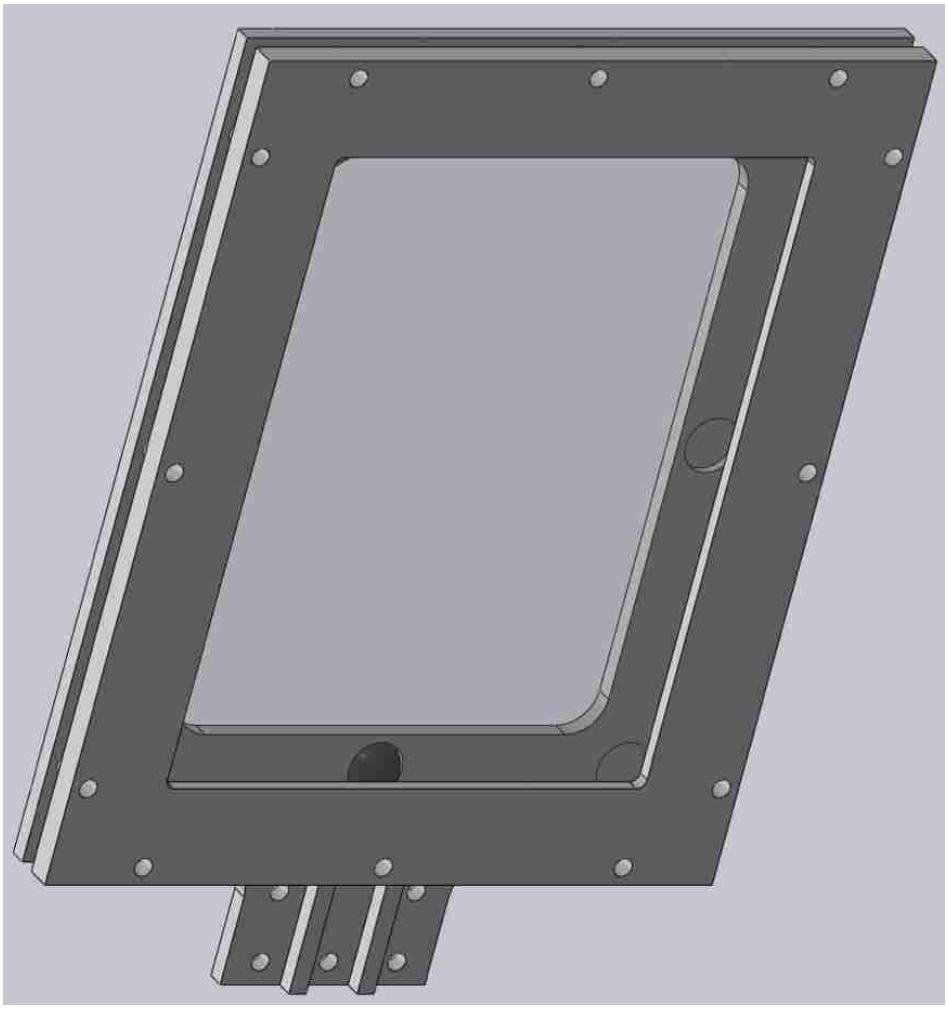

Figure C.5: The assembled lightweight rectangular mount. Note the recommended use of hemispherical soft rubber bumpers to cushion mirror (in circular depressions).

References

[1] Lord Rayleigh. Investigation of the character of the equilibrium of an incompressible heavy fluid of variable density. *Proc. London Math Soc.*, XIV(1):170, 1883.

[2] G. Taylor. The instability of liquid surfaces when accelerated in a direction perpendicular to their planes. I. *Proc. R. Soc. London, Ser. A*, 201(1065):192, 1950.

[3] S. Chandrasekhar. *Hydrodynamic and Hydromagnetic Stability.* Oxford University Press, Oxford, 1961.

[4] J. D. Huba, J. G. Lyon, and A. B. Hassam. Theory and simulation of the Rayleigh-Taylor instability in the limit of large Larmor radius. *Physical Review Letters*, 59(26):2971–2974, 1987.

[5] J. Hester, A. Loll, W. Blair, R. Sankrit, P.Scowen, and D. de Martin. A giant Hubble mosaic of the Crab nebula. News Release Number: STScI-2005-37, 1 Dec 2005.

[6] O. Porth, S. S. Komissarov, and R. Keppens. Rayleigh–Taylor instability in magnetohydrodynamic simulations of the Crab nebula. *Monthly Notices of the Royal Astronomical Society*, 443(1):547–558, 2014.

[7] J. Hester and P. Scowen. Embryonic stars emerge from interstellar"eggs". News Release Number: STScI-1995-44, 2 Nov 1995.

[8] J. O. Kane, D. D. Ryutov, B. A. Remington, S. G. Glendinning, Marc Pound, and David Arnett. Hydrodynamics of the Eagle nebula: the Pillars of Creation revisited. *Bull. Amer. Astron. Soc.*, 33:883, 2001.

[9] S. Atzeni and J. Meyer-Ter-Vehn. *The Physics of Inertial Fusion.* Oxford University Press, Oxford, 2004.

[10] R. C. Kirkpatrick, I. R. Lindemuth, and M. S. Ward. Magnetized target fusion: An overview. *Fus. Tech.*, 27:201, 1995.

[11] H. F. Robey. Effects of viscosity and mass diffusion in hydrodynamically unstable plasma flows. *Physics of Plasmas*, 11:4123, 2004.

[12] B. M. Haines, E. L. Vold, K. Molvig, C. Aldrich, and R. Rauenzahn. The effects of plasma diffusion and viscosity on turbulent instability growth. *Physics of Plasmas*, 21(9):092306, 2014.

[13] D. B. Sinars, S. A. Slutz, M. C. Herrmann, R. D. McBride, M. E. Cuneo, K. J. Peterson, R. A. Vesey, C. Nakhleh, B. E. Blue, K. Killebrew, D. Schroen, K. Tomlinson, A. D. Edens, M. R. Lopez, I. C. Smith, J. Shores, V. Bigman, G. R. Bennett, B. W. Atherton, M. Savage, W. A. Stygar, G. T. Leifeste, and J. L. Porter. Measurements of magneto-rayleigh-taylor instability growth during the implosion of initially solid al tubes driven by the 20-ma, 100-ns z facility. *Phys. Rev. Lett.*, 105:185001, Oct 2010.

[14] D. B. Sinars, S. A. Slutz, M. C. Herrmann, R. D. McBride, M. E. Cuneo, C. A. Jennings, J. P. Chittenden, A. L. Velikovich, K. J. Peterson, R. A. Vesey, C. Nakhleh, E. M. Waisman, B. E. Blue, K. Killebrew, D. Schroen, K. Tomlinson, A. D. Edens, M. R. Lopez, I. C. Smith, J. Shores, V. Bigman, G. R. Bennett, B. W. Atherton, M. Savage, W. A. Stygar, G. T. Leifeste, and J. L. Porter. Measurements of magneto-rayleigh–taylor instability growth during the implosion of initially solid metal liners. *Physics of Plasmas*, 18(5):056301, 2011.

[15] T. J. Awe, C. A. Jennings, R. D. McBride, M. E. Cuneo, D. C. Lamppa, M. R. Martin, D. C. Rovang, D. B. Sinars, S. A. Slutz, A. C. Owen, K. Tomlinson, M. R. Gomez, S. B. Hansen, M. C. Herrmann, M. C. Jones, J. L. McKenney, G. K. Robertson, G. A. Rochau, M. E. Savage, D. G. Schroen, and W. A. Stygar. Modified helix-like instability structure on imploding z-pinch liners that are preimposed with a uniform axial magnetic field. *Physics of Plasmas*, 21(5):056303, 2014.

[16] M. R. Weis, P. Zhang, Y. Y. Lau, I. M. Rittersdorf, J. C. Zier, R. M. Gilgenbach, M. H. Hess, and K. J. Peterson. Temporal evolution of surface ripples on a finite plasma slab subect ot the magneto-Rayleigh-Taylor instability. *Physics of Plasmas*, 21:122708, 2014.

[17] M. J.-E. Manuel, C. K. Li, F. H. Séguin, J. Frenje, D. T. Casey, R. D. Petrasso, S. X. Hu, R. Betti, J. D. Hager, D. D. Meyerhofer, and V. A. Smalyuk. First measurements of rayleigh-taylor-induced magnetic fields in laser-produced plasmas. *Phys. Rev. Lett.*, 108:255006, Jun 2012.

[18] B. Srinivasan, G. Dimonte, and X.-Z. Tang. Magnetic field generation in rayleigh-taylor unstable inertial confinement fusion plasmas. *Phys. Rev. Lett.*, 108:165002, Apr 2012.

[19] B.I. Jun, M.L. Norman, and J.M. Stone. A numerical study of Rayleigh-Taylor instability in magnetic fluids. *The Astrophysical Journal*, 453:332, 1995.

[20] J. M. Stone and T. Gardiner. Nonlinear evolution of the magnetohydrodynamic Rayleigh-Taylor instability. *Physics of Fluids*, 19:094104, 2007.

[21] J. M. Stone and T. Gardiner. The magnetic Rayleigh-Taylor instability in three dimensions. *The Astrophysical Journal*, 671:1726–1735, 2007.

[22] B. Srinivasan and X.-Z. Tang. The mitigating effect of magnetic fields on Rayleigh-Taylor unstable inertial confinement fusion plasmas. *Physics of Plasmas*, 20(056307):056307, 2013.

[23] P. Y. Chang, G. Fiksel, M. Hohenberger, J. P. Knauer, R. Betti, F. J. Marshall, D. D. Meyerhofer, F. H. Seguin, and R. D. Petrasso. Fusion Yield Enhancement in Magnetized Laser-Driven Implosions. *Physical Review Letters*, 107(3):035006, 2011.

[24] M. Hohenberger, P-Y Chang, G. Fiksel, J. P. Knauer, R. Betti, F. J. Marshall, D. D. Meyerhofer, F. H. Seguin, and R. D. Petrasso. Inertial confinement fusion implosions with imposed magnetic field compression using the OMEGA Laser. *Physics of Plasmas*, 19(5), 2012.

[25] S. C. Hsu, A. L. Moser, E. C. Merritt, C. S. Adams, J. P. Dunn, S. Brockington, A. Case, M. Gilmore, A. G. Lynn, S. J. Messer, and F. D. Witherspoon. Laboratory plasma physics experiments using merging supersonic plasma jets. *Journal of Plasma Physics*, FirstView:1–12, 12 2014.

[26] C. Thoma, D. R. Welch, and S. C. Hsu. Particle-in-cell simulations of collisionless shock formation via head-on merging of two laboratory supersonic plasma jets. *Physics of Plasmas*, 20(8):082128, 2013.

[27] D. A. Baker and J. E. Hammel. Experimental studies of the penetration of a plasma stream into a transverse magnetic field. *Physics of Fluids (1958-1988)*, 8(4):713–722, April 1965.

[28] D. A. Baker and J. E. Hammel. Experimental studies of a crossed-field plasma accelerator. Los Alamos Scientific Laboratory Report LA-3078, Los Alamos Scientific Laboratory, P.O. Box 1663, Los Alamos, NM., 87545, April 1965.

[29] E. H. Beckner. Flow of a hydrogen plasma through a transverse magnetic field. *Physics of Fluids (1958-1988)*, 7(4):586–595, 1964.

[30] P. D. Marković and F. R. Scott. Interaction of a helium plasma with an inhomogeneous transverse magnetic field. *Physics of Fluids (1958-1988)*, 14(8):1742–1747, 1971.

[31] G. Jellison and C. R. Parsons. Resonant shadowgraph and schlieren studies of magnetized laser-produced plasmas. *Physics of Fluids (1958-1988)*, 24(10):1787–1790, 1981.

[32] G. Jellison and C. R. Parsons. Observations of magnetized plasma flow through stationary background plasma. *Physics of Fluids (1958-1988)*, 26(5):1171–1172, 1983.

[33] E. S. Weibel. Spontaneously growing transverse waves in a plasma due to an anisotropic velocity distribution. *Phys. Rev. Lett.*, 2:83–84, Feb 1959.

[34] W. Fox, G. Fiksel, A. Bhattacharjee, P.-Y. Chang, K. Germaschewski, S. X. Hu, and P. M. Nilson. Filamentation instability of counterstreaming laser-driven plasmas. *Phys. Rev. Lett.*, 111:225002, Nov 2013.

[35] E. C. Merritt, A. L. Moser, S. C. Hsu, C. S. Adams, J. P. Dunn, M. A. Holgado, and M. A. Gilmore. Experimental evidence for collisional shock formation via two obliquely merging supersonic plasma jets. *Physics of Plasmas*, 21(5):055703, 2014.

[36] A. L. Moser and S. C. Hsu, "Observation of ionization-mediated transition from collisionless interpenetration to collisional stagnation between two merging supersonic plasmas," submitted (2014); http://arxiv.org/abs/1405.2286.

[37] A. L. Moser and S. C. Hsu, "Experimental characterization of a transition from collisionless to collisional interaction between head-on-merging supersonic plasma jets," submitted (2014); http://arxiv.org/abs/1412.1382.

[38] G. F. Swadling, S. V. Lebedev, G. N. Hall, F. Suzuki-Vidal, G. Burdiak, A. J. Harvey-Thompson, S. N. Bland, P. De Grouchy, E. Khoory, L. Pickworth, J. Skidmore, and L. Suttle. Shock-less interactions of ablation streams in tungsten wire array z-pinches. *Physics of Plasmas*, 20(6):2706, 2013.

[39] R. P. Drake. The design of laboratory experiments to produce collisionless shocks of cosmic relevance. *Physics of Plasmas*, 7(11):4690, 2000.

[40] A. Spitkovsky. Particle acceleration in relativistic collisionless shocks: Fermi process at last? *The Astrophysical Journal Letters*, 682(1):L5–L8, 2008.

[41] E. Waxman. Gamma-ray bursts and collisionless shocks. *Plasma Physics and Controlled Fusion*, 48(12B):B137, 2006.

[42] C. Courtois, R. A. D. Grundy, A. D. Ash, D. M. Chambers, and N. C. Woolsey. Experiment on collisionless plasma interaction with applications to supernova remnant physics. *Physics of Plasmas*, 11(7):3386, 2004.

[43] S. C. Hsu, E. C. Merritt, A. L. Moser, T. J. Awe, S. J. E. Brockington, J. S. Davis, C. S. Adams, A. Case, J. T. Cassibry, J. P. Dunn, M. A. Gilmore, A. G. Lynn, S. J. Messer, and F. D. Witherspoon. Experimental characterization of railgun-driven supersonic plasma jets motivated by high energy density physics applications. *Physics of Plasmas*, 19:123514, 2012.

[44] A. L. Moser. Observation of ionization-mediated transition from collisionless interpenetration to collisional stagnation during merging of two supersonic plasmas. In *Proceedings of the 56th Annual Meeting of the APS Division of Plasma Physics*, volume 59, New Orleans, LA, USA, Oct. 27–31 2014. American Physical Society.

[45] E. C. Merritt, A. G. Lynn, M. A. Gilmore, and S. C. Hsu. Multi-chord fiber-coupled interferometer with a long coherence length laser. *Review of Scientific Instruments*, 83:033506, 2012.

[46] E. C. Merritt, A. G. Lynn, M. A. Gilmore, C. Thoma, J. Loverich, and S. C. Hsu. *Review of Scientific Instruments*, 83:10D523, 2012.

[47] Prism Computational Sciences: www.prism-cs.com.

[48] E. C. Merritt. *Measurements of railgun generated supersonic plasma jet propagation and two jet oblique merging.* Doctoral dissertation, The University of New Mexico, Albuquerque, NM, USA, June 2013.

[49] S.C. Hsu, T.J. Awe, S. Brockington, A. Case, J.T. Cassibry, G. Kagan, S.J. Messer, M. Stanic, X. Tang, D.R. Welch, and F.D. Witherspoon. Spherically imploding plasma liners as a standoff driver for magnetoinertial fusion. *Plasma Science, IEEE Transactions on*, 40(5):1287–1298, May 2012.

[50] G. S. Settles. *Schlieren and Shadowgraph Techniques.* Springer-Verlag, Berlin Heidelberg, 2001.

[51] P. Rysselberghe. Remarks concerning the clausius-mossotti law. *The Journal of Physical Chemistry*, 36(4):1152–1155, 1931.

[52] R. A. Alpher and D. R. White. Optical refractivity of high-temperature gases. i. effects resulting from dissociation of diatomic gases. *Physics of Fluids (1958-1988)*, 2(2):153–161, 1959.

[53] J. D. Huba. *NRL Plasma Formulary*. Naval Research Laboratory, Washington, DC, 2011.

[54] S. I. Braginskii. Transport processes in a plasma. *Reviews of Plasma Physics*, 1:205, 1965.

[55] B. Srinivasan, A. Hakim, and U. Shumlak. Numerical methods for two-fluid dispersive fast mhd phenomena. *Commun. Comput. Phys.*, 10:183–215, 2011.

[56] U. Shumlak, R. Lilly, N. Reddell, E. Sousa, and B. Srinivasan. Advanced physics calculations using a multi-fluid plasma model. *Comput. Phys. Commun.*, 182(9):1767–1770, 2011.

[57] B. Srinivasan and X.-Z. Tang. Mitigating hydrodynamic mix at the gas-ice interface with a combination of magnetic, ablative, and viscous stabilization. *Eur. Phys. Lett.*, 107(6):65001, 2014.

[58] J. P. Freidberg. *Ideal magnetohydrodynamics*. Cambridge University Press, Cambridge, UK, 1987.